X-ray Diffraction Studies on the Structural Changes during Bacteriorhodopsin Photocycle.

Doctor of Science

March 2000

Graduate School of Science
Osaka University

Toshihiko OKA

CONTENTS

Abbreviations.

BR	bacteriorhodopsin.
FTIR	Fourier transform infrared.
SVD	singular value decomposition.
PCMB	p-chloromercuribenzoic acid.
PM	purple membrane.
D85	85th aspartic acid in the amino acid residues of BR.
D96N	mutant BR whose 96th aspartic acid was replaced to aspargine.

Section 1.
Bacteriorhodopsin.

A living organism retains its life by various chemical reactions inside its body. Proteins, which are copolymers comprised of 20 kinds of amino acids, play central roles in these chemical reactions. Depending on the differences in amino acid sequences, proteins have marvelous kinds of functions. The elucidation of the principle of protein functions is one of the essential objects to understand the molecular basis of life. Each living organism produces at least 1000 different species of proteins. Each protein possesses its unique tertiary structure and its unique function. Some proteins assemble to form a complex structure and, thus, perform complicated reactions. Therefore, understanding the principle of protein function is not a straightforward task. However, the constituent amino acids are only 20 kinds. It is reasonable to consider that there should be a common principle to express protein functions. In order to study the generality of protein function, the utilization of a protein with a simple and well-defined structure and a simple function would be an effective way. Such a protein has also an advantage in research that sample purification is rather easy. From these points of view, the author investigates bacteriorhodopsin. Bacteriorhodopsin can convert light energy into chemical energy as a single molecule.

Function and photo-reaction of bacteriorhodopsin.

Halobacterium salinarium grows in salt lakes which contain about 30 % NaCl like Dead Sea. Bacteriorhodopsin (BR) is a sole protein in a purple membrane, which is a patch of the cell membrane of *H. salinarium*. A purple membrane is a two dimensional crystal of BR. This crystal has p3 space group, and its unit is a trimer of BR. A purple membrane contains 75 % of BR and 25 % of lipids. A BR molecule consists of 248 amino acids and forms 7 trans-membrane α-helices (Fig.1.1). BR has a retinal linked to K216 at helix G via a protonated Schiff base. BR transports proton (hydrogen ion) from the cytoplasmic side to the extracellular side using the absorbed photon energy. Gradient of proton concentration is generated by the proton transport, and this gradient is used to make ATP, which is common energy currency in a living organism. BR is the smallest and the simplest photo-energy conversion system in all of living organisms. The elucidation of the molecular mechanism of the light-driven proton pump of BR is expected to help me elucidate the energy conversion mechanism in life.

Since BR absorbs photons of visible light its photocycle has been studied in detail by spectroscopic techniques such as flash photolysis and cryo-spectroscopy. The

photocycle is characterized with the distinct absorption spectral changes in the visible light region of the metastable intermediates J, K, L, M, N, and O. FTIR measurements of BR mutants have revealed the states of amino acid residues and some waters in the proton conducting channel. According to these results, charged residues inside BR before photoreaction are R82(+), D85(-), D212(-) and K216(+), which linked to the retinal. It was revealed that K216 and D85 take part in the proton translocation directly. D96 also takes part in the translocation but D96 is uncharged (protonated) before the photoreaction. The photoreaction of BR is as follows (Fig. 1.2). The retinal located inside BR absorbs a photon, whose wavelength is around 570 nm. The retinal is excited to Frank-Condon state. Then all-trans retinal isomerizes into 13-cis producing K intermediate (a few psec after the photon absorption). The retinal twists and keeps a part of photon energy (Smith et al. 1985). Then absorbance spectrum in visible light region shifts towards short wavelength (blue-shift) and L intermediate is formed (a few μsec after the photon absorption). After this, the proton bound to the retinal Schiff base is transferred to D85 within a few tens of μsec to a msec after photon absorption (Braiman et al., 1988). This deprotonaton of the Schiff base causes further blue-shift in BR spectrum and then M intermediate is formed. At almost the same time, a proton is released to the extracellular side from an unknown part X. Then the Schiff base is reprotonated from D96 locating the cytoplasmic side (Butt et al., 1989) and N intermediate is formed. Then the retinal re-isomerizes to all-trans in O intermediate (Smith et al., 1983). D85 transfers its proton to the unknown part X and BR recovers to the original state. The pK's of side chains in residues, which participate in the proton translocation, are as follows; D96 is 11.4 (Saraz et al, 1994), K216 (Schiff base) is >13 (Druckman et al., 1982), and D85 is 2.2 (Richter et al, 1996). Since the pK of a side chain of aspartic acid (D) in solution is about 4.5, the protein environments of these aspartic acids causes the unusual high pK of D96. It is also true in the photoreaction of BR that the protein regulates the pK of a side chains, and it controls the proton transfer between these residues.

Many mutant BRs have been made to study each residue's role in proton pumping. But single amino acid replaced mutants can always keep the function of proton transfer. Only when D85 and D212 are replaced to neutral residues, these mutants lose their function. Considering with these facts, It is probable that there are a few essential components for the function of proton transport in BR. Inferences of the essential ones have been discussed (Kataoka et al. 1994, Lanyi 1995, Haupts et al., 1997). BR structural change(s) during photoreaction have been considered as essential in proton transfer (Kataoka et al. 1994; Lanyi, 1995). A simple idea explaining for the

ion pumping mechanism is that the ion binding state of ion pump links with protein conformations and switches the ion transport pathway from one membrane surface to the other surface (Jardetzky, 1969). The structure of M intermediate was investigated by low resolution diffraction methods under stabilized condition (Dencher et al., 1989; Koch et al., 1991; Nakasako et al., 1991; Subramaniam et al., 1993). These data show a large structural change occurs in this state. Subramaniam et al. (1993) revealed that the cytoplasmic side of BR changes its structure in the photocycle. The proton transfer from the Schiff base to D85 occurs in L to M transition. It was shown that this structural change is closely related to the deprotonation of the Schiff base; in the original structure (conformation E) the proton channel is open to the extracellular surface, and in the M-type conformation (conformation C) it is open to the cytoplasmic surface (Kataoka et al., 1994; Brown et al., 1997). This structural transition after first proton transfer prevents reverse transfer of proton from D85 to the Schiff base. Thus, the alternating protein conformation model explains the proton transport mechanism (Lanyi, 1995).

I report here development of measurement methods for structural transitions in the reaction process. In section 2, the results on the structural transition from M intermediate to N intermediate in BR photocycle is reported. Time-resolved x-ray diffraction shows the difference between M and N intermediates. This difference between these intermediates is a contradictory point between two observations (Kamikubo et al., 1997; Subramaniam et al., 1998). Section 3 is a report on determination labeled atom positions using low resolution diffraction data. Section 4 shows the movement of labeled atom at G helices in BR photoreaction using the method described in section 3.

Section 2

Time-resolved X-ray Diffraction Study of Bacteriorhodopsin Photocycle.

2.1. INTRODUCTION.

Large structural changes in the M intermediate have been studied under stabilized conditions by neutron, x-ray, and electron diffraction methods (Dencher et al., 1989; Nakasako et al., 1991; Koch et al., 1991; Subramaniam et al., 1993). However these diffraction data are not consistent with each other. Dencher et al. (1989) reported that prominent changes are near helices F and G, and the change near helix B is less extensive. The data of Koch et al. (1991) was identical to the result of Dencher et al. (1989). On the other hand, Nakasako et al. (1991) showed that the most prominent structural change occurred near B and G helices. But these revealed structures of M intermediate differ from each other. Koch et al. (1991) revealed the structure of the M intermediate of D96N whose M intermediate has a long life. The difference Fourier map shows that the region near F and G helices changes its structure. Nakasako et al. (1991) showed, however, that the structure of Arg-HCl treated wild-type BR changes near B and G helices. Subramaniam et al. (1993) studied M intermediate structures of wild-type and D96G mutated BR which are trapped by rapid cooling during the photocycle. Their result was as follows; wild-type BR changed its structure near B and G helices in M intermediate, and D96G changed near F and G helices. Because the trapped wild-type included N intermediate, they concluded the structural change near F, G helices takes place in M intermediate and the change near B, G helices are N intermediate character. N intermediate structures were also revealed by x-ray and electron diffraction (Kamikubo et al. ,1996; Vonck, 1996). The structural change in N intermediate was observed near F and G helices. Moreover, Vonck (1996) showed F helix changes at the cytoplasmic end in N intermediate and indicated proton transfer channel at the cytoplasmic region opens to the aqueous phase in this state. As a consequence of these results, structural changes can be classified into two types; one is a characterized change near B and G, the other is near F and G. This disagreement was solved by my previous study (Kamikubo et al., 1996; Kamikubo et al., 1997). I observed two types of structural changes; M-type structure changes near B and G helix, and N-type structure changes F and G helix. Moreover in alkaline condition D96N mutant BR has the state that has a deprotonated Schiff bases and a N-type structure. This state was called MN intermediate. These results agree with the FTIR study of D96N (Sasaki et al., 1992). FTIR study revealed that in alkaline condition D96N has an N-type conformation with a

deprotonated Schiff base.

Recently, by using electron diffraction with rapid cooling Subramaniam et al. (1999) measured structural changes in intermediate states of wild-type, D96G, and other mutant BRs at varying times after excitation. Because they could not observe difference of M intermediate, N intermediate and O intermediate, they concluded the difference of these intermediate structures were trivial. But they could not measure diffraction patterns and absorbance changes on the same sample. I constructed a time-resolved x-ray diffraction measurement system for direct observation of the BR structural transition in its photocycle. I measured M-N transition of wild-type BR by time-resolved x-ray diffraction and absorbance and FTIR in the present study. I also report here a structural transition from M-type conformation to N-type conformation in the D96N photocycle by time-resolved x-ray experiments. In these experiments, structural transition from M-type to N-type was clearly observed. This is the first observation of the structural change using a diffraction method from M-type to N-type in real time measurement. I concluded that BR uses two step structural changes in the proton pumping.

Nomenclature. The photointermediates of BR were named from their spectra in the visible light region. Therefore, their names, K, L, M, N, O, originally indicated differences in the chromophore environment. Recently, these intermediates can be recognized also by FTIR and diffraction, which distinguish changes in the protein moiety as well as in the retinal. This situation has brought confusion to the discussion of the proton pump. In this paper, we use the following terminology. The M intermediate represents the intermediate with an unprotonated Schiff base, whose absorption maximum is near 410 nm. The N intermediate represents the intermediate that follows the M intermediate, which has a reprotonated Schiff base and an absorption maximum of 565 – 570 nm. The M-type and N-type conformations represent the protein structures of the M and N intermediates observed in the wild-type protein, respectively. It is possible to produce, however, the N-type conformation with an unprotonated Schiff base (M intermediate). This so-called MN intermediate (Sasaki et al., 1992, Kamikubo et al., 1997) is, thus, categorized as an M intermediate, although we will use the term MN intermediate occasionally, in its original meaning.

2.2. MATERIALS AND METHODS.

2.2.1. Purification of Bacteriorhodopsin.

2.2.1.1. Cultivation of Halobacterium Sarinalium.

Wild-type BR and D96N BR were used in the experiments. The cell that produces D96N BR (Ni et al., 1990; Needleman et al., 1991) was a kind gift from Dr. J. K. Lanyi. *Halobacterirum Sarinalium* was cultured as described by Oesterhelt and Stockenius (1974).

Compositions of Culture Fluid (pH7.2-7.4)(g/1L culture fluid)	
NaCl	250
$MgSO_4$ $7H_2O$	41
KCl	2
Trisodium Citric Acid	3
$CaCl_2$	0.2
Bacteriological Peptone (OXOID)	10

Agar media were prepared as follows. One litter culture fluid added to 15g Bacteriological Agar (OXOID) was autocraved with a stirring bar. After the temperature of the agar media went down bellow 60 °C, they were divided into culture dishes.

Ten μl of 100~1000 times diluted *Halobacterium Salinarium* culture fluid was spread onto agar media. The culture dishes of agar media were kept for about one month at 37 °C. One of *Halobacterium Salinarium* colonies was picked up by a platinum wire and put into 5 ml of a culture fluid. This culture was incubated in a shaker at 37 °C until it becomes muddy for about one week. Five ml of a culture fluid was added to 50 ml culture fluid and incubated in a shaker for further 2 or 3 days. About one fifth of the 50 ml culture was transferred into a 1L culture and incubated in a shaker for about 2 weeks.

2.2.1.2. Purification of bacteriorhodopsin.

The purple membranes were isolated by standard methods (Oesterhelt and Stockenius, 1974).

Procedure for Purple Membrane Purification

culture fluid
centrifugation (collection of bacteria)
(7000rpm, 30min, 4 °C)

↓

precipitate was pipetted with culture fluid without peptone and DNase1 was added. (10 µl of 1 mg/ml DNase1 solution was added to 30 ml culture.)

dialyze one day in distilled water (4 °C).

↓

centrifugation for removal of other cellular parts.

(3000 rpm, 30 min)

supernatant fluid is collected.

↓

ultracentrifugation

(25000-30000 rpm, 30-45 min, 4 °C)

precipitate is pipetted with 10 mM HEPES (pH 7.0).

this procedure is repeated until its supernatant becomes clear.

↓

sucrose density gradient.

linear sucrose gradient from 60 % to 40 %.

sucrose is ultracentrifuged with swing rotor.

(25000 rpm, 18 h, 4 °C,)

↓

sucrose removing with 10 mM HEPES (pH 7.0)

(25000-30000 rpm, 30min, 4 °C)

repeat this procedure 3 or 4 times.

2.2.2. Sample preparation for absorbance, FTIR and x-ray diffraction measurements.

The purple membranes with wild-type BR were suspended in 20 mM Tris (pH 9.0). The purple membranes with D96N BR were suspended in 10 mM HEPES or MOPS (pH 7.0). A 20 µl drop of suspension was dried on a piece of Mylar sheet, and another drop was layered onto the film. The layering procedure was repeated three times for x-ray diffraction experiments and one for optical measurements. This film was incubated at room temperature at a relative humidity of 95 % for 1 day.

For FTIR measurements, a 24 µl drop of wild-type PM suspension (20mM Tris pH9) was dried on a FBa cell, then the sample was incubated at room temperature at a relative humidity of 95 % for 1 day.

2.2.3. Absorbance measurements.

A light flash ($500 < \lambda < 600$ nm) induced absorbance changes at 410 nm and 570

nm in wild-type (pH 9) and D96N (pH7) BR. The sample was placed between a reference halogen lamp (Mega Light 100, Hoya-Schott) and a monochrometer (SPG-120S, SHIMADZU) with a photomultiplier (R928-09, Hamamatsu Photonics). The output signal was recorded by an ADC card (REX5054, RATOC System Inc.) connected to a Toshiba note PC. A xenon flash lamp with Toshiba Y50 and C50D filter excited the samples. Temperature of the sample was kept at 10 °C for wild-type and 25 °C for D96N. Time resolution of this experiment was 10 msec.

2.2.4. Time-resolved FTIR measurements.

I measured a flash induced infrared spectrum changes of wild-type (pH9) to confirm M-N transition. FTIR measurements was carried out with FTS6000 Spectrometer (BioRad). Time resolution was 133ms. A flash light for photo-excitation was the same as in the absorbance measurement. Sample cells were made of FBa. Cryostat (Oxford) was used to keep temperature at 10 °C. Sixteen different data sets were averaged. This averaged data were analyzed by singular value decomposition (see 2.2.7).

2.2.5. Time-resolved x-ray diffraction measurement system.

2.2.5.1. RIKEN beamline I (BL45XU) SAXS station at SPring8.

Time-resolved x-ray diffraction experiments were carried out at RIKEN Beamline I (BL45XU) small angle x-ray scattering station in SPring8 (Fujisawa et al., in press). This beamline is an undulator one with two branches. One is for protein crystallography and the other is for small angle x-ray scattering. The beam is split into the two branches by a diamond monochromator so that two experiments can be done simultaneously (Yamamoto et al., 1995). The small angle x-ray scattering branch was designed for studying small angle x-ray scattering of protein solution or fibrous subunits. The optics makes use of the good parallelism of the undulator beam in order to reduce parasitic scattering. The beamline consists of a double crystal monochromator and a K-B type focusing mirror system. The author joined to the beamline construction group, and helped beamline construction. X-ray intensity at a sample position is ~10^{12} photons/sec. The wavelength at this hutch is optimized at 1.0 Å.

2.2.5.2. X-ray detector.

X-ray diffraction profiles were recorded by a CCD camera (Hamamatsu Photonics, C4880-82) coupled with a 6-inch x-ray image intensifier (Hmamatsu Photonics, V5445P) (Amemiya et al., 1995). The role of the image intensifier is to match

the large size of an x-ray image to a limited size of the CCD image sensor, and to increase the number of visible light photons incident into the CCD for high detective quantum efficiency. The x-ray image intensifier has a 150 mm diameter beryllium entrance window. But the x-ray image intensifier has two disadvantages: nonunifom response and image distortion due to a rounded shape of the beryllium window (Amemiya et al., 1995; Fujisawa et al., 1999). The CCD has a 656 × 494 pixels size. The spatial resolution of this CCD with the x-ray image intensifier is about 230 μm. The maximum readout speed of a 656 × 494 pixel size image is 36.4msec/frame at fast reading mode (live mode). 400 × 400 pixel size images were recorded in my experiments. Use of small size images has two advantages in experiments. One is that only the image in the center of x-ray image intensifier is used: the nonuniformity of response and the image distortion are small near the center of the x-ray image intensifier. The other is that it reduces required computer memory size. The highest readout speed of this 400 × 400 pixel image is 30.5 msec/frame. The sequential mode of the CCD was used to read frames sequentially in time-resolved measurements. The x-ray image intensifier has an aperture control system to modify the amount of output visible light photons. There are 10 apertures. Aperture 1 has a largest area, and area size become a half as the index number increases. Area sizes of aperture from1 to 3 are larger than the size of lens that the CCD camera usually used. Aperture 4 converts 0.27 x-ray photons to 1 ADC count at CCD in live mode. Aperture 10 converts 17.2 x-ray photons to 1 ADC count at CCD in live mode. Output ADC counts are almost proportional to the aperture size.

One must correct the nonuniform response and the image distortion of data. The nonuniform response and the image distortion come from a rounded shape of the beryllium window so that alternation of the camera length changes the nonuniform response and the image distortion in the data. I corrected the image distortion of data as follows. I recorded diffraction patterns from purple membranes with this detector. These were averaged circularly (see 2.2.6.). Then the difference between peak positions in the data and these from calculated ideal data (lattice constant was 62.45 Å) (Grigorieff et al., 1996) was compared (Fig. 2.2). This difference was used for correction of the image distortion. I corrected the nonuniform response of data as follows. I recorded diffraction patterns from purple membranes both with this detector and with an imaging plate. These data were averaged circularly and intensity of each peaks was separated (see 2.2.6.). Then the intensities obtained using the CCD and the imaging plate were compared (Fig. 2.3). The intensity ratio between data from CCD and imaging plate was used for the correction of the nonuniform response.

2.2.6. Time-resolved X-ray Diffraction Experiments.

I constructed a time-resolved x-ray diffraction measurement system with x-ray image intensifier and CCD camera to study the M-N transition in BR photocycle. A xenon flash lamp was used to start the photocycle of BR. A delay pulse generator (DG535, Stanford Research Systems, or Stimlulator, Nihon Kohden) was used to make delay of the CCD camera acquisition and a flash lamp excitation. Camera length (distance from sample to detector) was 300 mm in my experiments. X-ray diffraction patterns up to 7 Å ((71) reflection) were recorded. The aperture size of the x-ray image intensifier was used 6. Using the aperture 6, the conversion ratio from x-ray photons to ADC counts is 1.08 photons/ADC. The data acquisition mode of the CCD camera was live-sequential mode. The size of image was set to 400 × 400 pixels. Two hundreds frames of diffraction images were recorded at 244 ms time resolution for wild-type BR, 122 ms for D96N. The samples were excited by a xenon flash lamp with Toshiba Y50 and C50D filters ($500<\lambda<600$nm) at 2.44 sec after the start of the diffraction measurement. Temperature was kept at 10 °C for wild-type and 25 °C for D96N. An ion chamber was used to measure x-ray intensity. The output signal was amplified by a current amplifier (Model 428, Keithly) and recorded. The frame timing of CCD and the flash timing were also recorded.

A sequential 2-dimensional ring diffraction patterns was averaged circularly to reduce into sequential 1-dimensional patterns. Sixteen different data sets of wild-type were averaged. Ten different data sets of D96N were averaged. Sequential 1-dimensional diffraction patterns were in m × n matrices. The elements of these matrices are the diffraction intensity of m points of S ($=2\sin\theta/\lambda$) and n time points. One hundreds sixty one columns include S from (11) reflection to (71), and 199 rows include all time points except the first point during which data error sometimes occurred. These matrices were analyzed by singular value decomposition (2.2.7.).

2.2.7. Singular value decomposition analysis.

2.2.7.1. Singular value decomposition analysis.

FTIR and x-ray diffraction data were analyzed by singular value decomposition (SVD) (see detail in Henry and Hofrichter (1992)). For an m × n matrix A of real elements ($m \geq n$) the SVD is defined by

$$\mathbf{A} = \mathbf{U}\mathbf{S}\mathbf{V}^{T} \qquad (1)$$

where U is an m × n matrix having the property that $\mathbf{U}^{T}\mathbf{U} = \mathbf{I}_n$, where $\mathbf{I}_n$ is the n × n identity matrix, V is an n × n matrix such that $\mathbf{V}^{T}\mathbf{V} = \mathbf{I}_n$, and S is a diagonal n × n matrix of nonnegative elements. The diagonal elements of S are called the singular values of A.

The columns of U and V are called the left and right singular vectors of A, respectively. The singular values are ordered along with the corresponding column of U and V so that $s_1 \geq s_2 \geq \cdots \geq s_n \geq 0$.

Given the matrix A with the decomposition shown in (1), the matrix product A^TA may be expressed as

$$\begin{aligned} A^TA &= (USV^T)^TUSV^T \\ &= VSU^TUSV^T \\ &= VS^2V^T \end{aligned} \quad (2)$$

The diagonal elements of S^2 are the eigenvalues, and the columns of V are the corresponding eigenvectors, of the matrix A^TA. By a derivation similar to that shown in equation (2), I can get a relation as follows.

$$AA^T = US^2U^T \quad (3)$$

Or, the columns of U are derived by calculating $U = AVS^{-1}$.

The diffraction from the each component was determined by the following. Given that B(s) is an $m \times r$ matrix containing diffraction pattern of the components as a function of s, and T(t) is an $n \times r$ matrix containing their fractional concentrations as a function of time t, the following relation is obtained.

$$A(s,t) = B(s)T(t)^T = USV^T$$

When λ is an eigenvalue of B^TBT^TT and v is an eigenvector,

$$B^TBT^TTv = \lambda v$$

Premultiplying this equation by T yields

$$\begin{aligned} TB^TBT^TTv &= T\lambda v \\ (TB^TBT^T)Tv &= \lambda(Tv) \\ A^TA\,(Tv) &= \lambda(Tv) \end{aligned}$$

From this equation and (2), r eigenvalues of B^TBT^TT are the square of the r nonzero singular values of A. Normalization of Tv yields the column of the matrix V corresponding to the singular value given by $\lambda^{1/2}$. If λ is an eigenvalue of T^TTB^TB, ω is an eigenvector,

$$A^TA\,(B\omega) = \lambda(B\omega)$$

From this equation and (3), U can be calculated from $B\omega$.

2.2.7.2. Singular value decomposition analysis to weighted data.

Before the SVD treatment, I consider the statistical weights for the data set A. The error of the data element $A(s_i,t_j)$ is described as σ_{ij}, and Σ is the matrix of σ_{ij}. The error of data A depends only on S but not on time because the measurement time slice is identical for all data and the intensity change is not so large. The σ_{ij} is given as the

average of $\sqrt{}$Aij for all time frame. Because diffraction intensity changes are much smaller than total intensity, the following relation holds.

$$\sigma_{ij} = \sigma_{ik} \text{ (i, j, k: arbitrary index)}$$

The weight matrix W is a diagonal matrix defined as next.

$$W_{ij} = 1/\sigma_{ij} \ (i=j)$$
$$= 0 \ (i \neq j)$$

W puts equal weights on all elements.

$$[W\Sigma]_{ij} = 1$$

So WA has uniformity weights. WA can be decomposed by SVD as follow.

$$WA = U_w SV^T = WUSV^T$$

Where $U = W^{-1}U_w$. So A can be written as follows.

$$A = USV^T$$

2.2.8. Reconstitution of extracted components

When r is the extracted number of component from SVD, the extracted signal components of V were fitted with exponential functions as

$$\begin{pmatrix} V1 \\ V2 \\ \vdots \\ Vr \end{pmatrix} = C \begin{pmatrix} 1 \\ \exp(-k_1 t) \\ \vdots \\ \exp(-k_{r-1} t) \end{pmatrix}$$

Where C is an $r \times r$ matrix. Each V component is weighted with a singular value in these fit. Decomposed spectra of diffraction profiles were reconstituted according to time constants as follows. Relation of original data matrix A and decomposed matrix B is as follows.

$$A = B \begin{pmatrix} 1 \\ \exp(-k_1 t) \\ \vdots \\ \exp(-k_{r-1} t) \end{pmatrix}$$

Where B is a $m \times r$ matrix. Theory of this fitting procedure is as follows.

The relation of three states of a molecules A, B, C is

$$A \xrightarrow{k_1} B \xrightarrow{k_2} C$$

Where k_1, and k_2 ($k_1 > k_2$) are rate constants. Fractional concentration of A(t), B(t), C(t) is calculated as follows.

$$dA/dt = -k_1 A$$
$$dB/dt = k_1 A - k_2 B$$

$$dC/dt = k_2B$$

Then,

$$A(t) = A_0\exp(-k_1t)$$

$$B(t) = -(k_1/(k_1-k_2))\,A_0\exp(-k_1t) + (B_0+(k_1/(k_1-k_2))\,A_0)\exp(-k_2t)$$

$$C(t) = 1 + (k_2/(k_1-k_2))\,A_0\exp(-k_1t) - (B_0+(k_1/(k_1-k_2))\,A_0)\exp(-k_2t)$$

A0, B0 is initial values of A(t), B(t).

When time dependences of fractional concentrations are written as above, signal intensity $I_{all}(x,t)$ at point x and time t can be written as:

$$I_{all}(x,t) = A(t)\,I_A(x) + B(t)\,I_B(x) + C(t)\,I_C(x)$$

$I_A(x)$, $I_B(x)$, $I_C(x)$ are the contributions to the total signal intensity from each component. This can be transformed as next.

$$I_{all}(x,t) = I_C(x) + (B_0 + (k_1/(k_1-k_2))A_0)(I_B(x) - I_C(x))\exp(-k_2t) + A_0[\,I_A(x) - (k_1/(k_1-k_2))\,I_B(x) + (k_2/(k_1-k_2))\,I_C(x)\,]\exp(-k_1t)$$

$$(3rd) = A_0[\,(I_A(x) - I_B(x)) - (k_2/(k_1-k_2))\,(I_B(x) - I_C(x))\,]\exp(-k_1t)$$

This relation is correct only when the model is true to the system.

In the case of x-ray diffraction, the relation of the signal intensities written above should be converted to a structure factor F.

$$F_{all}(k,t) = F_C + (B_0 + (k_1/(k_1-k_2))A_0)(F_B-F_C)\exp(-k_2t) + A_0[\,(F_A - F_B) - (k_2/(k_1-k_2))\,(F_B - F_C)\,]\exp(-k_1t)$$

Intensity of x-ray diffraction is square of the structure factor F. This I(k,t) is written as follows.

$$I(k,t) = |F_{all}|^2 = |F_C|^2 + 2(B_0 + (k_1/(k_1-k_2))A_0)\,(F_B-F_C)\cdot F_C\exp(-k_2t) + 2A_0[\,(F_A - F_B) - (k_2/(k_1-k_2))\,(F_B - F_C)\,]\cdot F_C\exp(-k_1t)$$

When $F_C >> (F_B-F_C)$, $F_C >> [\,(F_A - F_B) - (k_2/(k_1-k_2))\,(F_B - F_C)\,]$.

2.2.9. Difference Fourier Map.

I calculated difference Fourier maps from x-ray diffraction data as follows.

Reconstituted second and third components are added to the first component. These procedures were needed for peaks separations with gaussians. The purpose of background elimination was to extract the peaks of Bragg reflection which comes from two dimensional crystals of BR in purple membranes. Backgrounds were estimated by linking the points, where Bragg reflections didn't contribute, by a spline function (Press

et al., 1988). Then backgrounds were subtracted from data. Each peak was fitted with a gaussian, and each peak intensity was integrated. The nonunifomity of response, which originated in x-ray image intensifier, was corrected. Each intensity along the Debye-Scherrer ring was calculated.

I analyzed these intensities with difference Fourier to find the positions of structural changes. Because the intensity changes were small, I used next two approximations in the analysis.

1. Intensity ratios of the overlapped reflections, which have the same reflection plane distances, in intermediate states are the same as the ratios in the unphotolized state.
2. Phases of structure factors in intermediate states are the same as the phases in the unphotolized state.

Intensity ratios and phases from cryo-electron microscopy were used (Henderson et al., 1990).

Theory of difference Fourier (Blundel and Johnson, 1976).

When ρ_O is the electron density of the original state and ρ_I is that of the intermediate state, distribution of electron density in a unit cell is

$$\rho_O(x,y) = (1/A)\Sigma_{hk}F_O(hk)\exp[-2\pi i(hx+ky)+i\alpha_O(hk)]$$

$$\rho_I(x,y) = (1/A)\Sigma_{hk}F_I(hk)\exp[-2\pi i(hx+ky)+i\alpha_I(hk)]$$

Where F is an amplitude of the structure factor, α is a phase, A is an area of the unit cell. Since changes in ρ are small, α_I will not be very different from α_O so that the difference in the electron density may be approximated by

$$\rho_I(x,y) - \rho_O(x,y) = (1/A)\Sigma_{hk}\,[F_I(hk) - F_O(hk)]\exp[-2\pi i(hx+ky)+i\alpha_O(hk)]$$

It is necessary to estimate how this difference Fourier map differs from the true electron density represented by

$$\Delta\rho_{true} = (1/A)\Sigma_{hk}\,F_d(hk)\,\exp[-2\pi i(hx+ky)+i\alpha_d(hk)]$$

where, F_d and α_d is the amplitude and the phase of the structure factor of the difference density. Using a cosine rule,

$$F_I - F_O = F_d{}^2/(F_I + F_O) + 2\,F_I\,F_O\cos(\alpha_d - \alpha_O)/(F_I + F_O)$$

Hence,

$$(F_I - F_O)\exp(i\alpha_O) = F_d{}^2\exp(i\alpha_O)/(F_I + F_O) + F_O\,F_d\exp(i\alpha_O)/(F_I + F_O) + F_O\,F_d\exp[i(-\alpha_d + 2\alpha_O)]/(F_I + F_O)$$

Because F_I and $F_O >> F_d$, the first term will be small. The second term gives rise to the transform of F_d /2 in the electron density map. The third term gives rise to noise but since there is no any correlation between α_d and $2\alpha_O$ its contribution to the transform is

small. Hence,

$$\Delta\rho = (2/A)\Sigma_{hk}\,[F_I(hk) - F_O(hk)]\exp[-2\pi i(hx+ky)+i\alpha_O(hk)]$$

Error in difference Fourier.

Error in difference Fourier has two origins.

(1)The errors in intensity measurements. In a difference Fourier synthesis based on coefficient $2(F_I - F_O)$, the mean squared error is given by

$$\delta_{\Delta\rho}{}^2 = (4/A^2)\Sigma_{hk}(\sigma_{FI}{}^2 + \sigma_{FO}{}^2)$$

(2)The errors from the use of α_O instead of α_I in the difference Fourier. The third term of $(F_I - F_O)\exp(i\alpha_o)$ becomes noise.

$$\Delta\Delta\rho = (1/A)\,\Sigma_{hk}\,F_d\,\exp[-2\pi i(hx+ky) + i(-\alpha_d + 2\alpha_O)]$$

Since

$$\langle\Delta\Delta\rho^2\rangle = (1/A^2)\,\Sigma_{hk}\,|F_d|^2$$

Now $(F_I - F_O)\sim F_d\cos(\alpha_d - \alpha_o)$ and the average value of $\cos^2(\alpha_d - \alpha_O)=1/2$

$$\langle(F_I - F_O)^2\rangle \sim (1/2)\,\langle F_d{}^2\rangle$$

Hence

$$\langle\Delta\Delta\rho^2\rangle \sim (2/A^2)\,\Sigma_{hk}\,(F_I - F_O)^2$$

Then the total mean square error in the difference map is given by

$$\langle\Delta\Delta\rho^2\rangle_{total} = \langle\Delta\Delta\rho^2\rangle + \delta_{\Delta\rho}{}^2$$

Calculation of difference Fourier maps of purple membrane.

A purple membrane is a two dimensional crystal which has a space group P3. When x-ray is incident on purple membranes vertically, the diffraction pattern at small angle region has information on two dimensional electron density projected onto the membrane plane. Two dimensional electron density is as follows.

$$\rho(x,y) = (1/A)\,\Sigma_{hk}F(hk)\,\exp[-2\pi i(hx+ky) + i\alpha(hk)]$$

From Friedel's low, $\alpha(hk) = -\alpha(-h-k)$.

$$\rho(x,y) = (1/A)\,F(00) + (1/A)\,2\,\Sigma_{hk}F(hk)[\cos(2\pi(hx+ky)-\alpha(hk))]$$

Taking the symmetry into consideration, this equation can be transformed as follows.

$$\rho(x,y) = (1/A)\,F(00) + (1/A)\,2\,\Sigma_{hk}F(hk)[\cos(2\pi(hx+ky)-\alpha(hk)) + \cos(2\pi(kx+hy+ky)+\alpha(hk)) + \cos(2\pi(-hx-kx+hy)-\alpha(hk))]$$

Structure factor amplitude and phase of each reflection from cryo-electron microscopy (Henderson et al., 1990).

h	k	f(hk)	α(hk)
1	0	244	-27
1	1	1803	166
2	0	1570	-173
2	1	545	-129
1	2	1072	-34
3	0	670	104
2	2	1377	113
3	1	1686	176
1	3	558	111
4	0	1359	-78
3	2	1316	15
2	3	871	-39
4	1	1707	-48
1	4	1361	-50
5	0	2071	-14
3	3	164	-8
4	2	1016	91
2	4	2297	-119
5	1	563	30
1	5	1585	-96
6	0	1268	-13
4	3	2524	128
3	4	1553	145
5	2	1747	127
2	5	673	-177
6	1	1377	-30
1	6	458	25
7	0	1043	-107
5	3	555	155
3	5	1532	-87
6	2	599	-44
2	6	775	-154
7	1	962	-113
1	7	1347	154

2.3. RESULTS

2.3.1. Absorbance measurements.

Observable intermediates at this time resolution are limited to M intermediate or N intermediate. The increase of absorbance at 410 nm is an indication of deprotonation of the Schiff base, which is characteristic to M intermediate. In M intermediate, absorbance increases at 410 nm and decreases at 570 nm. In N intermediate, absorbance is unchanged at 410 nm and decreases at 570 nm (Váró and Lanyi, 1991b). Then fractional concentrations of these intermediate states can be estimated from absorbance changes at 410 nm and 570 nm.

Figure 2.5a shows absrobance changes in wild-type BR (pH9, 10°C) at 410 nm and 570 nm by a flash excitation (see 2.2.3.). This data shows clearly that decay processes are different at 570 nm and at 410 nm. This difference shows coexistence of M intermediate and N intermediate in the decay process. Figure 2.5b shows the fractional concentrations of M and N intermediates estimated from the data shown Fig. 2.5a. Decay kinetics of M intermediate shows two phases. Since the rate constant of the fast M component is 4.7 sec^{-1}, this component is difficult to detect in a measurement time resolution lower than 200 msec. The rate constant of the slow M intermediate is 0.91 sec^{-1}, and the rate constant of N intermediate is 0.27 sec^{-1}. Because the difference among these rate constants is larger than 3 times, it seems easy to separate M and N intermediates in other measurements.

The life time of the M intermediate for D96N mutant bR at pH 7 is 100 times slower than that of wild-type, because D96N lacks the proton donor for the Schiff base (Miller and Oestehelt, 1990). Figure 2.6a shows absorbance changes at 570 nm and 410 nm after a flash excitation for D96N (pH7, 25°C) (see 2.2.3.). The kinetics is consistent with the earlier observation (Miller and Oesterhelt, 1990). They showed the decay time of D96N (pH7, 0.1M ion) is 1 sec. This value is smaller than my results. Since my samples are concentrated, ionic strength tends to increase. Increase in ionic strength retards M intermediate decay (Miller and Oesterhelt, 1990). Figure 2.6b shows the estimated fractional concentrations of M and N intermediates. This shows that D96N generates mostly M intermediate in this condition. Using FTIR, however, it is clarified that the yellowish state of D96N possesses the N-type protein conformation (MN intermediate) (Sasaki et al., 1992). I revealed that D96N can take both the M-type protein conformation (M intermediate) and MN intermediate (Kamikubo et al., 1997). Therefore, under my experimental condition, the initial state after the flash excitation may be a mixture of M and MN intermediates.

2.3.2. Time-resolved FTIR measurement.

Time-resolved FTIR measurement after a flash excitation was carried out for wild-type BR (pH9, 10°C) (see 2.2.4.). Figure 2.8 shows a part of data. This data was analyzed with SVD (see 2.2.7.). Figure 2.8 shows the result of SVD analysis. Three components were clearly separated from the noise. This data wasn't simple as described in 2.2.8. Then, the function, which consists of a constant and 3 exponential functions, was fitted to 3 V spectra (Fig. 2.9). Each parameter is shown in the table.

	constant	k1 = 0.1626 ±0.0016	k2 = 0.5167 ±0.0095	k3 = 7.09 ±0.15
V1	0.00063 ±0.00017	0.1675 ±0.0020	0.0799 ±0.0022	-0.04476 ±0.00089
V2	0.02236 ±0.00064	0.1766 ±0.0040	-0.3553± ±0.0049	-0.4823 ±0.0056
V3	-0.0816 ±0.0020	0.203 ±0.010	-0.026 ±0.016	-0.550 ±0.019

Figure 2.10 shows reconstituted spectra (see 2.2.8.). The spectrum of the second component (k = 0.16 sec^{-1}) is the difference spectra of N intermediate, and the spectrum of the third component (k = 0.51 sec^{-1}) is mostly the M intermediate one (Sasaki et al., 1994). This means that the reaction model described in 2.2.8 can't be applicable to this decay process of wild-type BR (pH9, 10°C). The constant component might come from alkaline bleach in photoreaction, or the component could not go back to the original state in the measurement. Rate constant of the fastest component is almost the same as the inverse of the time resolution (0.133 sec). Spectrum of the fastest component seems like a difference spectrum of M and N intermediates. This component corresponds to the fast M component in the absorbance measurement. The decay constants of M and N intermediates in FTIR measurement are different from those in the absorbance measurements. This difference may be due to delicate sample conditions. But it is clear that M intermediate decays faster than N intermediate under this condition.

2.3.3. Time-resolved X-ray Diffraction Measurements.

In x-ray diffraction experiments, I used a two dimensional x-ray detector, an x-ray image intensifier with a cooled CCD camera (Amemiya et al., 1995). Because a and b axes of two dimensional crystals are not oriented in my samples, output data was a sequence of two dimensional ring patterns like in powder diffraction (Fig. 2.11). A series

of two-dimensional ring patterns obtained by the detector system were averaged circularly to obtain a series of one-dimensional diffraction profiles. Figure 2.12 shows an example of the time-resolved diffraction profiles summed over 16 independent data set for wild-type BR (pH9, 10°C). Ten x-ray diffraction data of D96N (pH7, 25°C) were also measured and summed out. Samples were illuminated by a xenon flash lamp to trigger its photocycle during measurements. Time resolution of the measurements was 244 ms for wild-type, 122 ms for D96N, which is sufficient to observe the decay process of M and N intermediate (Fig. 2.5, Fig. 2.6). In Fig. 2.12, the intensity changes of (11) and (20) reflection are clear, as well as those in other reflections. These decay kinetics are almost the same as in the absorbance measurements. Figure 2.13 and 2.14 shows the diffraction profile before and after the flash excitation. The changes in the intensities of reflections are similar to those in the earlier diffraction experiments (Koch et al., 1991; Kamikubo et al., 1997). Structural changes by the flash excitation are small when it is compared to the whole diffraction profiles. But they are much larger than errors in the data.

2.3.4. Singular value decomposition of time-resolved x-ray diffraction data.

I applied SVD treatment to the data shown in Fig. 2.12 to analyze the decay kinetics of wild-type and D96N BR. SVD analysis has been widely used for the characterization of the experimental data with various condition parameters (Henry and Horfrichter, 1992). In the SVD treatment, I used weighted data set (see 2.2.7.2.). The error of the data element $A(s_i,t_j)$ is given as the square root of the number of incident photons (Fig. 2.13). The error of data A depends only on S but not on time because the measurement times are identical for all frames and the intensity changes are small. The result of SVD analysis is shown in Fig. 2.15 to Fig. 2.23. Vn is the time course of the changes in the diffraction pattern, Un (or Uwn). Sn is the magnitude of the n-th signal.

The result of SVD analysis for wild-type BR (pH9, 10°C) is shown in Fig. 2.15 to Fig. 2.20. U and V spectra are shown in Fig. 2.17 and Fig 2.18. The 4th and the 5th V spectra, V4 and V5, have little time dependence, and the corresponding U spectra, U4 and U5, have little meaningful profiles. The 6th component and higher components are also independent on time (data not shown). These facts indicate that the components higher than the 4th component come from noises. On the other hand, the 1st to the 3rd components have significant time dependence as shown in the V spectra. The corresponding three U spectra have characteristic profiles. Therefore these three components are the signals coming from the structural changes in BR. Moreover, the

first three singular values are larger than other values, confirming that the first three components are signals and others are noises. The U1 is similar to the ordinary diffraction pattern from purple membrane except for its sign (this negative sign corresponds to the sign of V1). The corresponding V1 shows little time dependence, indicating that the U1 does not change during the photocycle. Thus, the first component is mainly composed of the time-independent base structure of BR. The U2 is similar to the difference diffraction profile between the photointermediate state and the unphotolized state which has been studied by diffraction methods under photosteady condition (Kamikubo et al., 1997). The V2, the time dependence of U2, shows a change by the flash excitation at time 0 and decays back to the unphotolized state. The 3rd component has smaller singular value than the 1st and the 2nd components, but distinguishable from noises. The existence of the 3rd component indicates that there are, at least, two different intermediate conformations in the decay process of wild-type BR after a flash excitation. Since the results of absorbance and FTIR measurements show the existence of M and N intermediates in this time region, two intermediate conformations correspond to these intermediates.

The result of SVD analysis for D96N (pH7, 25°C) is shown in Fig. 2.21 to Fig. 2.23. This result shows that the data of D96N has also three components. This means that the decay process of D96N has two different conformations as wild-type. Moreover first three U spectra of D96N are almost the same as these of wild-type. This identity indicates that D96N has the same two intermediate structures as wild-type. Then D96N should have two intermediate conformations, M-type conformation and N-type conformation. But D96N generate mostly M intermediate (which has a deprotonated Schiff base) under this condition (Fig. 2.6). Thus, these results indicate the existence of MN intermediate, which has a deprotonated Sciff base like M intermediate and a structure like N intermediate (Sasaki et al., 1992; Kamikubo et al., 1997).

Errors in SVD data (Henry and Hofrichter, 1976)

Henry and Hofrichter (1992) simulated SVD analysis for the data which include random noise.

(1) Singular value decomposition of random matrices

When n × n random matrices were analyzed by SVD, the distribution function of singular values is written as

$$P(x) = (1/\pi)(4 - x^2)^{1/2}; \qquad x \equiv s/\sigma n^{1/2}$$

This distribution is the so-called quarter-circle law. This law becomes a very good first-order description of the distribution of singular value for matrices larger than 100

$\times 100$.

The sizes of my data are almost 200×200, and $\sigma = 1$ because weighted data were analyzed. Then maximum of singular values which comes from noise are as

$$s = \sigma n^{1/2} (4 - \pi p^2)^{1/2}$$
$$= 1 \cdot 200^{1/2} (4 - 0)^{1/2}$$
$$\sim 28$$

This is almost the same as the fifth singular value in my SVD analyses (Fig. 2.15). The fourth components in my SVD analyses are taken as noise, but U4s look like U1s or U3s. When signal to noise ratio becomes better, this component will be absorbed by U1 or U3.

(2) Singular value decomposition of matrices which contain noise

Henry and Hofrichter simulated SVD analysis of data which contain random noise. The jth SVD component is described by

$$s_j \sim s_{j0} + (m+n-1)\sigma_r^2/2s_{j0} + \varepsilon_{sj}; \qquad [\mathrm{var}(\varepsilon_{sj}) = \sigma_r^2]$$
$$U_{ji} \sim U_{ji0} + \varepsilon U_{ji}/s_{j0}; \qquad [\mathrm{var}(\varepsilon U_{ji}) = (1 - U_{ji0}^2)\,\sigma_r^2]$$
$$V_{ji} \sim V_{ji0} + \varepsilon V_{ji}/s_{j0}; \qquad [\mathrm{var}(\varepsilon V_{ji}) = (1 - V_{ji0}^2)\,\sigma_r^2]$$

The values which have subscript 0 are the ideal values without random noise.

Since S3 of wild-type is 59, the third singular value of data without noise will be about 56. Then S3 is almost the same as ideal value. Since U spectra are normalized, U_{ji} is much smaller than 1. Then $(1 - U_{ji0}^2)$ is nearly equal to 1. Consequently, equations have been simplified.

$$s_j \sim s_{j0} + \varepsilon_{sj}; \qquad [\mathrm{var}(\varepsilon_{sj}) = \sigma_r^2]$$
$$U_{ji} \sim U_{ji0} + \varepsilon U_{ji}/s_{j0}; \qquad [\mathrm{var}(\varepsilon U_{ji}) = \sigma_r^2]$$
$$V_{ji} \sim V_{ji0} + \varepsilon V_{ji}/s_{j0}; \qquad [\mathrm{var}(\varepsilon V_{ji}) = \sigma_r^2]$$

Reconstitution of B spectra

Since the three components derived from the SVD analysis do not correspond directly to three independent states in the photocycle, I need to reconstitute the diffraction profiles for three states from the three components. Three V spectra were fitted by double exponential functions to decompose to three species depending on the decay rate. Since V1 has no time dependency, double exponential functions were fitted to V2 and V3.

$$\begin{pmatrix} V2 \\ V3 \end{pmatrix} = \mathbf{C} \begin{pmatrix} 1 \\ \exp(-k_1 t) \\ \exp(-k_2 t) \end{pmatrix}$$

Where **C** is a 2×3 matrix. Each parameter of wild-type is shown in next table.

	constant	k1= 0.1322± 0.0010	k2= 0.891± 0.020
V1	-0.070888 ± 6.7e-06		
V2	0.04237± 0.00020	-0.2489± 0.0016	-0.17941± 0.00189
V3	-0.0257± 0.0016	0.2820± 0.0074	-0.748± 0.014

Three components were reconstituted from this result. Three components are as follows; time independent component B0, decay component B1 (rate constant k1) and decay component B2 (rate constant k2).

Each parameter of D96N is shown in the next table.

	constant	k1= 0.3434± 0.0021	k2= 0.657± 0.020
V1	-0.070888± 1.1e-05		
V2	0.04068± 0.00011	-0.3480± 0.0039	0.0166± 0.0042
V3	-0.0343± 0.0015	1.000 ± 0.055	-1.373±0.051

Figure 2.20 and 2.23 shows three diffraction profiles obtained after reconstitution. The profile B0 corresponds to a base diffraction profile of the unphotolized state which is unchanged during the photocycle; profiles B1 and B2 are diffraction profiles of two different components which decayed after the flash excitation with different time constant. Just after the flash excitation, the x-ray diffraction profile is a summation of all three profiles, B0, B1 and B2.

Figure 2.20 shows the difference profiles of two decay components of wild-type, a slow one (k=0.132) and a fast one (k=0.89). Absorbance and FTIR measurements show that M intermediate decays fast and N intermediate decays slowly in wild-type (pH9, 10°C). Then the slow decay component (k=0.132) mainly corresponds to M intermediate and fast one (k=0.89) to N intermediate in Fig. 2.10. Slow and fast components are alike, but they have some remarkable differences. Especially the ratio between the magnitude of (11) negative peak to that of (20) positive peak is clearly different of slow and fast components. According to the result of Kamikubo et al. (1997), the intensity ratio of the negative peak of (11) to the positive of (20) is almost 1:1 for the M-type structure but it is 1:0 for the N-type structure under a photosteady state. In Fig. 2.20, the ratio for the slow component is 1:1 and that for the fast is 3:1. This also indicates that slow component mainly consists of M intermediate and the fast one of N intermediate.

In the case of D96N (Fig.2.23), the ratio of the magnitude of (11) negative peak to that of (20) positive peak is about 5:2 in the difference profile just after the flash excitation (which corresponds to summation of B1 and B2 in Fig. 2.23). Since the profile B2 decays faster than the profile B1, the difference profile becomes similar to B1 at the

near end of the reaction. The ratio between the intensities of (11) peak and (20) peak becomes 6:1 finally. The change in the intensity ratio of (11) to (20) has also been observed in the photosteady state of D96N (Kamikubo et al., 1997). My time-resolved experiment reveals that at least two distinct conformations exist in the photocycle of D96N. The structural properties of these two components are close to the M-type conformation and the N-type conformation. The structural transition from the M-type to the N-type conformation is an important constituent of the photocycle, which I demonstrated previously in a photosteady experiment (Kamikubo et al., 1997). Since the mutant D96N possesses mainly the deprotonated Schiff base in the present time region (Fig. 2.6), the observed structural transition would be from the M intermediate to the MN intermediate. Another possibility is that the M-type conformation decays faster than the N-type conformation.

2.3.5. Difference Fourier Maps

I analyzed these intensities by difference Fourier method and estimated the positions which showed large changes (see 2.2.9). In this analysis, I used reflections up to (51). These maps correspond to 10 Å resolution.

The peak intensities of wild-type BR.

h	k	B0	σ (B0)	B0+B1	σ (B0+B1)	B0+B2	σ (B0+B2)
1	0	0	0	0	0	0	0
1	1	7.478595	0.001338	7.088379	0.006182	7.295947	0.011944
2	0	3.118515	0.001139	3.308514	0.005107	3.338243	0.01018
2	1	1.250386	0.000829	1.289419	0.00361	1.311181	0.007338
3	0	0	0	0	0	0	0
2	2	0.779078	0.000948	0.757004	0.004161	0.754881	0.008483
3	1	1.737816	0.000925	1.734318	0.004065	1.748165	0.008315
4	0	0.737765	0.000595	0.664501	0.002635	0.691491	0.005313
3	2	0.767257	0.000467	0.911149	0.002274	0.860405	0.004269
4	1	1.58566	0.000617	1.350416	0.002795	1.483605	0.005352
5	0	1.213617	0.000629	1.301144	0.002835	1.26326	0.005647
3	3	0	0	0	0	0	0
4	2	2.130041	0.000806	2.122906	0.00355	2.193732	0.007283
5	1	0.779451	0.000664	0.8129	0.002876	0.779416	0.005848

The peak intensities of D96N BR.

h	k	B0	σ (B0)	B0+B1	σ (B0+B1)	B0+B2	σ (B0+B2)
1	0	0	0	0	0	0	0
1	1	7.487304	0.002815	6.340799	0.019	7.692979	0.022769
2	0	2.984342	0.002248	3.23783	0.013549	3.083004	0.016962
2	1	1.279354	0.001727	1.344104	0.00938	1.30842	0.012053
3	0	0	0	0	0	0	0
2	2	0.742279	0.002236	0.726899	0.010503	0.755797	0.014696
3	1	1.748009	0.002263	1.755978	0.010812	1.778208	0.014425
4	0	0.798165	0.00148	0.545972	0.007434	0.86888	0.009621
3	2	0.794614	0.001111	1.057251	0.006961	0.796513	0.007327
4	1	1.577066	0.001471	1.029501	0.007854	1.749952	0.010487
5	0	1.263402	0.001629	1.488559	0.008692	1.225494	0.010894
3	3	0	0	0	0	0	0
4	2	2.184648	0.002026	2.136889	0.010053	2.330503	0.013033
5	1	0.757468	0.001592	0.822847	0.007969	0.707349	0.01001

Figures 2.25a and 2.25b show the difference electron density maps of wild-type calculated from the slow and the fast components shown in Fig. 2.20. The changes near F and G helices are observed for the slow component (Fig. 2.25a), and the positive peak at outside of F helix is higher than that on G helix. This is a characteristic property for

the N intermediate (Kamikubo et al., 1996). On the other hand, the positive peak on G helix is observed for the fast component (Fig 2.25b). In this map, the positive peak at outside of F helix is lower than that on G helix. This indicates that F helix changes its structure during M-N transition. This feature is the same as the transition of M-type conformation to N-type conformation in alkaline D96N (Kamikubo et al., 1997).

Figures 2.26a and 2.26b show the difference electron density maps of D96N. The map of slow component (Fig. 2.26a) is almost the same as wild-type. A large peak is observed on F helix. On the contrary, a negative peak and a positive peak is observed on F in the map of fast component (Fig. 2.26b). This result is interpreted as follows. The positive peak of F helix is low just after the flash excitation (summation map of slow and fast components), then it increase as the fast component decay (map of slow component). This naturally implies that the electron density of F helix increases at the transition from M-type conformation (M intermediate) to N-type conformation (MN or N intermediate) (see 2.3.4, Fig. 2.23). This results is consistent with that of wild-type.

2.4. DISCUSSIONS

I measured structural changes of BR after a flash excitation by time-resolved x-ray diffraction. So far, only Koch et al. (1991) did time-resolved diffraction study on BR. They measured structural decay process of D96N M intermediate. But they could extract only one decay component during this process. Using electron diffraction with rapid cooling, Subramaniam et al. (1999) measured structural changes in intermediate states of wild-type, D96G, and other mutant BRs at varying times after excitation. They also could not observe the difference between M intermediate and N intermediate. On the contrary to these results, I could measure the structural M-N transition of wild-type BR (pH9, 10°C) as a change in the x-ray diffraction pattern. I employed SVD, which is used frequently in spectroscopy, for analyzing time-resolved x-ray data. This method is powerful in extracting a small amount of changes from data (Henry and Hofrichter, 1992). I first decomposed data by SVD analysis, then calculated difference Fourier maps. Considering the noise from map calculation, this method is much effective than decomposition from time-sequential difference Fourier maps.

I also measured structural changes of D96N BR (pH7, 25°C) after a flash excitation by time-resolved x-ray diffraction. The result indicates that D96N has the same two intermediate structures as wild-type. Then D96N has two intermediate conformations, M-type conformation and N-type conformation. This result agrees with the existence of MN intermediate, which has a deprotonated Schiff base like M intermediate and a structure like N intermediate in D96N alkaline condition (Sasaki et al., 1992; Kamikubo et al., 1997). Recently, Rödig et al. (1999) reported that MN intermediate of D96N was observed under neutral condition. Their experimental condition (D96N, pH7, 25°C) is the same as in my experiment. Both my and their results confirm the existence of the MN intermediate

I observed an increase of electron density at outside of F helix in M-N transition. This indicates that a part of F helix moves outward in M-N transition. The Schiff base is reprotonated from D96 during M to N transition. D96 is located in a hydrophobic environment and has unusually high pK, so it is protonated in the unphotolized state. This means that pK of D96 needs to decrease for transfer of proton to the Schiff base. So, an important event lowers the D96 pK is expected to occur in M to N transition. In this step, the structural changes in the cytoplasmic surface of BR were observed by EPR (Steinhoff et al., 1994; Thiogeir et al.. 1997). Especially, Thiogeir et al. (1997) showed clearly that EF loop moves in M-N transition. An electron diffraction experiment also shows the cytoplasmic end of F helix is open in the N intermediate (Vonck, 1996). She

showed a three dimensional difference Fourier map of N intermediate of mutant BR by electron diffraction of tilted specimen. These results indicate that the end of F helix moves outward in M-N transition. This transition corresponds to the opening of the proton transfer channel to the cytoplasmic surface. This change is considered to take water molecules into the proton channel in the cytoplasmic side and to lower the high pK of D96 (Kamikubo et al., 1997). It facilitates proton transfer from D96 to the retinal Schiff base. This idea agrees with the fact that M-N transition of wild-type and M-MN transition of D96N is influenced by the hydration of the samples (Váró et al., 1991; Cao et al., 1991; Kamikubo et al., 1997). Replacement of hydrophobic residues locating cytoplasmic proton channel, F219, F171, T46 elongate the lifetime of N intermediate. Moreover, T46V and F219L contains N like conformer at unphotolized state (Brown et al., 1993; Subramaniam et al., 1999). These residues are located near D96, especially the OH group of T46 is hydrogen bonding to the carboxyl group of D96 (Leucke et al.. 1998). These results suggest that perturbation of the environment of D96 stabilizes the hydrogen bond between D96 and neighbor water molecules (Yamazaki et al., 1995) and prevents the recovery of high pK of D96 which is needed for reprotonation of D96 in photocycle.

If the structural transition from M-type to N-type has the role of taking water molecule(s) into the proton channel and lowering the D96 pK value, proton transfer from D96 to Schiff base occurs after this structural transition. Therefore, MN intermediate may exist in the wild-type photocycle, but it probably decays immediately and is difficult to be detected.

Section 3

X-ray Diffraction Studies of Bacteriorhodopsin. Determination of the Positions of Mercury Label at Several Engineered Cysteine Residues.

3.1. INTRODUCTION

High resolution structure determination is an essential step to elucidate the molecular mechanism of the function of proteins. Generally, two powerful approaches are employed, X-ray crystallography and NMR solution structure analysis. For studies of membrane proteins, however, these two approaches are not always applicable, because of difficulties in the crystallization in the first case and constraint in the lipid environments in the second. Electron crystallography of two dimensional crystals has been successfully applied to the structural analysis of membrane proteins. Especially BR is the first membrane protein, the structure of which is solved to 3.5 Å resolution by electron crystallography (Henderson et al., 1990; Grigorieff et al., 1996). Henderson and coworkers have begun to extend their pioneering work to the structural analysis of the photointermediates of BR (Subramaniam et al., 1993).

X-ray and neutron diffraction of oriented sheets of purple membrane have provided useful structural information, more recently about the photointermediates (Henderson, 1975; Blaurock, 1975; Popot et al., 1989; Dencher et al., 1989; Koch et al., 1991; Nakasako et al., 1991; Kataoka et al., 1994; Kamikubo et al., 1996). So far reasonable projection maps for M and N intermediates have been presented. Although the projection maps are limited in resolution to 7 Å, they show quite good agreement with the projection maps from electron crystallography (Subramaniam et al., 1993). To reveal that a major structural change occurred in the photointermediates, X-ray diffraction is a useful and effective method. When a position of a specific amino acid can be marked in the projection map, I have an opportunity to see the change in the position of specific amino acid residue. This would be possible by heavy atom labeling (Krebs et al., 1993). In order to explore the movement of that position, I need to locate it accurately with a heavy atom.

Electron diffraction studies (Subramaniam et al., 1993; Vonck, 1996) demonstrated of tilted specimens that the most prominent structural change are observed in cytoplasmic half of BR. These structural changes are considered to have an important roles in the translocation of protons (Kataoka et al., 1994). The structure changes in the M (Nakasako et al, 1991), and more recently the N (Kamikubo et al, 1996), intermediates had been revealed by X-ray diffraction. These results showed

where structural change occurred. But, I cannot know how much the positions moves and how they moves. In two dimensional X-ray diffraction, further, I cannot distinguish the changes in cytoplasmic half from that in extracellular half. Although, if I can labeled heavy atom to a specific site, I can distinguish where the structural change occurs. Moreover, if I can measure the heavy atom labeled position accurately, I can quantitate how much its position moves in the structural change.

In the study of BR, heavy atom labeling techniques has been carried out to locate the labeled sites in the electron density map. Model calculations of this kind were performed by Plöhn and Büldt (1986). They showed labeled positions can be obtained with an accuracy ±1 Å. But, on experiment, heavy atom labeling technique has some difficulties in the determination of labeled residues or labeling at specific sites, and low intensity differences when the occupancy of heavy atom is low.

I show here results on specific heavy atom labeling of BR. I introduced cysteine residues, one at a time, into BR for the heavy atom labeling. I used cysteine mutants, F27C, L100C, T170C, F171C and I222C (Fig. 3.1). The substituted residues are located near the cytoplasmic ends of the helices A, C, F, F and G. These mutants were labeled with PCMB which specifically reacts with sulfhydryl group and produce mercaptide. This method realized specific sites labeling and high occupancy. Krebs et al. (Krebs et al., 1993) used this method for a loop region. The refined maps I obtained with this approach locate the labeled cysteines at the predicted places from the model of Grigorieff et al. (1996), in spite of the low resolution of the diffraction.

3.2. MATERIALS AND METHODS

Samples. The cysteine-substituted BR mutants, F27C, L100C, T170C, F171C, I222C were constructed by inserting the changed gene into a non-integrating vector with novobiocin resistance as the selective marker. *Halobacterium salinalium* was transformed as before (Ni et al, 1990; Needleman et al., 1991). These mutants were purified as PM sheets according to a standard method (Oesterhelt and Stockenius, 1974).

Heavy Atom Labeling. One mM PCMB was prepared in 50 mM buffer at pH 7.0 (Boyer, 1954). This solution (0.24 ml) was added to 3.0ml PM suspension (16 μM) in the same buffer and incubated for 1 day at room temperature to yield the mercuribenzoate derivatives. Then the samples were washed with 10 mM HEPES buffer at pH 7.0, and the extent of the reaction was followed by spectrometric assay (Boyer, 1954). The reactions complete within 1 hour.

X-ray Diffraction Experiments. A 20 μl of droplet of a 320 μM PM suspension was dried on a piece of aluminum foil about for half day, and the same procedure was repeated 6 or 7 times. The samples were equilibrated for 1 or 2 days at 92 % relative humidity. The X-ray diffraction experiments were carried out on labeled and non-labeled cysteine mutants at 10 °C, 180 sec in dark condition with the MUSCLE Diffractometer at BL-15A in the Photon Factory of the National Laboratory for High Energy Physics, Tsukuba, Japan (Amemiya et al., 1983). The diffraction profiles were recorded by a one dimensional position sensitive proportional counter. The data acquisition systems were as described (Nakasako, 1990; Nakasako et al., 1991; Kataoka et al., 1994).

Data Treatments. Background of diffraction profiles were calculated by spline interpolation (Press et al., 1988) of the data points where diffraction of purple membrane don't contribute. After correction by Lorentz factor and subtraction of the background scattering, I calculated the integral intensity of each Bragg reflection by profile-fitting with a non-linear asymmetric function (Nakasako.,1991). After normalizing, these data intensities of the same condition samples were averaged out and the standard deviation were calculated from the dispersion of these intensities. Next, difference Fourier maps between labeled and non-labeled were calculated before refinement, with phases and intensity ratios of the same h^2+hk+k^2 value derived from

electron cryo-microscopy data (Henderson et al., 1990).

Data Refinement. Electron distribution of label part mainly comes from mercury atom. So I treated the electron density distribution of mercuribenzoate as a Gaussian. Thus I could refine structure factors, using the labeled positions determined in this difference Fourier map as starting points. The least square calculation was based on Marquardt method (Press et al., 1988). A two dimensional Gaussian of mercury electron density at (x, y) can be transformed as follows.

$$f(hk) = A \exp(-BS^2) \exp[-2\pi i(hx+ky)]$$

f(hk):structure factor of mercuribenzoate

A : scale factor

B : temperature factor

S : scattering length, which depend on hk

in the case of BR

$$S=2 (h^2+hk+k^2)^{1/2}/3^{1/2}/a$$

a is lattice constant.

hk : Miller index

So, the calculated structure factor of the labeled sample F_H^{cal} (hk) is

$$\mathbf{F}_H^{cal} (hk) = \mathbf{F}_N (hk) + f(hk) \qquad (*1)$$

$\mathbf{F}_N$: observed structure factor of non-labeled sample

Hence, in refinement of first part ,I minimize the following quantity.

$$\chi^2 = \Sigma_{hk} [\{ | \mathbf{F}_H^{obs} (hk) | - k | \mathbf{F}_H^{cal} (hk) | \}^2 / (\sigma_H + \sigma_N)^2]$$

k : scale factor (nearly equal 1)

σ : standard deviation of $|\mathbf{F}|$

In this way I get the best fit of the electron density distribution function of heavy atom.

In x-ray powder diffraction, the diffraction intensities which have the same h^2+hk+k^2 values are overlapped. If the overlapped structure factors are $\mathbf{F}_H (h_1k_1)$, $\mathbf{F}_H (h_2k_2)$, the diffraction intensity can be written as

$$I(S) = | \mathbf{F}_H (h_1k_1) |^2 + | \mathbf{F}_H (h_2k_2) |^2 \qquad (*2)$$

$$S = S(h_1k_1) = S(h_2k_2)$$

These structure factors are devided by intensity ratios from electron cryo-microscopy data for wild-type BR (Grigorieff et al., 1996). So I can recalculate the dividing factor from (*1) and (*2) with $\mathbf{F}_N$ (hk) and the function of heavy atom, as second part of refinement.

The refinement procedure first and second part were repeated by turns until convergence. After refinement, I calculated difference Fourier map between non-

labeled data and refined labeled data. The peak positions are converted to scale by a scale factor of 2brd (Grigorieff et al., 1996), protein data bank data. Its lattice constant is 62.45 Å.

3.3. RESULTS

Heavy Atom Labeling. The reaction of PCMB with cysteine causes the increase of absorbance in UV region (Boyer, 1954). The completion of the reaction, thus, can be followed by the change of absorbance at 250 nm. The reaction of PCMB with cysteine residue for cysteine-substituted mutants were completed within 1 hour. The spectra for Hg-labeled and non-labeled 222C are shown in Fig. 3.2 as an example with the difference spectrum. The similar increase in UV region after mercury labeling was observed for the other cysteine-substituted mutants. This spectrum change comes from PCMB combined with cysteine.

X-ray Diffraction. X-ray diffraction patterns were recorded from oriented PM films of labeled and non-labeled cysteine mutants by 180 sec exposure. The diffraction patterns indicate that the lattice structure is not affected significantly by either cysteine substitution or mercury labeling. As is the case for the wild-type BR, Bragg reflections up to (71) reflection, which is correspond to 7 Å resolution, were clearly observed for all the mutants with and without mercury. X-ray diffraction experiments were repeated for the different sample preparation for 10 - 20 times, the numbers of the diffraction profiles processed were listed in Table 1. In order to estimate the integral intensity of each Bragg reflection, each diffraction profile was processed with the same procedure and averaged to calculate the standard deviation. The averaged intensities from labeled and non-labeled 222C are shown in Fig. 3.3. The differences between the intensities from labeled and non-labeled samples are clearly beyond the magnitudes of the error level. The intensities of (11), (31) and some other reflections are considerably larger in labeled sample, but those of (20), (43), (52) and another reflections are smaller. These differences are attributable to the labeled mercury electron density. Similarly, for all the other mutants, the clear differences between labeled and non-labeled sample were observed in the diffraction profiles (not shown).

The projection map was calculated with the intensity data mentioned above combined with the phase from electron microscopy (Henderson et al., 1990). The difference electron density map between labeled and non-labeled 222C is shown in Fig. 3.4a. Without any data refinement, a single distinct peak located between helices F and G is observed in a monomer. The other peaks are clearly of a noise level. According to the structure model of Grigorieff et al.(1996), I222 is at the cytoplasmic side of G helix which faced to F helix. I can regard the peak as the electron density of the labeled mercury. A single distinct peak can be observed in each difference map

near the expected position for the substituted cysteine residue for the other mutants.

Refinement of Labeled Positions. Data refinement procedures were performed to averaged data described in MATERIALS AND METHODS. All peak position refinements to each sample were converged. This converged peak positions of all labeled mutants are shown in Table 2(a). The refined difference map between labeled and non-labeled 222C is shown in Fig. 3.4b. The coordinates of positions in Table 2(a) and Fig. 3.4 are Cartesian. The origins are located at the center of Fig. 3.4. X and y axes increase to the right and upward. The sides of squares of Fig. 3.4 are 62.45 Å. The peaks of mercury electron density become sharper and more isotropic than before refinement. This isotropicity comes from using isotropic gaussian for data refinement. Naturally, atomic vibrations are anisotropic one, so it is better to use anisotropic gaussian for data refinement. But if I use anisotropic gaussian, the number of unknown parameters increasing make reliability of data refinement lower because of the small number of the data. Intensity dividing rate recalculation seems to increase unknown parameters. But these dividing rate depend on the parameters of refined gaussian, so this recalculation doesn't increase the number of parameters. The refined labeled positions are free from the refinement starting points if the starting point is located inside a circle of about 7 Å or more radius of the refined label position. The standard deviations of peak positions are less than 1 Å. The 222C peak position before refinement are (27.2, -0.1). This moved to (27.15, 0.86) after refinement, the moved distances were about 1 Å. Also other sample moved about from 0.4 Å to 2.4 Å after refinement.

Comparison with the Electron Diffraction Structure. Each Cα atom peak positions of the model by Grigorieff et al. (1996) are shown in Table. 2(b). The distance between the mercury and the Cα atom of a cysteine must be within 4.5 Å because of its bond length. Indeed, the distances between Cα atom of data of Grigorieff et al.(1996) and the mercury positions of my data were shorter than 4.5 Å in xy-plane (Table 2(b)). These mercury positions are reasonable in a view of the helix locations, and they almost overlap the residues (which are substituted in my mutants) in the model. The mercury locates δ position of the labeled cysteine residue. So I compared each mercury position to δ position atom of the wild-type BR model (Grigorieff et al., 1996). Table 2(c) shows δ position atoms of the wild-type BR model. Cδ2 positions of F27, L100, F171 in the model is same as position of labeled mercury positions in Table 2(a) within error level. T170 has no atom at δ position, so atoms of γ position are listed in Table 2(c). The

distance between Oγ1 position of T170 in the model and labeled mercury to 170C is about 1.5 Å. This length is almost same as one bondlength. In the case of F27, L100, T170, F171, the wild-type model and my data shows good agreement. The δ position atom of I222 shows differences above error level from my mercury position data. But this difference is only about 1.5 Å. This may come from that I used mutant BR and wild-type BR model was not estimated its error level. These positions of mercury and wild-type BR residues of F27, L100, T170, F171, I222 are shown in Fig. 3.5 at xy-plane. In the case of 170C and 222C, comparing the mercury positions and residues of structure model, the mercury positions face outward of BR monomer. This reason may results from bulky group of PCMB. The aromatic ring of PCMB cannot get into inner side of protein, so it is pushed outward to obstruction less direction.

Table 3.1. The number of averaged same condition samples. These data were averaged out after peak deconvolution and normalized, and standard deviation were calculated by these data dispersion.

	F27C	L100C	T170C	F171C	I222C
labeled	20	19	12	18	20
non-labeled	20	18	15	16	19

Table 3.2. (a) Refined peak positions. The unit of positions is Å.

	F27C	L100C	T170C	F171C	I222C
X	22.01±0.53	19.74±0.93	26.57±0.74	21.67±0.86	27.15±0.49
Y	-8.36±0.31	3.45±0.61	1.22±0.40	9.46±0.76	0.86±0.33

(b) Cα atom positions (Grigorieff et al., 1996) and projected distances onto XY plane between the Cα and labeled mercury positions.

	F27	L100	T170	F171C	I222
X	20.916	15.328	24.928	22.430	25.481
Y	-11.454	3.170	3.395	6.175	-0.993
distance	3.28	4.42	2.73	3.37	2.49

(c)Cδ atom positions (Grigorieff et al., 1996) of F27, F42, L100 ,I222 and Oγ1 Cγ2 of T170.

		F27	L100	171C	I222		T170
X	Cδ1	19.641	18.003	19.536	26.443	Oγ1	25.009
Y		-9.100	1.653	7.745	2.225		1.131
X	Cδ2	21.599	19.072	21.184		Cγ2	23.317
Y		-8.254	3.016	9.282			1.553

3.4. DISCUSSION

Krebs et al. (1993) used heavy atom labeling and X-ray diffraction to localize labeling site of the A103C mutant BR, 103rd residue located in the loop between C and D in the wild-type BR structure model (Grigorieff et al., 1996). They labeled substituted cysteine residue by PCMB, organic mercury reagent. PCMB specifically reacts with sulfhydryl group of cysteine residue, so a BR monomer was labeled with single mercury compound. They refined labeled position with good reproducibility. I improved their method on intensity ratio recalculation and apply this to mutant BRs substituted a single helical end residue to cysteine. These mercury positions were refined to accuracy under 1 Å. For getting accurate positions, I repeated independent experiments on same condition more than 10 times and averaged these data. The former procedure made error smaller and the latter made possible to estimate data dispersion including error comes from data treatment. So I could get accurate heavy atom positions and accumulate error sizes. Similarly intensity deviding ratio recalculation is necessary for me to pursuit getting precise positions.

Mercury positions and wild-type BR structure model (Grigorieff et al., 1996) are compared in Fig. 3.5. This figure shows clearly that the positions of mercury and δ atoms of the model are almost overlapped. Off course, I used heavy atom labeling and cysteine substitution, so I cannot compare my data directly to wild-type BR without thinking of this difference. But these consistency of my data and wild-type BR model shows the redundancy of protein structure allows cysteine substitution and heavy atom labeling to keep almost same structure as native protein. This method can be used for determination of a single heavy atom position only when structure is kept as native protein. The photocycle of bulky group labeled cysteine mutant BRs including 27C, 100C, 170C, 222C were investigated by Brown et al.(1995). The photocycles of 27C, 100C, 222Care almost unchanged by bulky group labeling, but 170C are retard N intermediate decay by labeling. Similarly 171C has prolonged N intermediate (Kamikubo et al, 1996) than wild-type BR. FTIR and diffraction method suggested that F helix of cytoplasimic region tilts outward in the N intermediates (Ludlam et al., 1995; Kamikubo et al, 1996; Vonck, 1996). These results shows that the motional freedom of helix F play an important role in N intermediate. But this change of photocycle don't influence this experiments. From my results and comparing to wild-type model (Grigorieff et al., 1996), this change is negligible on structure at neutral pH.

In the BR study heavy atom labeling technique has used to assign helices to electron density map (Seiff et al, 1986; Katre et al, 1984), but it is difficult to determine

labeled residues and to increase occupancy of the heavy atom. I report the method to solve these problems that is effective for constructing model structures when low resolution electron density maps are obtained. This method are also useful for residue assignments of membrane proteins whose 3 dimensional crystal cannot be available but 2 dimensional crystal can, such as rhodopsin (Schertler et al., 1993). If difficulty of these membrane protein expressions are solved, cysteine substitution and heavy atom labeling provide helices assignment in 2 dimensional projection electron density map. Another application of the method, I think BR photointermediate structure study. The studies of photointermediate structure by diffraction methods shows the electron density differences between ground states and intermediates states. From these data, the structural change occur near B and G helices in M intermediates (Nakasako et al., 1991), near F and G helices in N intermediates (Kamikubo et al, 1996; Vonck, 1996). They show only electron density changes, don't show position changes. Especially, X-ray diffraction of oriented purple membrane gives only the structure projected onto membrane plane. By X-ray diffraction I cannot distinguish the change in cytoplasmic half from in extracellular half. However, it is possible to identify the side where the structural change occur, if I can use this method described here to the photointemediate study. The heavy atom labeling is promising to characterize the structural change in more detail. By the 2 different states study of mercury labeled BR it is possible to know how much its position moves and how moves. In the N intermediate, it is thought that F helix of BR tilts outward to take water molecules into protein. But it was supposed by the electron density increase near outside of F helix end (Vonck, 1996). If I can introduce cysteine residue to F helix and label PCMB without any perturbation to photocycle and structure, I measure how much helix moves and how it moves. And I can know how B and G helices change by labeling to these helices, although these helices' changes have not yet shown how move.

Section 4

Conformational Change of Helix G in the Bacteriorhodopsin Photocycle: Investigation with Heavy Atom Labeling and X-ray Diffraction.

4.1. INTRODUCTION

Bacteriorhodopsin (BR) is a light driven proton pump in the purple membrane of *Halobacterium salinarium*. The photocycle of BR is initiated by absorption of a photon by the retinal chromophore. The photocycle can be described as a sequence of states, BR -> J -> K -> L -> M -> N -> O -> BR. The important steps for proton transfer in the photocycle are the deprotonation of the retinal Schiff base to D85, located to the extracellular side, which is the L to M transition, and the reprotonation of the Schiff base from D96, located to the cytoplasmic side, which is the M to N transition (reviewed most recently in Lanyi, 1997). Since the deprotonation and the reprotonation are closely related to the release and the uptake of a proton, global conformational change is expected to be part of the switch between the deprotonation and reprotonation steps (Kataoka et al., 1994; Lanyi, 1995, 1997).

The evidence for global structural changes of BR at the M or the N intermediate is from various laboratories (Dencher et al., 1989; Koch et al., 1991; Nakasako et al., 1991; Subramaniam et al., 1993; Kamikubo et al., 1996; Vonck 1996). These diffraction studies suggested that major changes occur at helices B, F and G. Later, it was revealed that the characteristics of the M intermediate are the changes near helices B and G, while the characteristics of the N intermediate are the changes near helices F and G (Kamikubo et al., 1997). FTIR study of the deprotonated state of D96N at alkaline pH suggested the existence of a substate termed the M_N intermediate, a state which already has the N type protein conformation but with a still deprotonated Schiff base (Sasaki et al., 1992). The M_N state was distinguished from the pure M state by X-ray diffraction as well (Kamikubo et al. 1997). A transition between two M substates (M_1 and M_2) has been proposed to account for the extracellular to the cytoplasmic change of the access of the Schiff base (Váró and Lanyi, 1991a). It has been confirmed that the major conformational change occurs during M_1 to M_2 transition (Sass et al., 1997). Further, a subtle but essential conformational change occurs during M_2 to N transition, which is hydration dependent (Kamikubo et al., 1997). The displacement of the E-F loop in change may be as high as 5 Å (Thorgeisson et al. 1997).

The structural change at helix F appears as a pair of positive and negative peaks. From this feature it seems that the cytoplasmic end of this helix moves away

from the main body of the protein. Subramaniam et al. (1993) suggested that the movement of helix F opens a channel to transport a proton from cytoplasmic surface into protein. Ludlam et al. (1995) suggested that the Y185 to P186 region may function as a hinge for this movement. Consequently, there is a possibility that some water molecules enter the cytoplasmic channel and lower the pK of D96 (Kamikubo et al., 1997). On the other hand, there have been few investigations on the structural changes at the other helices. Although all of the diffraction studies demonstrated a density change at helix G, the essence of this change remains unclear. Unlike the case of helix F, the change at helix G is characterized as a prominent positive peak without an accompanying unique and localized negative peak, that would be expected from a tilt. Instead, there are a series of small negative peaks (Subramaniam et al., 1993). The change at helix B is also characterized by a single distinct positive peak (Nakasako et al., 1991). In order to elucidate these structural changes in detail, experiments with higher resolution are required.

X-ray diffraction of heavy atom labeled BR is one of the promising methods to describe these structural changes in the required detail. If I can observe a change in a heavy atom position in a specific intermediate, the essence of the structural change can be described in terms of amino acid residues. For this purpose, I introduced a single cysteine residue replacement substitution to BR and the introduced cysteine was labeled with the organic mercury compound, *p*-chloromercuribenzoate (PCMB). It has been already demonstrated that the position of a heavy atom can be determined within 1 Å accuracy (Krebs et al., 1993; Oka et al., 1997). I found that the mercury atoms were located at the positions expected from the high resolution structure (Oka et al., 1997, Gregorieff et al., 1996). I have now extended the heavy atom labeling method to the study of the structural change in the BR photocycle. I focused on the change of helix G, using the I222C BR mutant. The results show that in the M_N intermediate the mercury label at C222 moves 2 Å toward helix F.

4.2. MATERIALS AND METHODS

Sample preparation.

The site specific mutation I222C was introduced into bop gene, and the changed gene was constructed by inserting the changed gene into a non-integrating vector with novobiocin resistance as the selective marker. *Halobacterium salinarium* was transformed as before (Ni et al., 1990; Needleman et al., 1991). The mutated protein was purified from *H. salinarium* as purple membrane (PM) sheets according to a standard method (Oesterhelt and Stoeckenius, 1974). PCMB labeling was described as before (Oka et al., 1997). PMs were suspended in 20mM Na_2CO_3/$NaHCO_3$ buffer (pH 9.5) containing 10 mM NaCl.

X-ray diffraction experiment

The PM films for the X-ray diffraction were prepared on mylar sheets as discribed (Kamikubo et al., 1996; Oka et al., 1997), and equilibrated at 84% relative humidity. To transfer Gdn-HCl into the films, they were soaked for 10 mins in a 100 mM Gdn-HCl solution (pH 9.5, containing 20 mM Na_2CO_3/$NaHCO_3$ and 10mM NaCl), and thereafter the excess solution was removed (Dencher et al., 1989; Hauss et al., 1994). The films were equilibrated at 84% relative humidity for about 1 day. X-ray diffraction experiments were carried out with the MUSCLE Diffractometer (Amemiya et al., 1985) installed at BL15A in the Photon Factory, using synchrotron radiation as described previously (Nakasako et al., 1991). X-ray diffraction profiles were recorded at the same position of the same specimen, with and without continuous illumination with a 1-kW slide projector, using a cut-off filter Y-51 (transmission > 510 nm, Toshiba). The temparature of the sample were kept 20°C. Exposure times were 180 sec. Data include up to the (7,1) reflection, which corresponds to 7 Å resolution.

Data Refinement

X-ray data treatments and analysis were described as before (Oka et al., 1997). The electron distribution of the label comes mainly from the mercury atom, and for this reason I treated the electron-density distribution of mercuribenzoate as a Gaussian. The structure factor of mercuribenzoate is

$$f(hk) = A \exp(-BS^2) \exp[-2\pi i (hx+ky)].$$

A and B are the scale factor and the temperature factor and h and k are Miller indices. Mercuribenzoate locates at (x, y). The structure factor of the labeled sample, $\mathbf{F}_H^{cal}(hk)$, is expressed as

$$F_H^{cal}(hk) = F_N(hk) + f(hk) \quad (1)$$

where F_N is the observed structure factor of non-labeled sample. In the first step of the refinement, the following quantity is minimized.

$$\chi^2 = \sum_{hk} \frac{[|F_H^{obs}(hk)|^2 - k|F_H^{cal}(hk)|^2]}{\sigma_H^2 + \sigma_N^2}$$

where k and σ are the scale factor (in this case, nearly equal to 1) and the standard deviation of the observed intensity. The heavy atom position is estimated by this procedure. In X-ray powder diffraction, the diffraction lines that have the same h^2+hk+k^2 values appear at the same position. Therefore, the observed integral intensity of such a reflection line is a sum of overlapping reflections. Given the structure factor of the overlapping reflections as $F_H(h_1k_1)$ and $F_H(h_2k_2)$, the observed diffraction intensity can be written as

$$I(S) = |F_H(h_1k_1)|^2 + |F_H(h_2k_2)|^2 \quad (2)$$

Each structure factor of overlapping reflection was evaluated using the intensity ratios for reflections with the same h^2+hk+k^2 for wild-type BR derived from cryoelectron microscopy data (Grigorieff et al., 1996). I recalculated the structure factors of the overlapping reflections for the labeled BR using Eqs. (Henderson et al., 1990), (2) and the structure factor of mercury, f(hk), as the second part of refinement. The first and second parts of the refinement procedure were iterated alternately until good convergence was obtained. Data of 10 measurements of labeled I222C and 8 measurements of non-labeled I222C were averaged, and the errors were estimated. Lattice constant used was 62.45 Å (Grigorieff et al., 1996). The phases of the electron cryo-microscopy data (Henderson et al., 1990) were used for the difference electron density maps. The refinements of the labeled positions were performed independently for the M_N and BR states.

FTIR measurements

The samples for Fourier transform infrared (FTIR) measurements were prepared under the same condition as for X-ray diffraction. A 6μl sample of labeled or non-labeled I222C BR suspended in 20mM Sodium Carbonate Buffer (pH9.5) containing 10mM NaCl was placed on a BaF_2 window (10mm diameter), and dried under gentle stream of N_2 gas. To transfer Gdn-HCl into the films, they were soaked for 10 minutes in a 100 mM Gdn-HCl solution (pH 9.5, containing 20 mM Na_2CO_3/$NaHCO_3$ and 10mM NaCl), and thereafter the excess solution was removed. The film was incubated under 84% relative humidity and sealed using silicone rubber spacer and another BaF_2 window. Spectral recordings were performed in a Horiba FT-210 Fourier

transform infrared spectrophotometer equipped with an MCT detector. The temperature of the sample were kept 20°C. The M_N intermediate was produced by irradiation of BR with >510-nm light for 30sec. Difference FTIR spectra were obtained for 2 minutes recording after irradiation.

4.3. RESULTS

The difference density maps calculated from the intensity differences between M_N and BR are given in Fig.4.1. The solid contour lines indicate regions of increased density and the dotted lines the regions of decreased density in the M_N state. The positions of the helices and the arrangement of the BR monomers in the trimer are also indicated. The difference of the positive peak height near helix F between M_N and BR is about 3%. The map of non-labeled I222C exhibits changes mainly at helices F and G with the minor change in helix B, which is the general property of N type structure (Kamikubo et al., 1997). The positive peak near helix F is paired with a negative feature between helices F and G. In contrast, the positive peak of helix G is surrounded several negative regions. These are same changes as in the D96N mutant and the Gdn-HCl treated wild-type BR at alkaline pH (Koch et al., 1991; Dencher et al., 1989). A change of density is seen also at helix B, but its amplitude is smaller. These features resemble the changes in the N intermediate (Kamikubo et al., 1996), consistent with the conclusion from FTIR results that M_N and N intermediates have similar structure (Sasaki et al., 1992). I had shown earlier that the structure of the M (M_2) intermediate is distinguishable from that of M_N or N, and the transition between the M type structure and the N type structure is hydration dependent (Kamikubo et al., 1997). In the present case, I used a relative humidity of 84% for the accumulation of the M_N intermediate, which seems rather low as compared with the previous study (Kamikubo et al., 1997). However, the diffraction and the FTIR spectra (Fig. 4.2) indicated the accumulation of the M_N intermediate. This would be partly because deliquescent Gdn-HCl brings sufficient water molecules to BR to accumulate the N type conformation at a lower vapor pressure.

The difference map of labeled I222C differs somewhat from the map of the non-labeled protein. The major difference is the lower amplitude of the change at helix G for the labeled protein. As discussed below, both Cys-222 and the label are located at helix G, and the movement of the mercury label from the region of density increase into the neighboring region of negative density change compensates for increase due to the protein. It seems that this accounts for the difference, and otherwise the two density maps are very similar.

Figure 4.2 shows the difference FTIR spectra between before and after illumination for the non-labeled and the labeled I222C BR. The experimental conditions are the same as that for X-ray diffraction measurements, except for the continuous illumination for diffraction. The two curves show the same features. There is a pair of

characteristic positive and negative amide I bands at 1650 and 1670 cm^{-1}. The COOH vibration of D85 is also observed at 1756cm^{-1}. These features are diagnostic for the N-type protein conformation (Pfefferlé et al, 1991; Ludlam et al, 1995). The deprotonated state of the Schiff base is clear from the fact that no positive peak is observed at 1186cm^{-1}. These FTIR evidences are consistent with the M_N intermediate state (Sasaki et al., 1992). It is confirmed by both difference Fourier map and difference FTIR spectra that the intermediate accumulated by illumination after Gdn-HCl treatment is the M_N intermediate.

The difference map between the labeled and non-labeled I222C in the BR state shows clearly the density of the mercury atom (Fig.4.3a). I can see the single peak of the mercury at helix G in each monomer. It is broader than the peak observed for neutral pH (Oka et al., 1997), but the peak positions are same. The map of mercury density in the M_N state is shown in Fig.4.3b. It shows that the position of the mercury moves in the M_N to BR transition. This is consistent with the change at helix G in Fig. 4.1. The 3D-difference map between N and BR shows the region near Ile-222 as changes mostly at helix G (Vonck, 1996). Since N has the same protein structure as M_N (Kamikubo et al., 1996), this result is in accord with the movement of mercury at Cys-222.

After the positions of the mercury were roughly estimated from the initial difference map, the position refinements were performed with the method as described above (Oka et al., 1997). The coordinates of the refined positions are listed in Table 1. The coordinate system employed is the same as that of Grigorieff et al. (1996). The errors of these data are smaller than 1 Å. The mercury peak position of BR state is the same as at neutral pH, within this error level (Oka et al., 1997). The mercury atom is located at the δ position of the cysteine residue. The position of the mercury differs by about 1.7 Å from Ile-222 δ atom in the wild-type BR structure (Grigorieff et al., 1996). This difference might arise from the labeling or the cysteine substitution.

The in-plane position of the mercury atom, and the wild-type BR residues (Grigorieff et al., 1996) from the 221st to the 223rd are shown in Fig.4.4. Although in the new structure model (Lueck et al., 1998), some region are different from the earlier structural model (Grigorieff et al., 1996), the structure of the region from the 221^{st} to the 223^{rd} is almost identical in these two structure model. I can see that the mercury atom is clearly moved in M_N relative to BR. The magnitude of the displacement of the mercury position in the BR to M_N transition is 2.1 ± 0.8 Å (Table 1). This value well exceeds the error level. The direction of the movement is toward the side of helix F that faces the center of the protein. The transition is from the positive region to the negative region in Fig.4.1a. This must be the reason why the positive peak is smaller in Fig.4.1b.

The line connected the center of the helix G of the BR state and the center of the positive peak is parallel to the displacement vector of the mercury. The distance between the center of the positive peak and the main chain of the helix G of the side of I222 to L223 is 2 Å, i.e., roughly equal to the mercury displacement, suggesting the shift of helix G during the BR to M_N transition.

Table 4.1. The refined coordinate of mercury atom positions in the M_N and BR states and its difference.

	BR	M_N	M_N minus BR
X	27.78 ± 0.72	26.88 ± 0.60	-0.90 ± 0.94
Y	1.15 ± 0.60	3.02 ± 0.41	1.87 ± 0.73

4.4. DISCUSSION

Labeling and diffraction methods have been applied to investigate BR structure. Plöhn and Büldt (1989) showed that these methods can produce the labeled atom position with high accuracy despite of the low resolution data. In fact, deuterium labeling and neutron diffraction has been used to investigate structural changes in the BR photocycle. Hauss et al. (1994) labeled retinal with deuterium and detected its tilt after photoisomerization. The position of PCMB label at cysteine substituted BRs have been studied at neutral pH in the unphotolyzed state (Krebs et al., 1993; Oka et al., 1997). These reports demonstrated that the mercury labeling method can provide precise information about the BR structure. I now used the same method with Gdn-HCl treated labeled I222C BR, and detected its position change during the photocycle. The error levels of the position of the label are almost same as those at neutral pH (Oka et al., 1997). I show that the single mercury atom moves 2.1 ± 0.8 Å in the M_N photointermediate. This is the first report on detecting a movement of a specific amino acid residue in the BR photocycle by heavy atom labeling.

A structural change of G helix was observed in the M and the N intermediates before (Dencher et al., 1989, Koch et al., 1991; Nakasako et al., 1992; Subramaniam et al., 1993; Vonck, 1996; Kamikubo et al., 1996). Recently, the high resolution BR structure has been reported by several groups using cryo-electron microscopy (Grigorieff et al., 1996; Kimura et al., 1997) and X-ray crystal structure analysis (Pebay-Peyroula et al., 1997, Luecke et al., 1998). According to these structures, helix G has a kink at around K216 to which retinal chromophore is bound. Vonck (1996) showed that the structural change of helix G occurs mainly in the cytoplasmic half of G helix starting from G220. The most changed part in helix G is the region around I222. The extracellular side of helix G changes less than the cytoplasmic side. The present result indicates that the region around I222 of helix G moves toward helix F. Hauss et al. (1994) demonstrated that the β-ionone ring of retinal moves little but the region near the Schiff base moves 1.4 ± 0.9 Å toward the β-ionone ring in the M_N intermediate, which is the same direction as the mercury movement revealed in this study. This suggests that the region between K216 and I222 in helix G moves cooperatively with the region near the Schiff base of the retinal. Takei et al. (1994) found that the side chain of K216 undergoes a conformational change during photocycle. The change of helix G thus may originate from the region of K216 and the retinal. The application of the mercury labeling to the other residues of helix G promises to reveal the properties of this change. Recently high resolution structure of M intermediate revealed by x-ray crystallography

(Leucke et al., 1999b). It shows that G helix near K216 moves toward retinal. This result agree with my study and the results of Takei et al. (1994).

If the position change for the mercury represents the change at helix G in Fig. 4.1, this change is a tilt of the helix toward inner side of F helix and the membrane normal. Thus, G helix would move toward the positive region in the difference map (Fig.4.4). If the helix tilts by as much as 2 Å, the change must appear as a pair of positive and negative peaks. But the positive peak at helix G is not accompanied by a single, localized feature of negative density in difference map. Instead, I see the positive peak surrounded by a large non-connected negative regions. It seems that the change of helix G is more complicated than a simple tilt. Subramaniam et al. (1993) had suggested that the cytoplasmic portion of helix G is more ordered in the intermediate state. Indeed, the 3-D difference map of N intermediate (Vonck, 1996), whose vertical resolution is 10.5 Å, showed that the most prominent positive change at helix G is at its cytoplasmic side, from about the 220th residue to the helical end, including the I222 residue. On the xy coordinate, the positive region overlaps with I222 and F219. In the high resolution structure of BR, helix G appears to bend near K216 that is linked to the retinal (Grigorieff et al., 1996; Kimura et al., 1997; Pebay-Peyroula et al., 1997; Leucke et al. 1998). This region of the helix may be mobile.

Section 5. Conclusion

I developed effective methods to study structural changes of BR during its photoreaction. I labeled mutant BRs with heavy atoms and determined positions of these heavy atom using low resolution x-ray diffraction data (section 3). This method is useful in locating residues in a protein, whose crystal diffracts only to low resolution. I applied this method to the MN intermediate state of BR (section 4). The result shows that a part of G helix moves toward inside of F helix. I also constructed time-resolved measurement system to observe the structural transitions in BR photocycle (section 2). I found M-N transition of BR in its photocycle by time-resolved X-ray diffraction. This structural transition is considered to control the pK of D96 which is important in protonation of the Schiff base.

The results of my researches and other evidence on BR structural changes in photoreaction are unified as follows. Retinal isomerizes from all-trans to 13-cis by photon absorption. At L-M transition, the Schiff base transfers its proton to D85 (Braiman et al., 1989). It is considered that the first global structural transition occurs at or after this step (Váró and Lanyi, 1991a; Kataoka et al., 1994; Sass et al., 1997), but there is no clear evidence. This structural transition after the first proton transfer prevents a proton reverse transfer from D85 to the Schiff base. Then a part of G helix moves toward inside of F helix (sectoin 4). This would correlate with the reformation of twisted retinal and make a proton transfer passway from D96 to the Schiff base. At M-N transition, the cytoplasmic end of F helix moves outward, and this movement makes environment of D96 hydrophilic and thereby decreases the pK value of D96 (section 2). At almost the same time, D96 transfers its proton to the Schiff base. Then D96 is reprotonated in N-O transition, and structure returns back to the original one at this step. At the end of photocycle, D85 transfers its proton to a part of the extracellular side. The proton transfer from the Schiff base to D85 causes first global structural change (L-M transition), and the second structural change causes proton transfer from D96 to the Schiff base (M-N transition). Localized changes (protonated state of the Schiff base) and global (structural) changes affect each other and realize proton transfer to one dirrection.

REFERENCES

Amemiya, Y., K. Wakabayashi, T. Hamanaka, T. Wakabayashi, T. Matsushita, and H. Hashizume. (1983). Nucl. Instrum. Meth. 208:471-477.

Amemiya, Y., Ito, K., Yagi, N., Asano, Y., Wakabayashi, K., Ueki, T., and Endo, T. (1995) Rev. Sci. Instrum. 66, 2290-2294.

Blaurock, A. E. (1975) J. Mol. Biol. 93, 139-158.

Blundell, T. L. and Johnson, L. N. (1976) "Protein Crystallography", Academic Press, London

Boyer, P. D. (1954) J. Am. Chem. Soc. 76, 4331-4337.

Braiman, M. S., Moigi, T., Marti, T., Stern, L., J., Khorana, H. G., and Rothschild, K. J. (1988) Biochemistry 27, 8516-8520

Brown, L. S., Zimanyi, L., Needleman, R., Ottolenghi, M., and Lanyi, J. K. (1993) Biochemistry 32, 7679-7685

Brown, L. S., Váró, G., Needleman, R., and Lanyi, J. K. (1995) Biopys. J. 69, 2103-2111.

Brown, L. S., Kamikubo, H., Zimanyi, L., Kataoka, M., Tokunaga, F., Verdegem, P., Lugtenburg, J., and Lanyi, J. K. (1997) Proc. Natl. Acad. Sci. USA 94, 5040-5044.

Butt, H. J., Fendler, K., Bamberg, E., Tittor, J., and Oesterhelr, D. (1989) EMBO J. 8, 1657-1663

Cao, Y., Váró, G., Chang, M., Ni, B., Needleman, R., and Lanyi, J. K. (1991) Biochemistry 30, 10972-10979.

Dencher, N. A., D. Dresselhaus, G. Zaccai, and G. Büldt. (1989). Proc. Natl. Acad. Sci. USA. 86:7876-7879.

Druckman, S., Ottolenghi, M., Pande, A., Pande, J., Cllender, R. H. (1982) Biochemistry 21, 4953-4959

Edman, K., Nollert, P., Royant, A., Belrhall, H., Pebay-Peyroula, E., Hadju, J., Neutze, R., and Landau, E. M. (1999) nature. 401, 822-826

Essen, T. N., Siegert, R., Lehman, W. D., and Oesterhelt, D. (1998) Proc. Natl. Acad. Sci. USA, 95, 11673-11678

Fujisawa, T., Inoue, K., Oka, T., Iwamoto, H., Uruga, T., Kumasaka, T., Inoko, Y., Yagi, N., Yamamoto, M., and Ueki, T. in press. J. Appl. Cryst.

Fujisawa, T, Inoko, Y., and Yagi, N. (1999). J. Synchrotron Rad. 6. 1106-1114

Grigorieff, N., T. A. Ceska, K. H. Downing, J. M. Baldwin, and R. Henderson. (1996). J. Mol. Biol. 259:393-421.

Haupts, U., Tittor, J., Bamberg, E., and Oesterhelt, D. (1997) Biochemistry 36, 2-7

Hauss, T., G. Büldt, M. P. Heyn, and N. A. Dencher. (1994) Proc. Natl. Acad. Sci. USA. 91, 11854-11858.

Henderson, R. (1975) J. Mol. Biol. 93, 123-138.
Henderson, R., J. Baldwin, T. A. Ceska, F. Zemlin, E. Beckmann, and K. H. Downing. (1990) J. Mol. Biol. 213, 899-929.
Henry, E. R., and Horfrichter J. (1992) Methods Enzymol. 210, 129-192.
Jardetzky, O. (1966) Nature 211, 969-970.
Kamikubo, H., Kataoka, M., Váró, G., Oka, T., Tokunaga, F., Needleman, R., and Lanyi, J. K. (1996) Proc. Natl. Acad. Sci. USA 93, 1386-1390.
Kamikubo, H., Oka, T., Imamoto, Y., Tokunaga, F., Lanyi, J. K., and Kataoka, M. (1997) Biochemistry 36, 12282-12287.
Kataoka, M., Kamikubo, H., Tokunaga, F., Brown, L. S., Yamazaki, Y., Maeda, A., Sheves, M., Needleman, R., and Lanyi, J. K. (1994) J. Mol. Biol. 243, 621-638.
Katre, N. V., J. Finer-Moore, and R. M. Stroud. (1984) Biophys. J. 46, 195-204.
Kimura, Y., D. G. Vassylyev, A. Miyazawa, A. Kidera, M. Matsushima, K. Mitsuoka, K. Murata, T. Hirai, and Y. Fujiyoshi. (1997). Nature. 389, 206-211.
Krebs, M. P., W. Behrens, R. Mollaaghababa, H. G. Khorana, and M. P. Heyn. (1993) Biochemistry. 32:12830-12834.
Koch, M. H., N. A. Dencher, D. Oesterhelt, H. -J. Plöhn, G. Rapp, and G. Büldt. (1991) EMBO J. 10, 521-526.
Lanyi, J. K. (1995) Nature 375, 461-463.
Leucke, H., Richter, H. T., and Lanyi, J. K. (1998) Science 280, 1934-1937
Leucke, H., Schobert, B., Richter, H.-T., Cartailler, J.-P., and Lanyi, J. K. (1999a) J. Mol. Biol. 291, 899-911
Leucke, H., Schobert, B., Richter, H.-T., Cartailler, J.-P., and Lanyi,J. K. (1999b) Science 286, 255-260
Ludlam, C. F. C., S. Sonar, C.-P. Lee, M. Coleman, J. Herzfeld, U. L. RajBhandary and K. J. Rothschild. (1995) Biochemistry. 34, 2-6.
Marti, T., Otto, H., Mogi, T., Rosselet, S. J., Heyn, M. P., and Khorana, H. G. (1991) J. Biol. Chem. 266, 6919-6929
Miller, A., and Oesterhelt, D. (1990) Biochim. Biophys. Acta. 1020, 57-64.
Nakasako, M, (1990) Ph.D. thesis (Tohoku University, Sendai) (Japanese).
Nakasako, M., M. Kataoka, Y. Amemiya, and F.Tokunaga. (1991) FEBS Lett. 292:73-75.
Ni, B., Chang, M., Duschl, A., Lanyi, J. K., and Needleman, R. (1990) Gene 90. 169-172.
Needleman, R., Chang, M., Ni, B., Váró, G., Fornes, J., White, S. H., and Lanyi, J. K. (1991) J. Biol. Chem. 266, 11478-11484.
Oesterhelt, D., and Stockenius, W. (1974) Methods Enzymol. 31, 667-678.
Oka, T., Kamikubo, H., Tokunaga, F., Lanyi, J. K., Needleman, R., and Kataoka, M.

(1997) Photochem. Photobiol. 66, 768-773.

Oka, T., Kamikubo, H., Tokunaga, F., Lanyi, J. K., Needleman, R., and Kataoka, M. (1999) Biophys. J. 76, 1018-1023

Papadopoulos , G., N. A. Dencher, G. Zaccai, and G. Büldt. (1990) J. Mol. Biol. 214:15-19.

Pebay-Peyroula, E., G. Rummel, J. P. Rosenbusch, E. M. Landau. (1997) Science. 277, 1676-1681.

Pfefferlé, J. M., A. Maeda, J. Sasaki, and T. Yoshizawa. (1991) Biochemistry. 30, 6548-6556.

Plöhn, H.-J., and G. Büldt. (1989) J. Appl Cryst. 19, 255-261.

Popot, J. L., D. M. Engelman, O. Gurel, and G. Zaccai. (1989) J. Mol. Biol. 210, 829-847.

Press, W. H., B. P. Flannery, S. A. Teukolsky, and W.T. Vetterling. (1988) Numerical Recipes in C. Cambridge University Press, New York.

Richter, H.-T., Brown, L. S., Needlema, R., Lanyi, J. K. (1996) Biochemistry 35, 4054-4062

Rödig, C., and Siebert, F. (1999) FEBS Lett. 445, 14-18.

Saraz, S., Oesterhelt, D., Ormos, P., (1994) Biopys. J. 67, 1706-1712

Sasaki, J., Shichida, Y., Lanyi, J. K., and Maeda, A. (1992) J. Biol. Chem. 267, 20782-20786.

Sasaki, J., Lanyi, J. K., Needleman, R., Yoshizawa, T., and Maeda, A. (1994) Biochemistry (1994) 33, 3178-3184.

Sass, H. J., I. W. Schachowa, G. Rapp, M. H. J. Koch, D. Oesterhelt, N. A. Dencher, and G. Büldt. (1997) EMBO J. 16, 1484-1491.

Schertler, G. F. X., C. Villa and R. Henderson (1993) Nature 362, 770-2

Seiff, F, I. Wallat, J. Westerhausen, and M. P. Heyn. (1986) Biophys. J. 50, 629-635.

Smith, S. O., Pardoen, J. A., Mulder, P. P. J., Curry, B., Lugtenburg, J., and Mathies, R. (1983) Biochemistry, 22, 6141-6148.

Smith, S. O., Lugtenburg, J., and Mathies, R. A. (1985) J. Membr. Biol. 85, 95-109

Steinhoff, H., Mollaaghababa, R., Altenbach, C., Hideg, K., Krebs, M., Khorana, H. G., and Hubbell, W. L. (1994) Science 266, 105-7.

Subramaniam, S., M. Gerstein, D. Oesterhelt, and R. Henderson. (1993) EMBO J. 12, 1-8.

Subramaniam, S., Lindahl, M., Bullough, P., Faruqi, W., Tittor, J., Oesterhelt, D., Brown, L., Lanyi, J., and Henderson, R. (1999) J. Mol. Biol. 287, 145-161

Takei, H., Y. Gat, Z. Rothman, A. Lewis, and M. Sheves. (1994) J. Biol. Chem. 269,

7387-7389.

Thogeirsson, T. E., Xiao, W., Brown, L. S., Needleman, R., Lanyi, J. K., and Shin, Y.-K. (1997) J. Mol. Biol. 273, 951-957.

Váró, G., and Lanyi, J. K. (1991a) Biochemistry 30, 5008-5015.

Váró, G., and Lanyi, J. K. (1991b) Biophys. J. 59, 313-322.

Vonck, J., (1996) Biochemistry 35, 5870-5878.

Yamazaki, Y., Hatanaka, M., Kandori, H., Sasaki, J., Karstens, W. F. J., Raap, J., Lugtenburg, J., Bizounok, M., Herzfeld, J., Needleman, R., Lanyi, J. K., and Maeda, A. (1995) 34, 7088-7093

Yamamoto, M., Fujisawa, T., Nakasako, M., Tanaka, T., Uruga, T., Kimura, H., Yamaoka, H., Inoue, Y., Iwasaki, H., Ishikawa, T., Kitamura, H., and Ueki, T. (1995) Rev. Sci. Instrum. 66, 1833-1835.

Yamazaki, Y., H. Kandori, R. Needleman, J. K. Lanyi, and A. Maeda. (1998) Biochemistry. 37, 1559-1564.

List of related publications

"Structures of photointermediates of bacteriorhodopsin and the molecular mechanism of proton pump"
Oka T., Kamikubo, H., and Kataoka, M.
Journal of the Japanese Society for Synchrotron Radiation Research (1999) 12, 184-193

"Conformational change of helix G in the bacteriorhodopsin photocycle: investigation with heavy atom labeling and x-ray diffraction"
Oka, T., Kamikubo, H., Tokunaga, F., Lanyi, J. K., Needleman, R., and Kataoka, M.
Biophyscal Journal (1999) 76, 1018-1023

"X-ray diffraction studies of bacteriorhodopsin. determination of the positions of mercury label at several engineered cystein residues"
Oka, T., Kamikubo, H., Tokunaga, F., Lanyi, J. K., Needleman, R., and Kataoka, M.
Photochemistry and Photobiology (1997) 66, 768-773.

"Small-angle x-ray scattering station at the SPring-8 RIKEN beamline"
Fujisawa, T., Inoue, K., Oka, T., Iwamoto, H., Uruga, T., Kumasaka, T., Inoko, Y., Yagi, N., Yamamoto, M., and Ueki, T.
Journal of Applied Crystallography. in press.

"The last phase of the reprotonation switch in bacteriorhodopsin: the transition between the M-type and the N-type protein conformation depends on hydration"
Kamikubo, H., Oka, T., Imamoto, Y.. Tokunaga, F., Lanyi, J. K., and Kataoka, M.
Biochemistry (1997) 36, 12282-12287.

"Structure of the N intermediate of bacteriorhodopsin revealed by x-ray diffraction"
Kamikubo, H., Kataoka, M., Váró, G., Oka, T., Tokunaga, F., Needleman, R., and Lanyi, J. K.
Proceedings of National Academy of Science USA (1996) 93, 1386-1390.

Acknowledgements

The author thanks Professor Mikio Kataoka (NAIST) for his supports and discussions. The author thanks Professor Fumio Tokunaga (Osaka University) for his supports and discussions. The author thanks Doctor Naoto Yagi (JASRI) for his supports and discussions of the experiments at SPring8. The author thanks Doctor Tetsuro Fujisawa (RIKEN) for his supports of the experiments at BL45A (SPring8). The author thanks Doctor Hironari Kamikubo (KEK) for his supports and discussions. The author thanks Professor Janos K. Lanyi (University of California, Irvine) and Professor Richard Needleman (Wayne State University) for their suppliances of the mutant BRs.

The author thanks Professor Takamitsu Yamanaka (Osaka University), Professor Syuichi Kinoshita (Osaka university) and Associate Professor Osamu Hisatomi (Osaka University) for their discussions in the examination of the doctor of science.

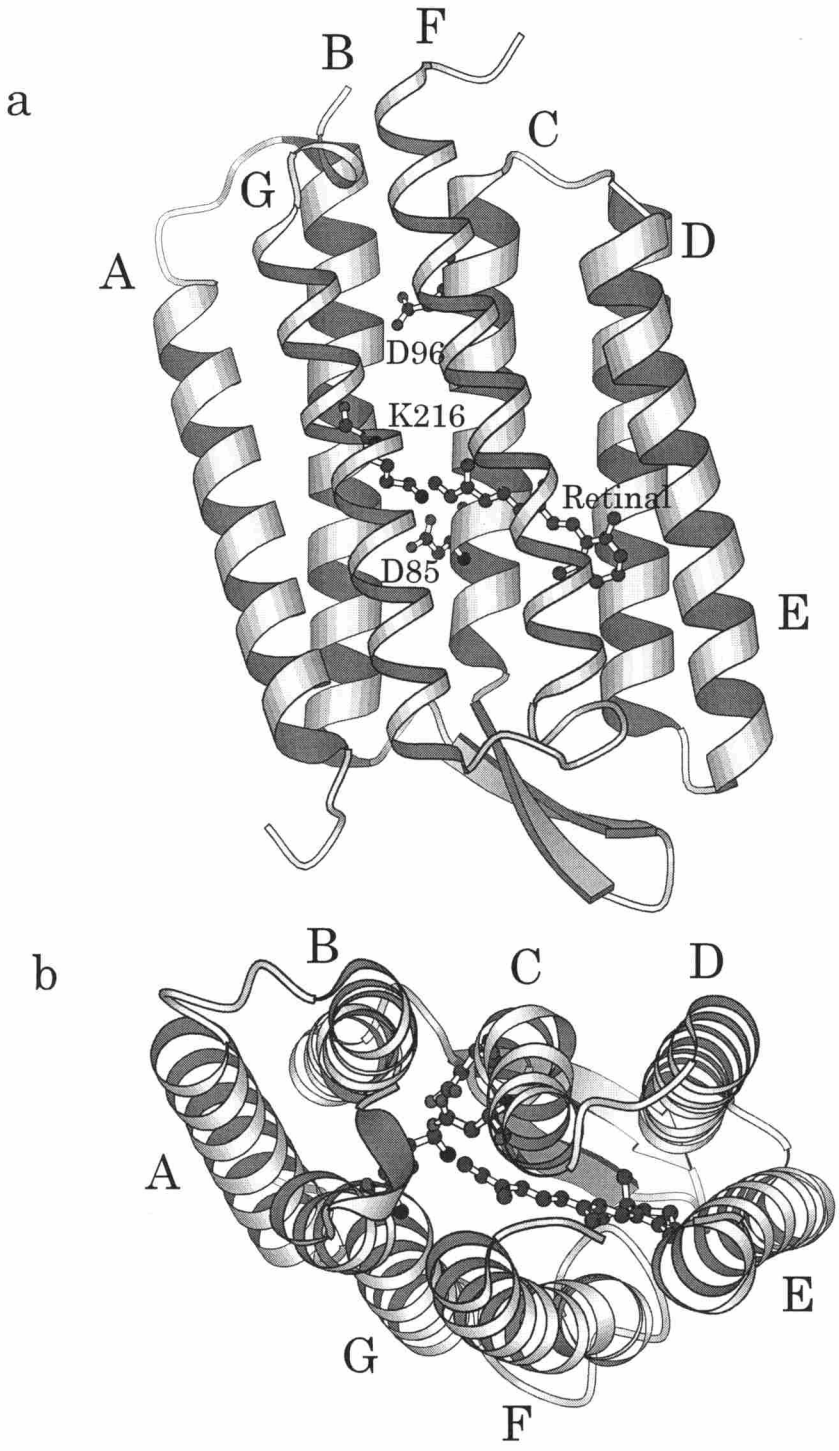

Figure 1.1. Structure of BR (Leucke et al., 1999a). A BR molecule consists of 248 amino acids and forms 7 trans-membrane a-helices. Seven a-helices and side chains of D85, D96, K216 and retinal are shown. (a) Side view of whole structure. (b) Projected view onto membrane plane. BR transports proton (hydrogen ion) from the cytoplasmic side to the extracellular side using the absorbed photon energy. BR is the smallest and the simplest photo-energy conversion system in all of living organisms.

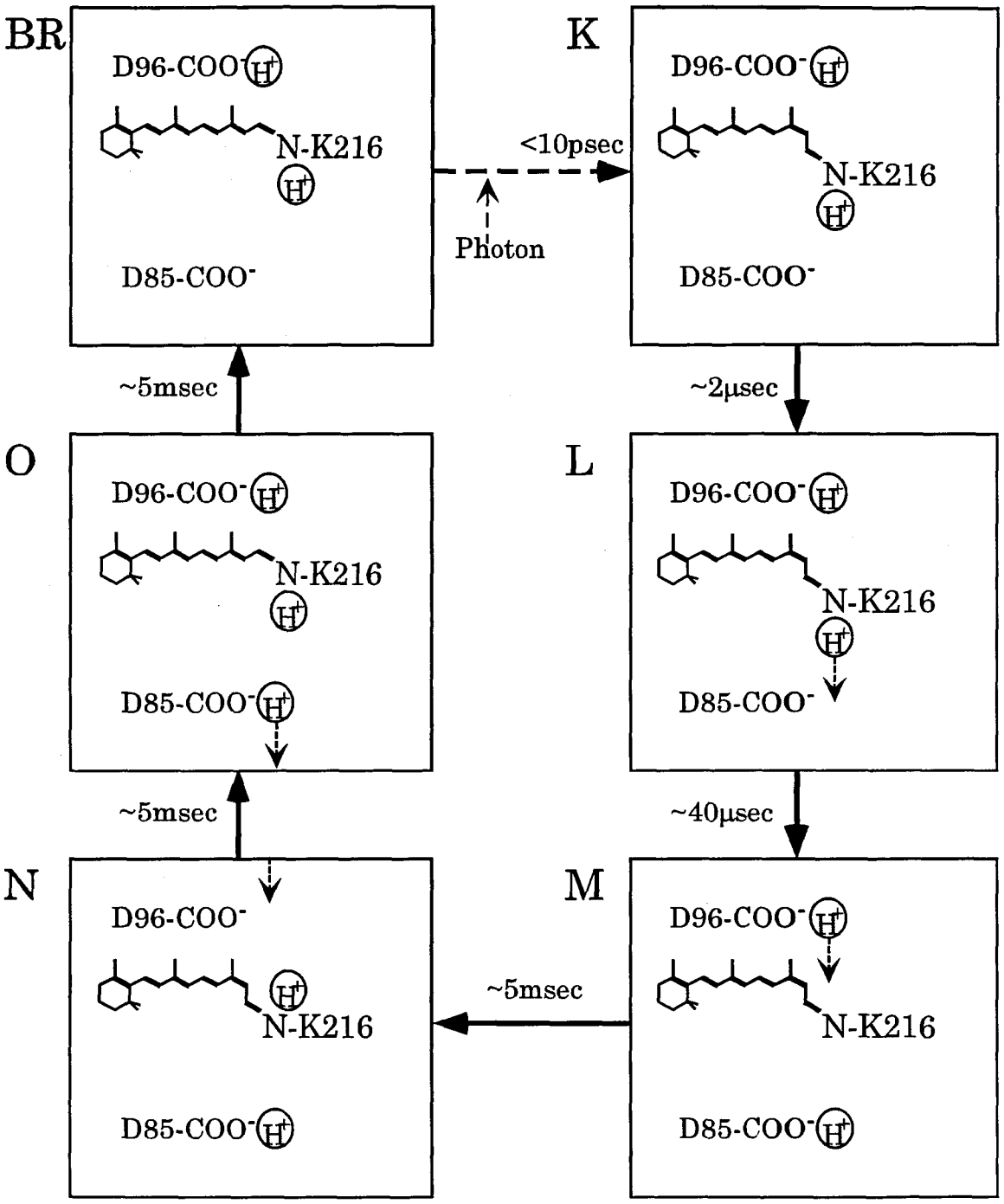

Figure 1.2. Photo-intermediate states of BR and the state of key residues in proton pump.

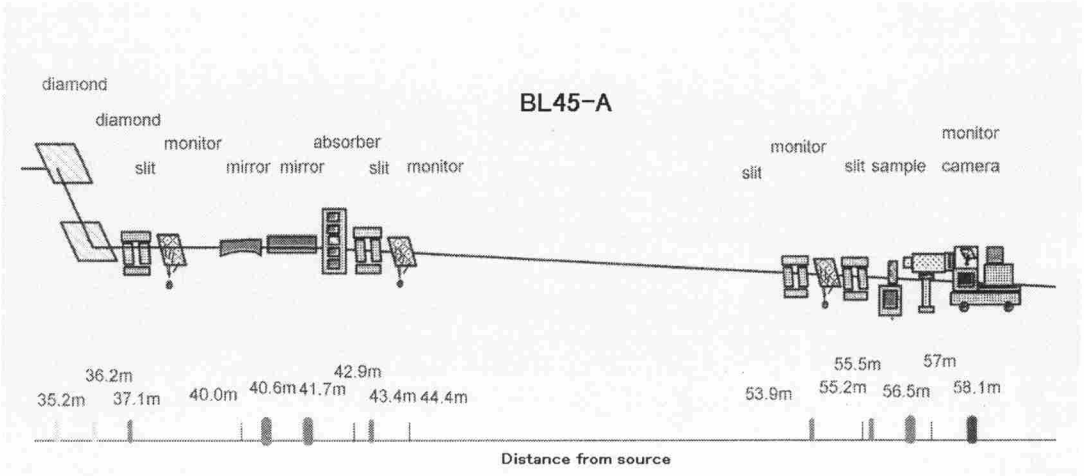

Figure 2.1. Beamline layout of BL45XU-A. An x-ray source is a vertically polarized tandem undulator. X-ray from source is monochromatized by a diamond monochromator, which locates around 36 m from x-ray source. Then x-ray beam is focused onto a detector plane (~58 m) by two Rhodium coated K-B type mirrors (~40 m). Four slits eliminate parasitic scattering from optical components. Components from 35 m to 44 m are in the optical hutch, and another components from 53 m to 58 m are in the experimental hutch A for small-angle x-ray scattering.

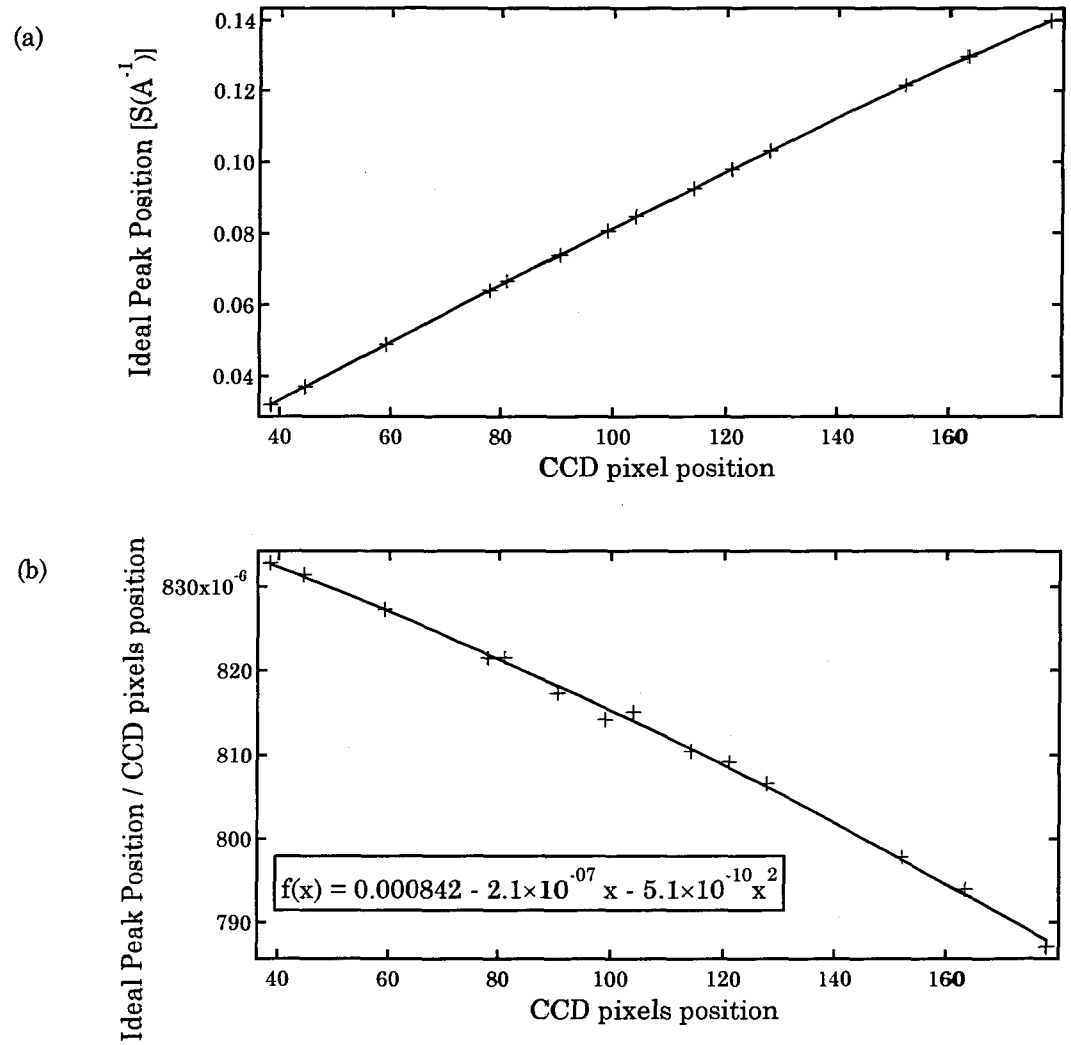

Figure 2.2. Deviation plot of Bragg reflection from ideal position. (a) X-axis indicates observed Bragg peak positions from center of the CCD pixel, y-axis indicates ideal positions of Bragg peaks. If x-ray image intensifier has no distortion, plots must be on a line, which pass the origin. (b) X-axis is same as (a), y-axis is ideal peak positions divided by observed position. This plot must be a barwise line, if x-ray image intensifier has no distortion. This plot was fitted with a polynomial function to get the correction function for image distortion.

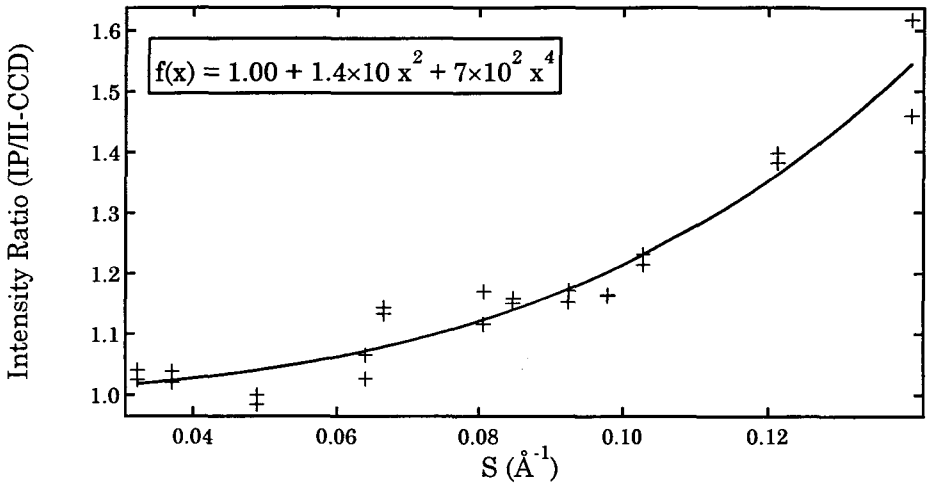

h	k	ratio
1	0	1.00488
1	1	1.01513
2	0	1.0205
2	1	1.0376
3	0	1.04982
2	2	1.06938
3	1	1.07623
4	0	1.09775
3	2	1.12076
4	1	1.13691
5	0	1.17119
3	3	1.18931
4	2	1.19861
5	1	1.22752
6	0	1.27897
4	3	1.28975
5	2	1.31181
6	1	1.35789
7	0	1.43193
6	2	1.47116
7	1	1.53982

Figure 2.3. Figure shows intensity ratio between IP and CCD with x-ray image intensifier. Intensity was the integrated x-ray diffraction intensity of Bragg reflections from purple membrane. Same samples were used in IP and CCD to record same diffractions. IP has uniformity of response. This plot was fitted with polynomial function to get the intensity correction function of nonuniformity. Calculated intensity correction table is also shown.

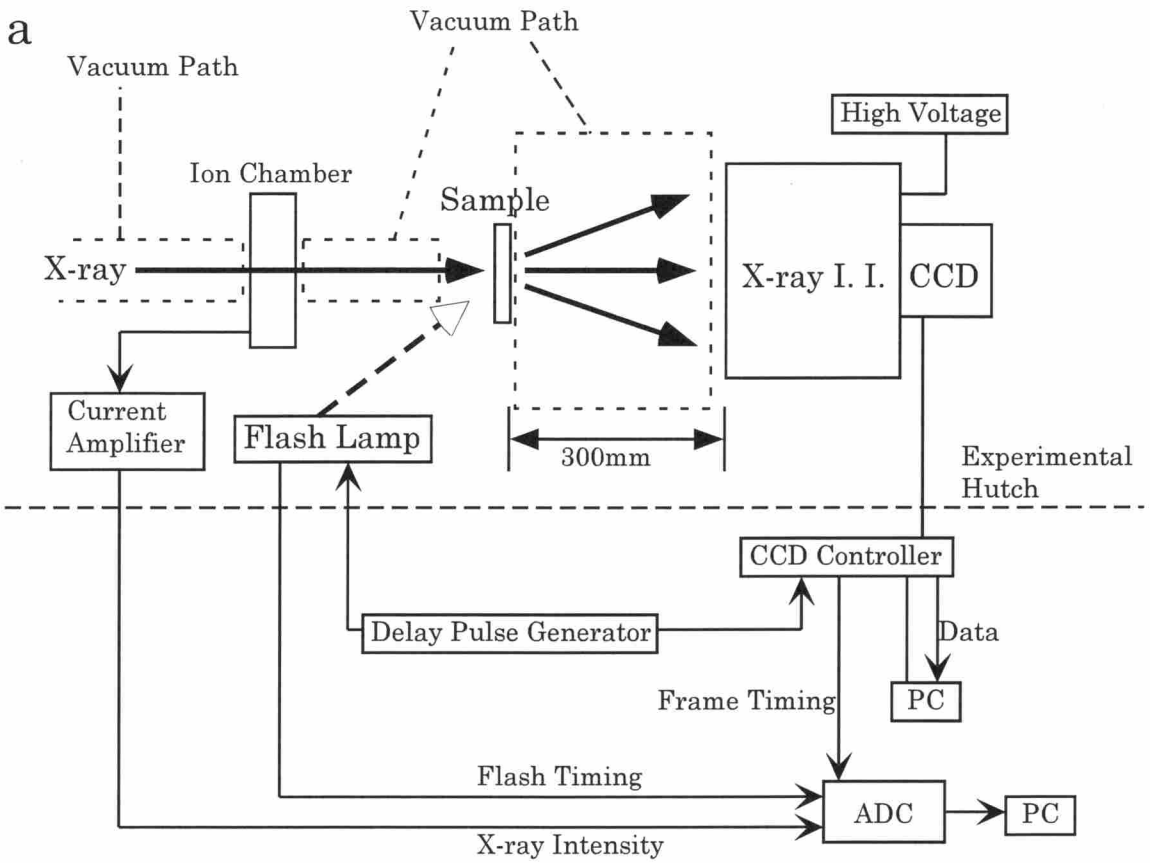

b

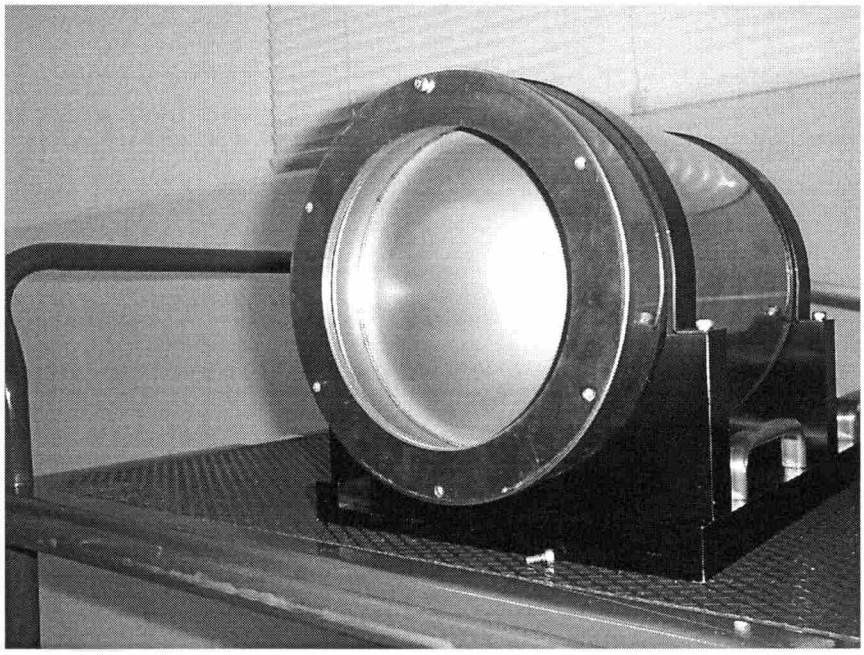

Figure 2.4. (a) Layout of time resolved x-ray diffraction experiments. (b) X-ray image intensifier.

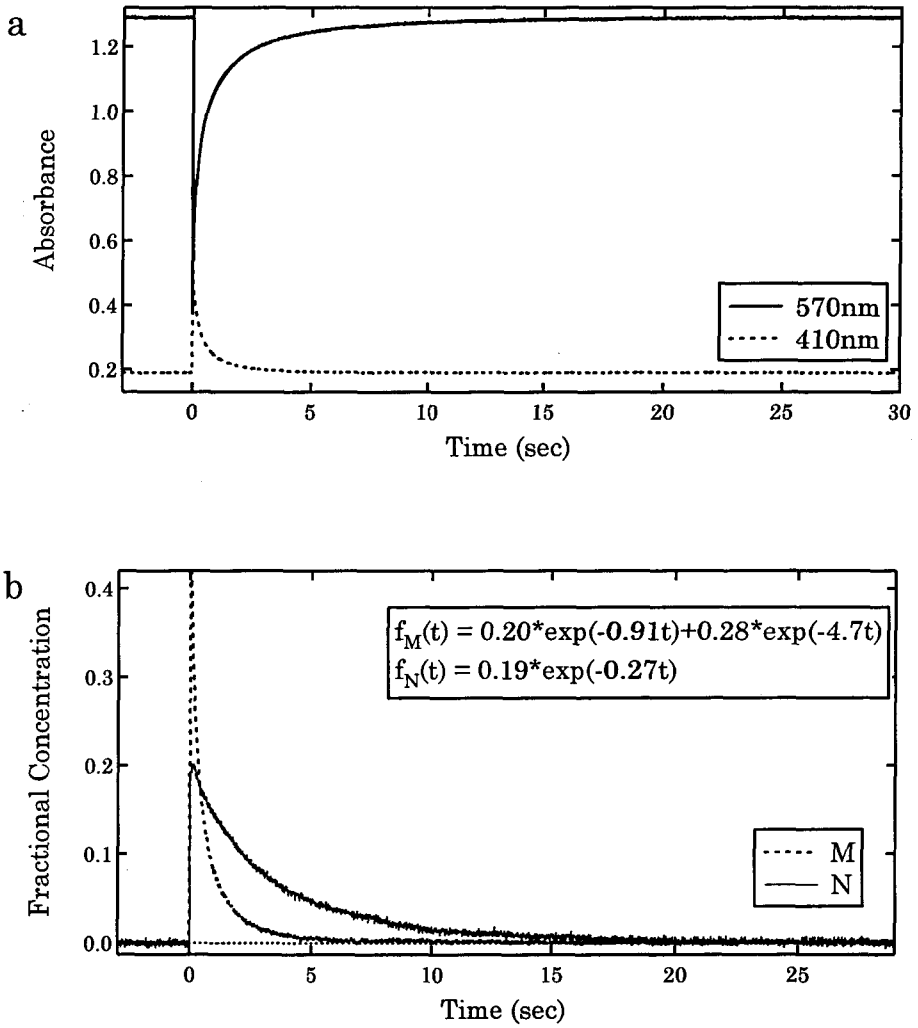

Figure 2.5. (a) Absorbance changes of wild-type BR (pH9,10°C) at 570 nm and 410 nm after a xenon flash lamp excitation. Time resolution is 10 msec. M and N intermediate are observed in this condition. Generation of M intermediate causes increase of absorbance at 410 nm and decrease at 570 nm, but generation of N causes decrease of absorbance at 570 nm and doesn't perturb absorbance at 410 nm. Then fractional concentrations of M and N intermediates are estimated from these absorbance changes. This figure shows that decays at 570 nm and 410 nm are different. this result indicates coexistence of M and N intermediate at this condition. (b) Estimated fractional concentrations of M and N intermediates from data shown in (a). M intermediate decays faster than N intermediate. Double exponential function was used to fit the fraction of M intermediate, and single one was used to N.

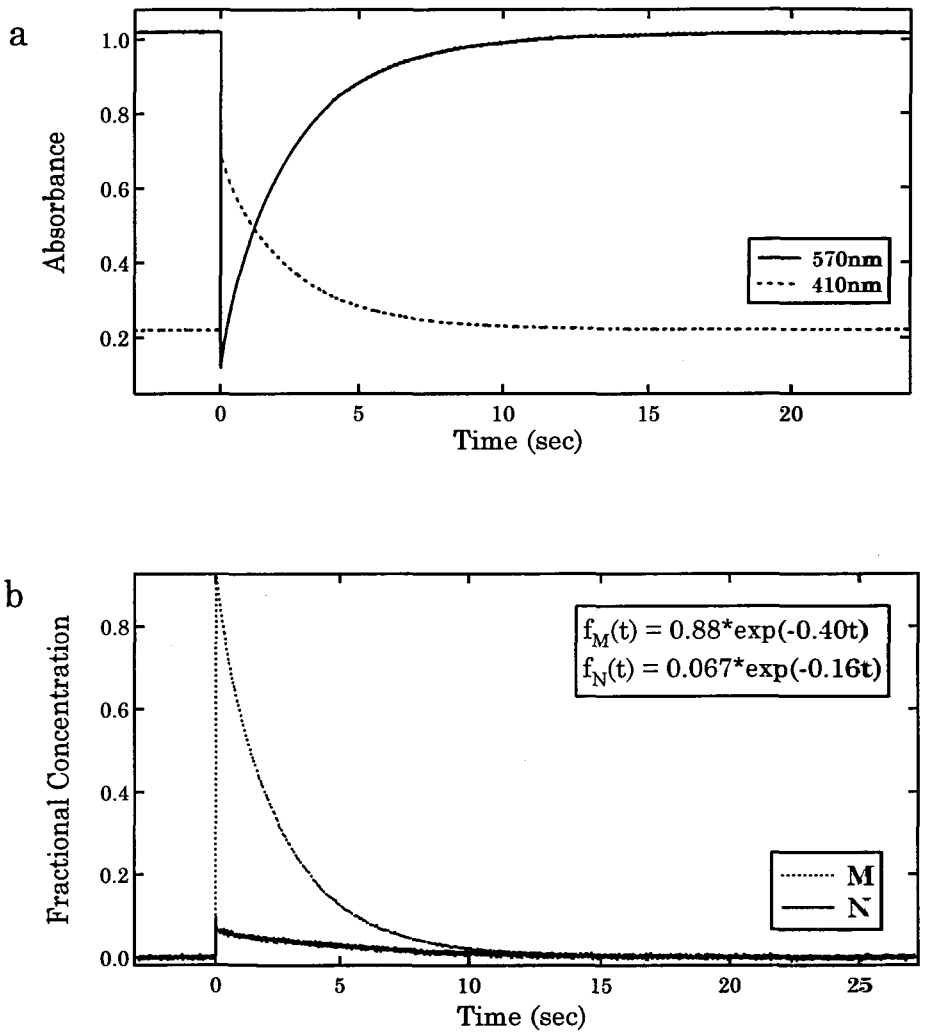

Figure 2.6. (a)Absorbance changes of D96N BR (PH7, 25°C) at 570 nm and 410 nm after an xenon flash lamp excitation. Decays of 570 nm and 410 nm are almost the same because M intermediate is major component in this condition. (b) Estimated fractional concentrations of M and N intermediates from data shown in (a).

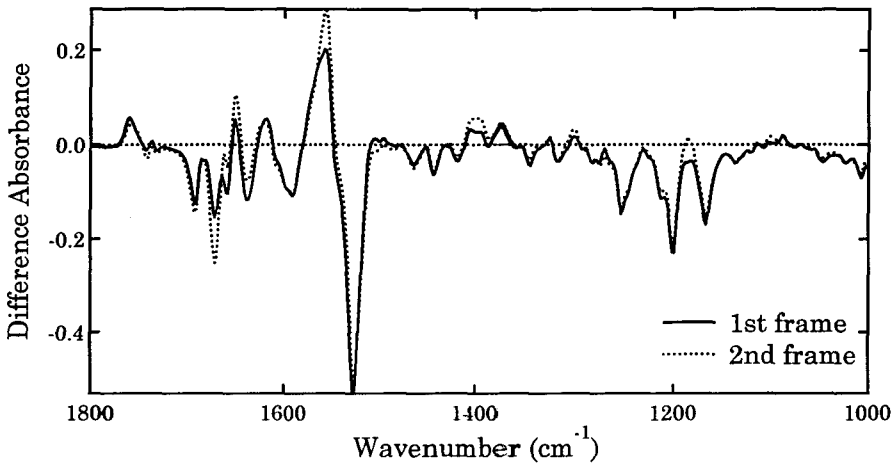

Figure 2.7. FTIR difference spectrum change of wild-type BR (pH9,10°C) after a flash excitation. Time resolution was 133 msec. This Figure shows first and second frames of FTIR spectra after a flash excitation.

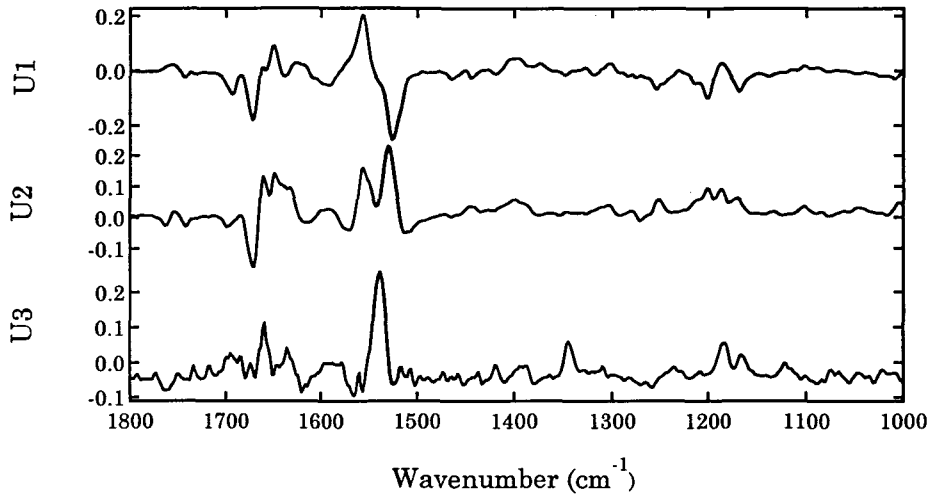

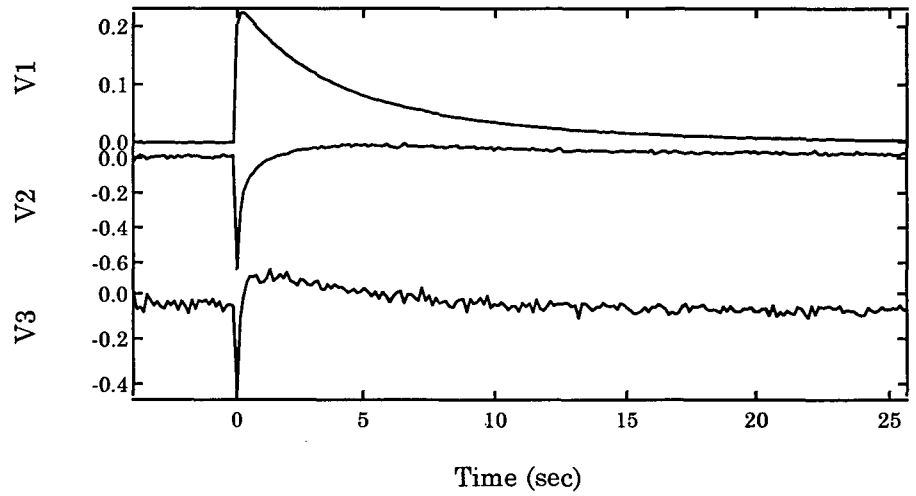

index	SingularValues
1	7.71197
2	1.2549
3	0.316301
4	0.174346
5	0.113136
6	0.108747
7	0.100389
8	0.087128
9	0.0818613
10	0.0791794

Figure 2.8. FTIR difference spectrum change of wild-type BR (pH9,10°C) was analyzed by SVD. Figure shows extracted 3 signal components of U and V spectra. Table shows singular values of 10 major components.

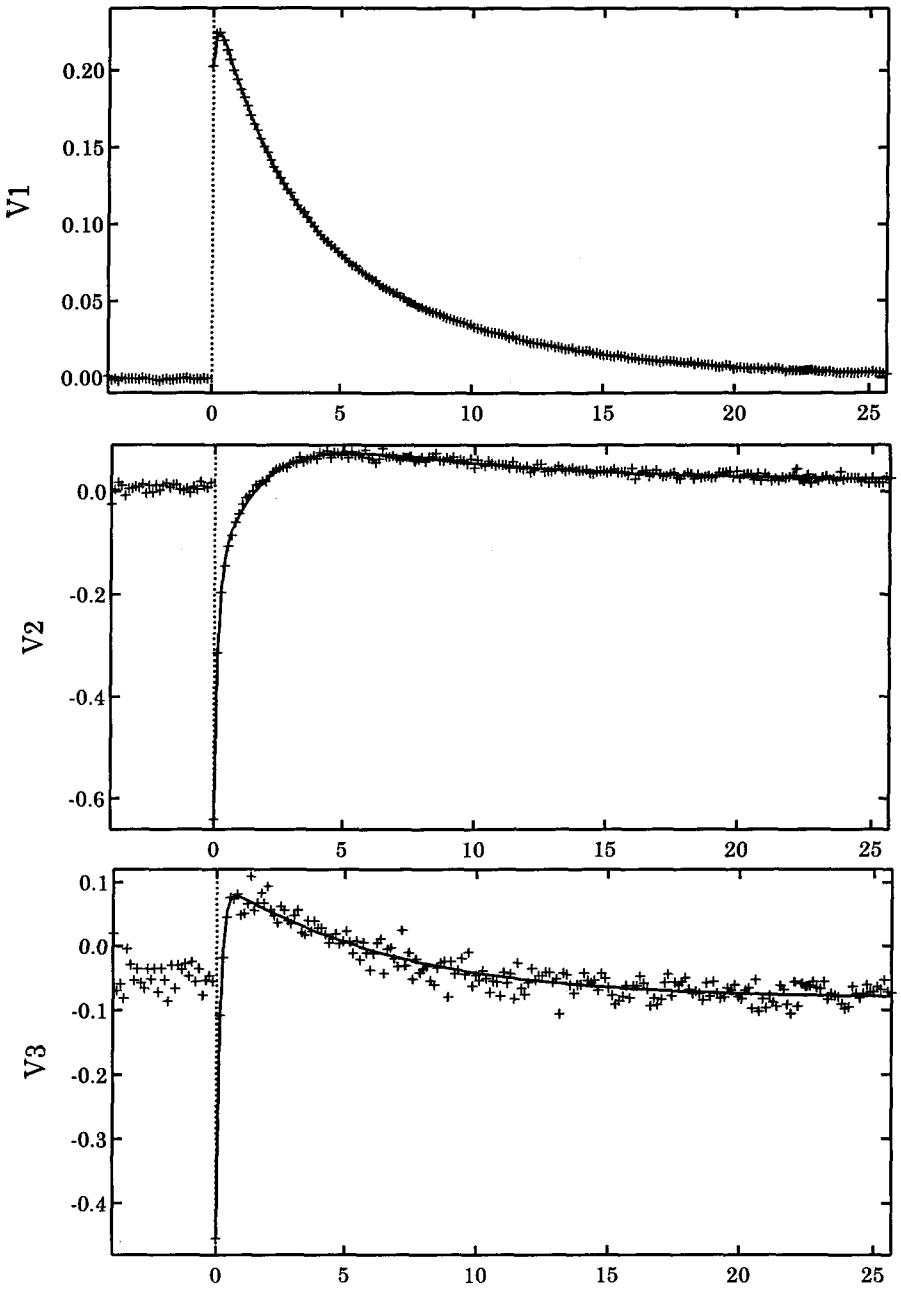

Figure 2.9. Since SVD analysis extracted 3 components from FTIR data, this reaction system were constituted from 3 changeable components and 1 original components. Then V spectra of FTIR data were fitted with triple exponential functions. Each parameter is descried in the main part.

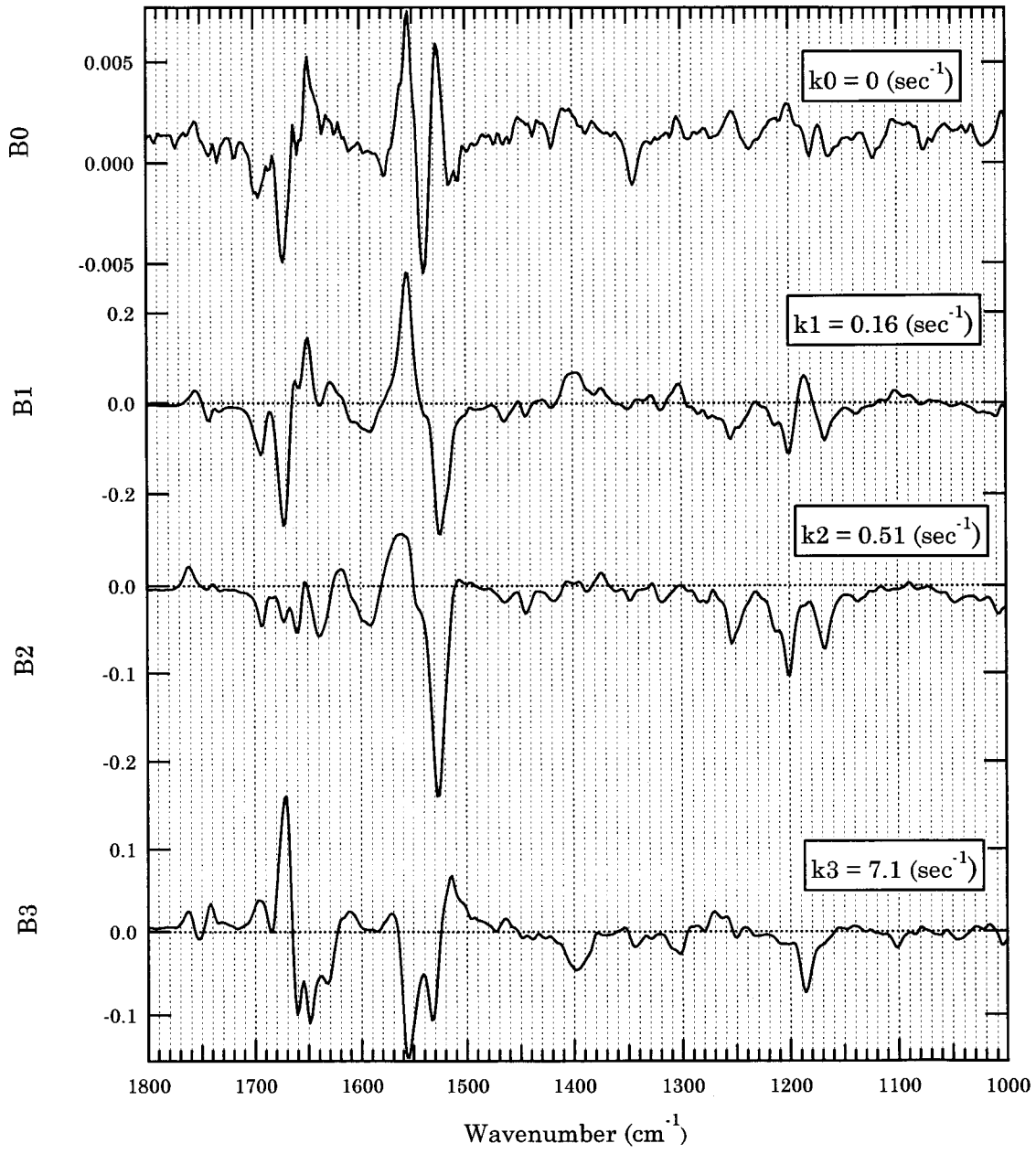

Figure 2.10. Reconstitute spectra from triple exponential function fit. Constant component might be a component, which cannot go back to original state in this time range or which is bleached BRs in alkaline photo-absorption. B1 spectrum (k1=0.16) is that of the N intermediate, and B2 spectrum (k2=0.51) is the M intermediate one (Sasaki et al., 1994). M and N intermediates are separated by exponential function fits. Then this reaction system is not simple one as described in 2.2.8. B3 is the spectrum of M minus N intermediate.

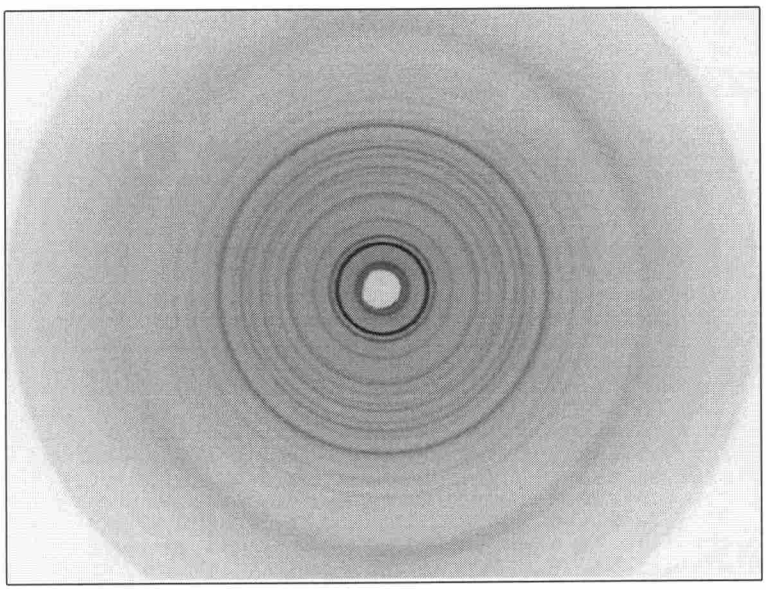

Figure 2.11. This Figure shows that an x-ray diffraction pattern of purple membranes recorded by the CCD camera with the x-ray image intensifier. Exposure time was 1 sec. Purple membranes were oriented on a piece of mylar sheets (polymer film). Since x-ray is incident to this film vertically, c axis of BR two dimensional crystals (purple membranes) are parallel to x-ray. But there are many crystals on a piece of mylar sheet and a ,b axis of crystals are not oriented. Then x-ray diffraction pattern from this sample become like a powder diffraction pattern. This image was averaged circularly to proceed data analyses.

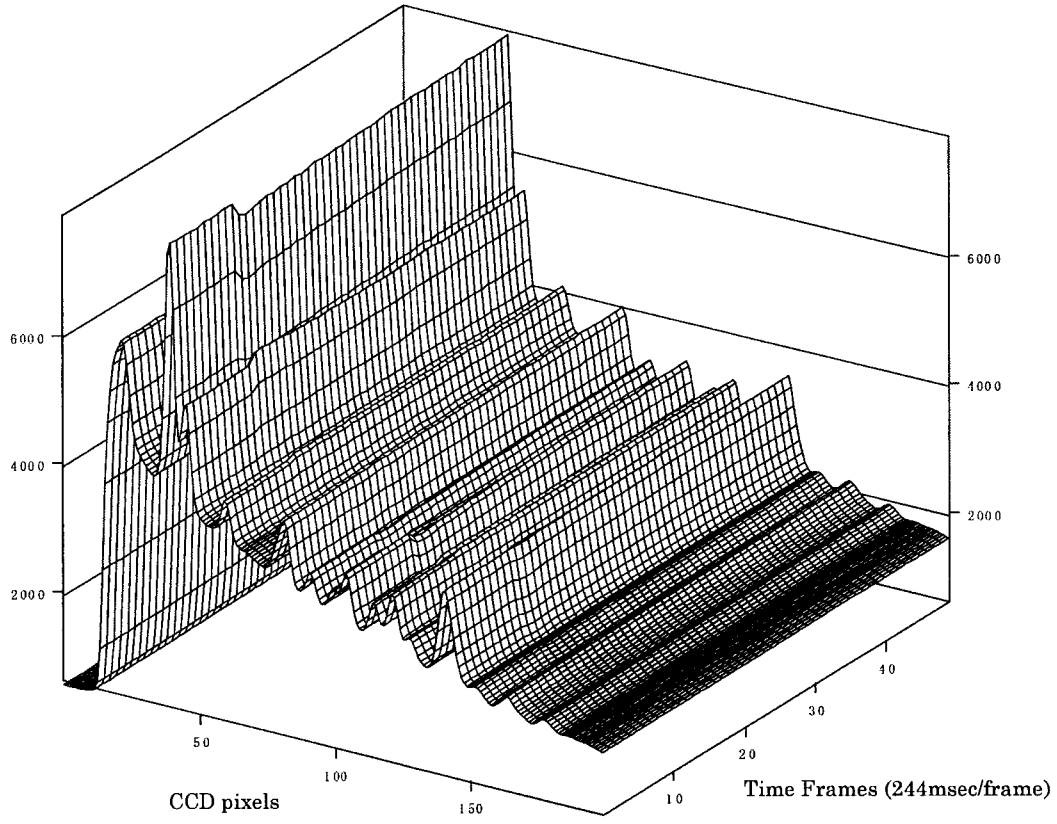

Figure 2.12. Time-resolved x-ray diffraction pattern of wild-type BR (pH9, 10° C) before and after a xenon flash lamp excitation. Bragg peaks up to 7 A are observed. Time resolution of this experiment is 244 ms. Time frames are only shown up to 50th frame, but diffraction patterns are recorded up to 200th frame. BR was illuminated at 11th frame. Excitation causes the changes of diffraction pattern These changes comes from structural changes of BR in its photocycle.

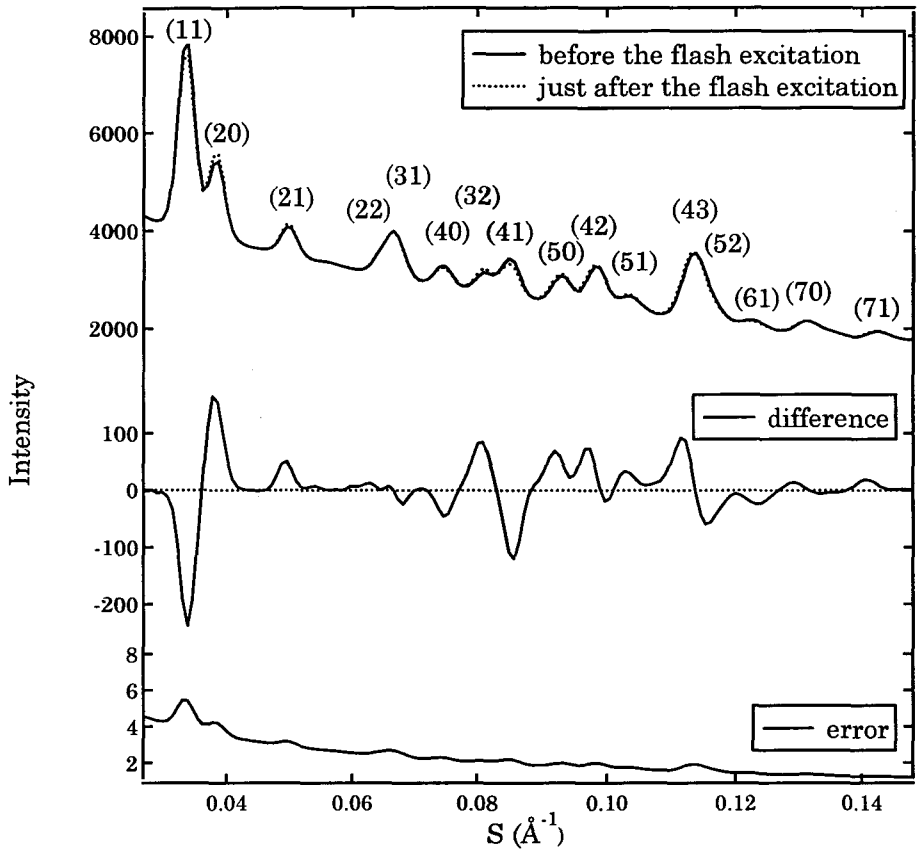

Figure 2.13. X-ray diffraction profiles of wild-type BR (pH9, 10°C) before and just after flash excitation and difference. Estimated error of each frames is also shown. Intensity change by flash excitation is small, but this change is much larger than noise level.

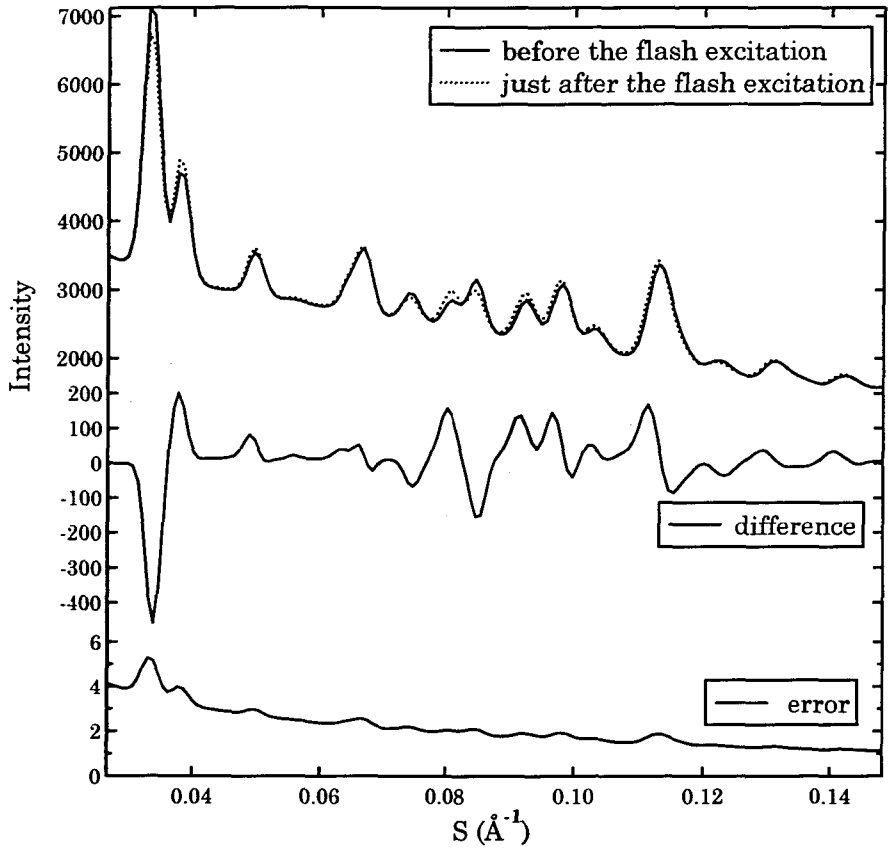

Figure 2.14. X-ray diffraction profiles of D96N BR(pH7, 25°C) before and just after flash excitation and difference. Estimated error of each frames is also shown.

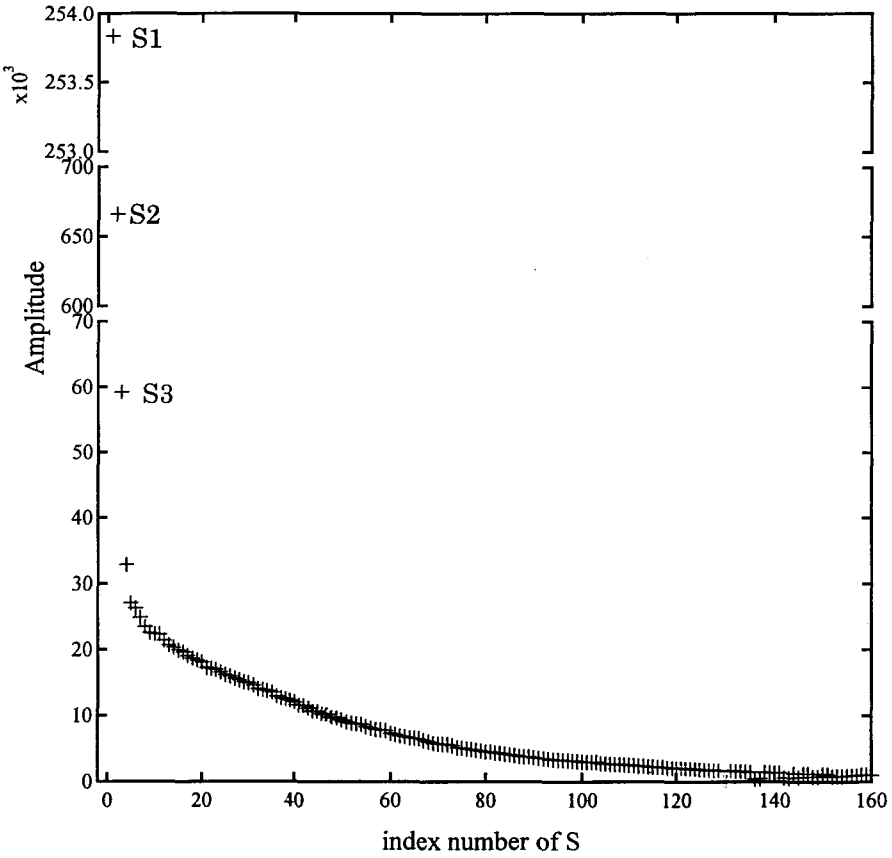

Figure 2.15. Singular values of the SVD analysis result for weighted diffraction data of wild-type BR (pH9, 10°C). Singular values of noise components decrease gradually. Fourth singular value is apart from sequential singular values of noises. But 4th one does not separate clearly. Then it is taken as a noise.

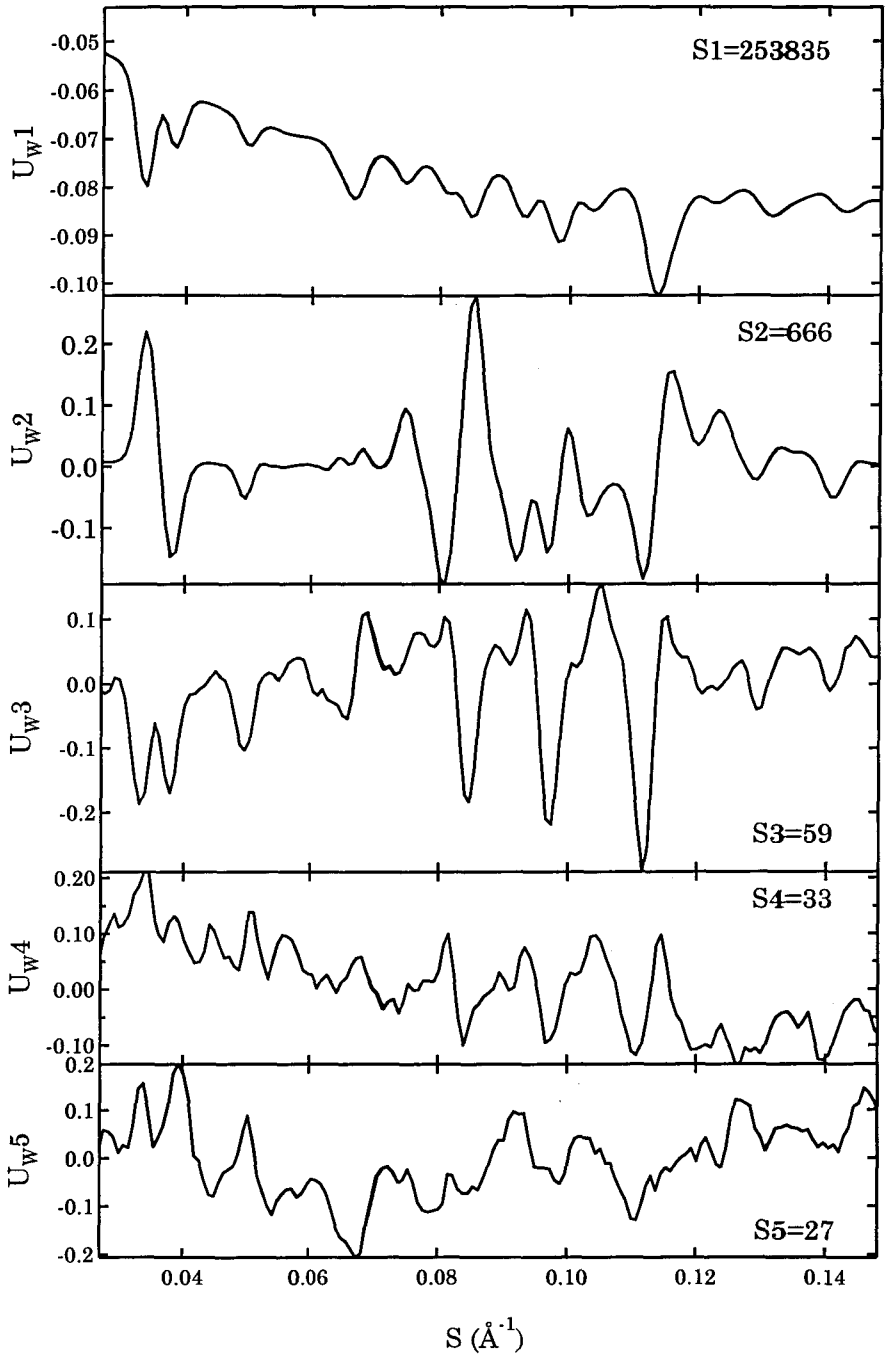

Figure 2.16. Uw spectra of the SVD analysis result for weighted diffraction data of wild-type BR (pH9, 10°C). 5 major components are shown.

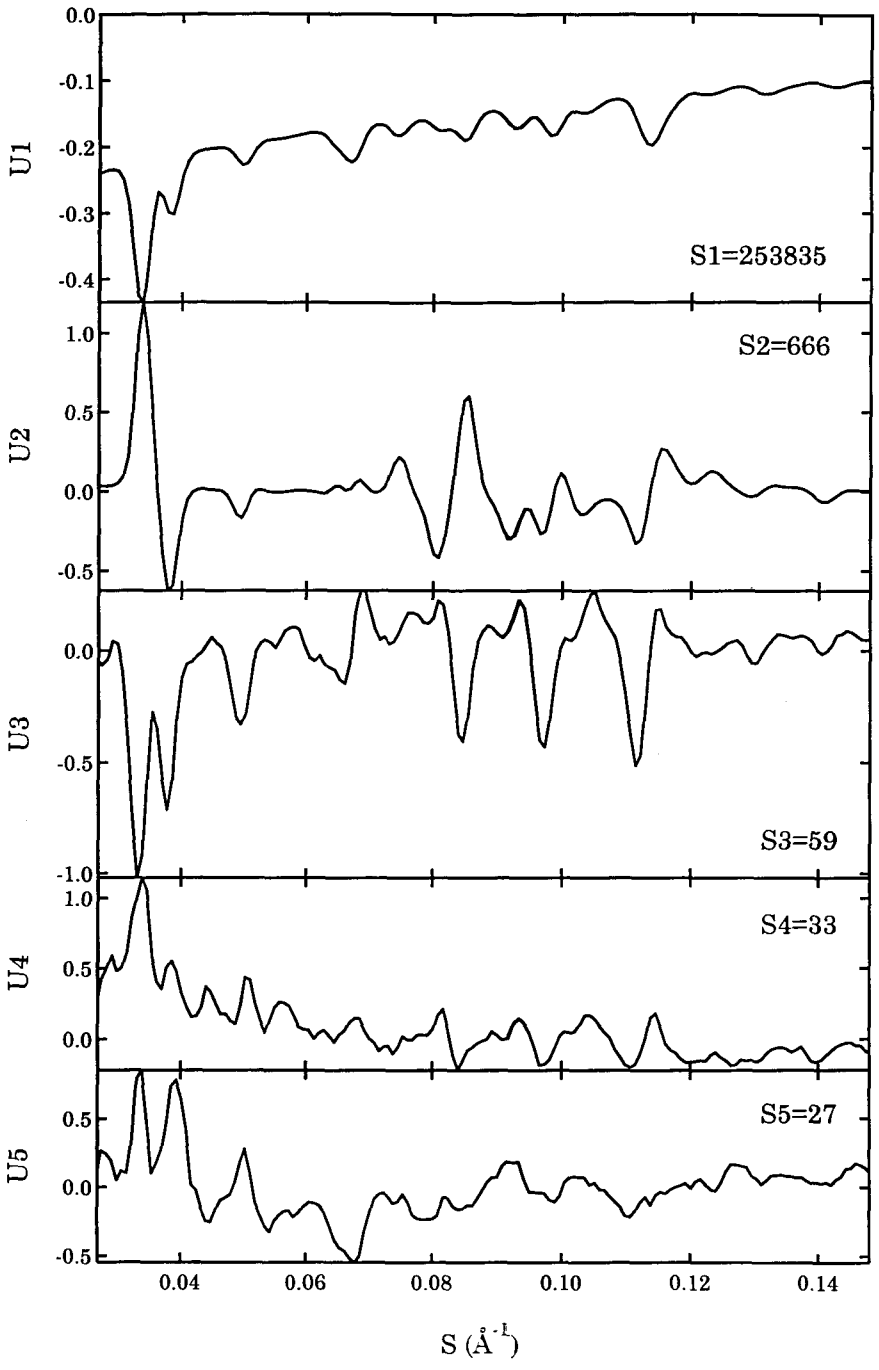

Figure 2.17. U spectra of SVD analysis for weighted diffraction data of wild-type BR (pH9,10°C) (see 2.2.7.2). This Figure shows 5 major components. U1 has a negative sign but it is almost same as diffraction profile shown in Fig. 2.13. U2 is almost same as difference diffraction profile shown in Fig. 2.13. But difference of (11) and (20) peaks are different clearly. U3 have clear profile. Third singular value also indicates that this component is distinguishable from noise.

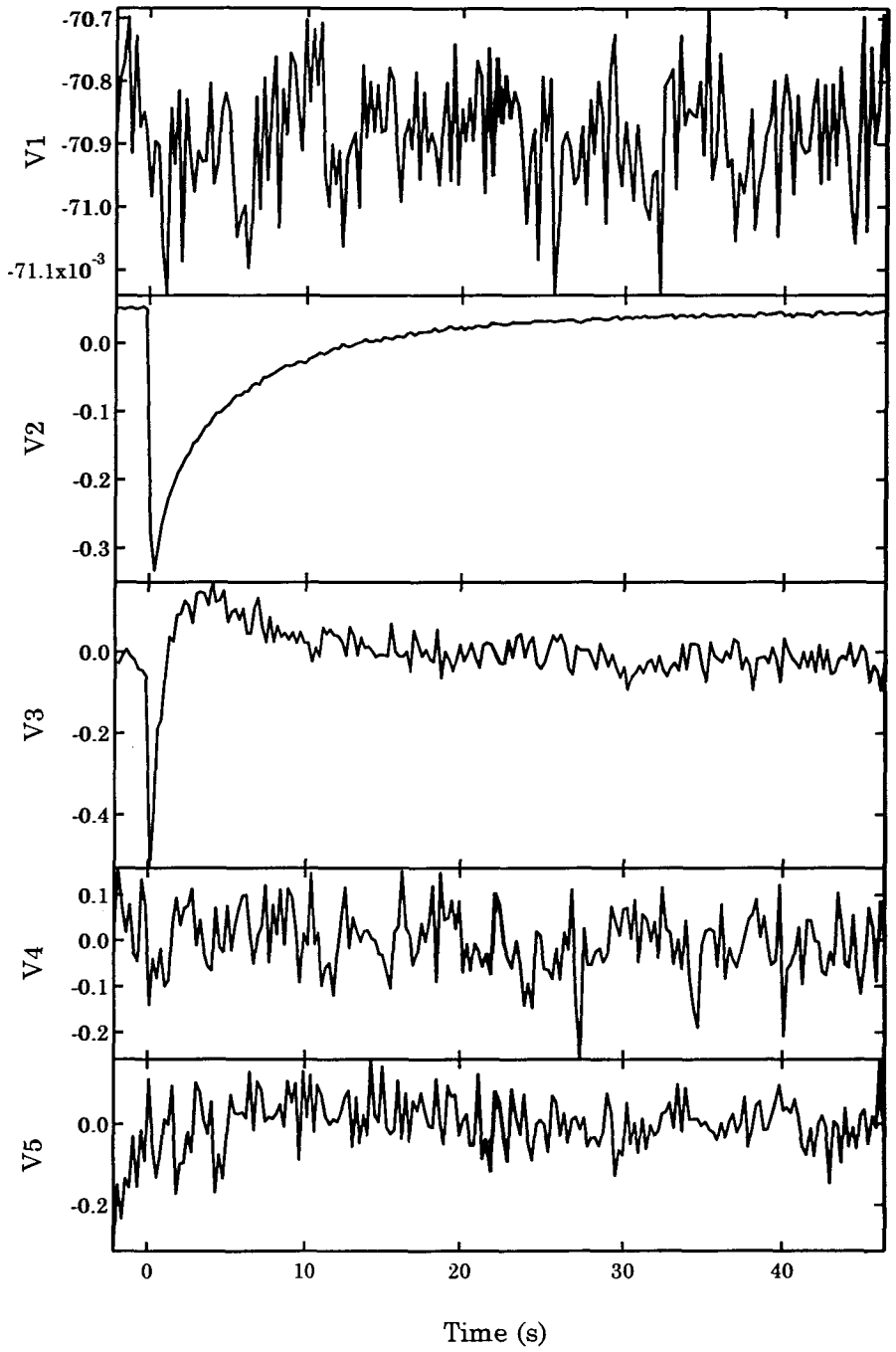

Figure 2.18. V spectra of the SVD analysis result for weighted diffraction data of wild-type BR (pH9, 10°C). This spectra indicate time course of corresponding U and Uw spectra. V1 has no time dependency. it has almost constant at 0.0709. U1 is time constant component. V2 and V3 changes largely by flash excitation at time 0. Then U2 and U3 are time dependent components. V4 and V5 has no time dependency. Shortly according to this result, one time independent component and two time dependent components were observed in decay process of wild-type BR (pH9, 10°C).

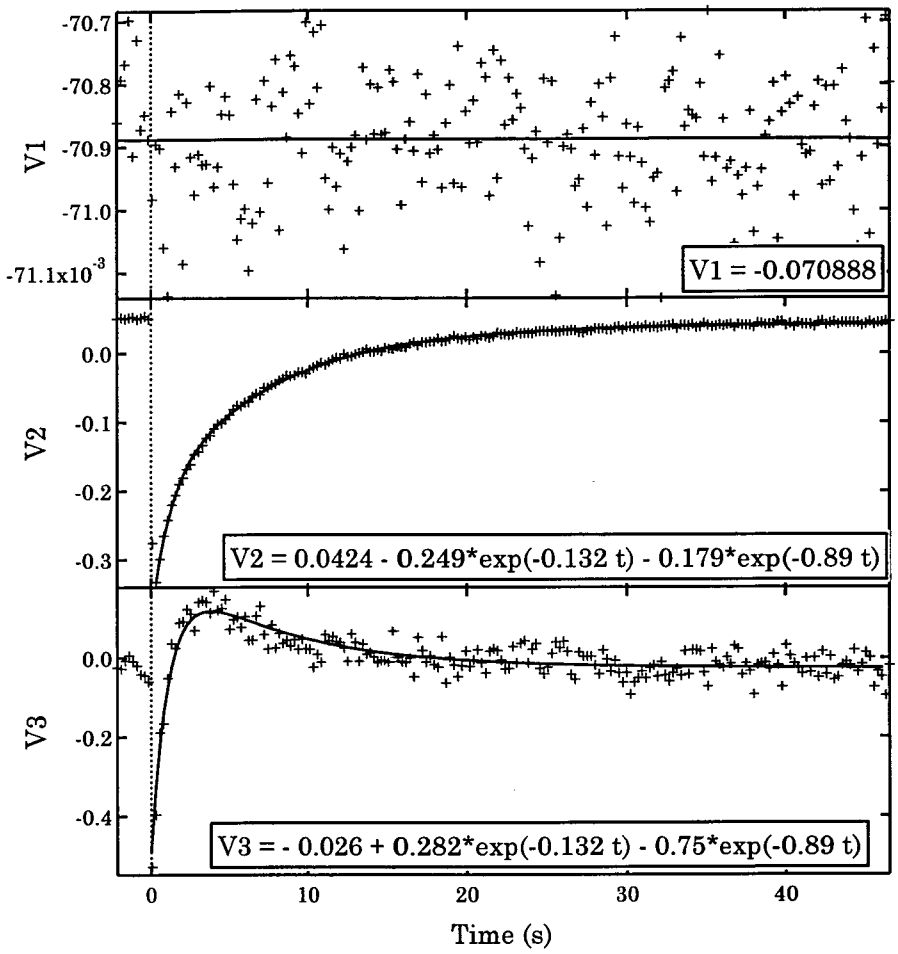

Figure 2.19. The result of fits to 3 major V spectra of weighted diffraction data (wild-type BR, pH9, 10°C) (see 2.2.8. and 2.3.4). Three components were separated; time independent component (k=0), slow one (k=0.132), and fast one (k=0.89).

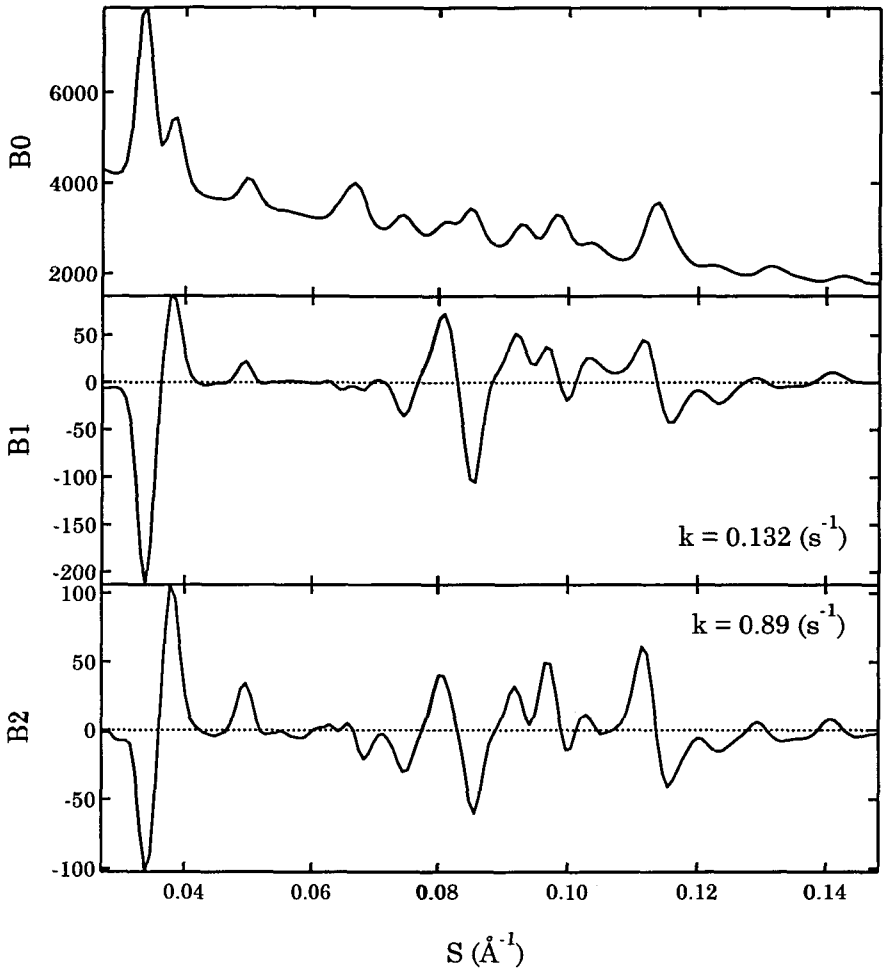

Figure 2.20. Reconstituted B spectra of weighted diffraction data (wild-type BR, pH9, 10°C) (see 2.2.8). B0 is ordinary diffraction profile of purple membrane under dark condition. B1 and B2 are correspond to N and M intermediate (see 2.3.1 and 2.3.2). Difference between B1 and B2 is not large. But some difference is seen. Especially, ratios of (11) and (20) peaks are clearly different. The peak height of (11) negative peak (S~0.030) is about 3 times larger than that of (20) positive peak (S~0.035) in N intermediate (B1). But its ratio is almost 1 in M intermediate (B2). These characters are same as that of alkaline D96N under photosteady condition (Kamikubo et al., 1997).

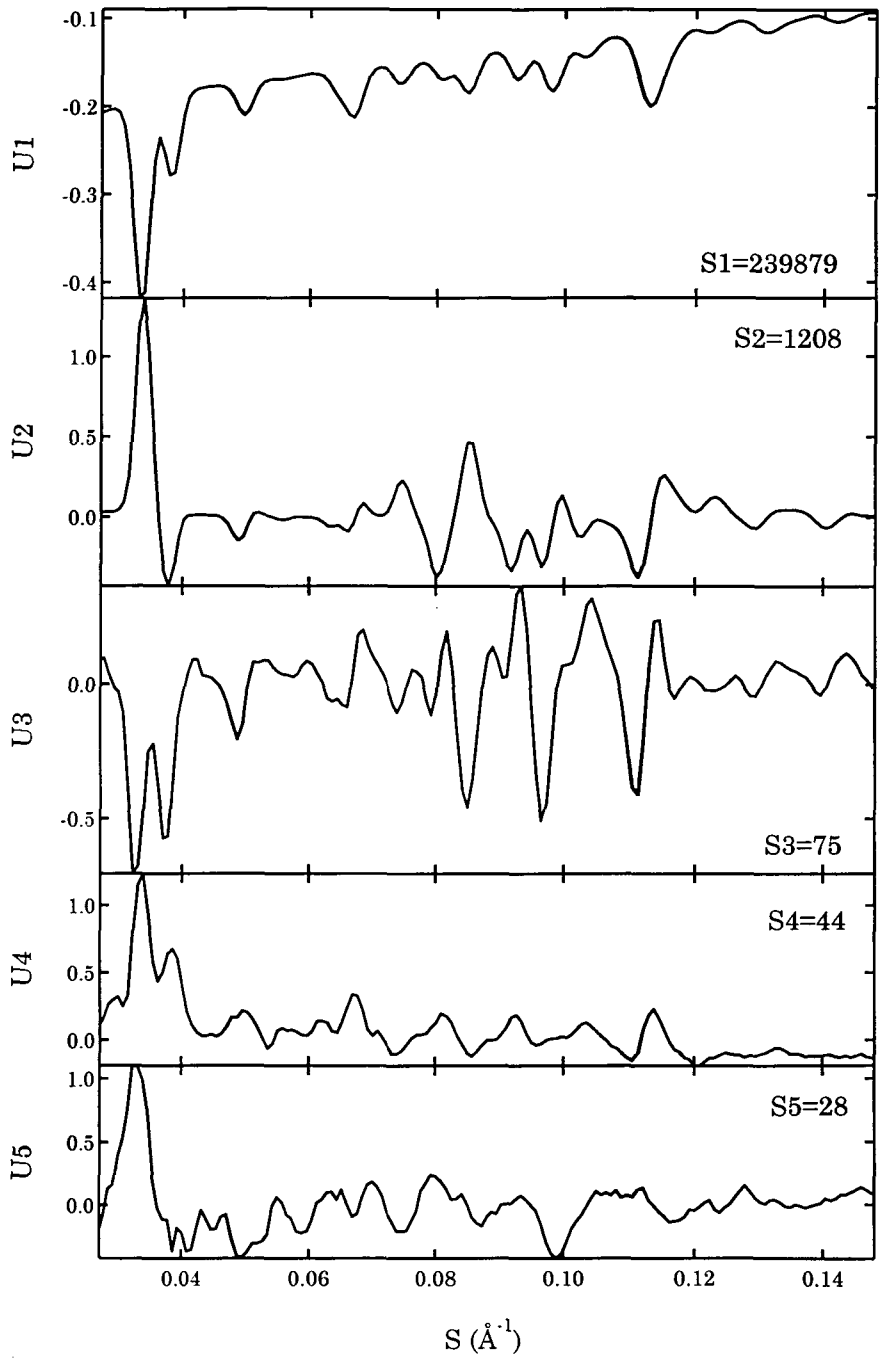

Figure 2.21. Time-resolved x-ray diffraction data of D96N (pH7, 25°C) was also analyzed by SVD. This Figure shows 5 major U spectra of D96N (pH7, 25°C). Singular values of latter components are 25, 24, 24, 23, 23, 22, and so on. Then U1, U2, U3 are separated from noise. Because U1, U2, U3 of D96N are almost same as those of wild-type, structural changes of D96N and wild-type are considered as identical.

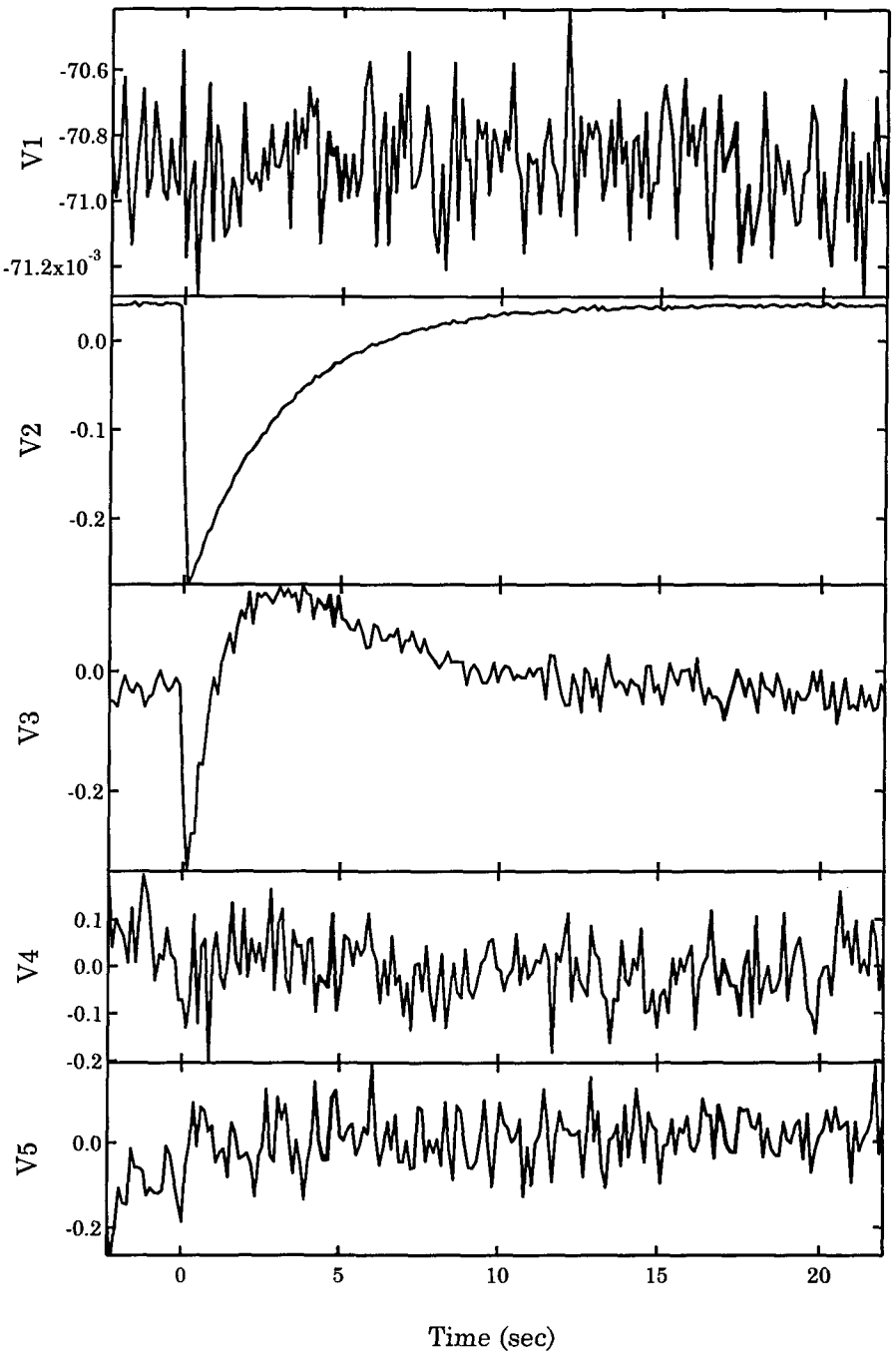

Figure 2.22. V spectra of the SVD analysis result for weighted diffraction data of D96N (pH7, 25°C). Since V4 and V5 don't have clear time dependency, they are not distinguishable from noise. On the contrary to these, V1, V2 and V3 has clear time dependence

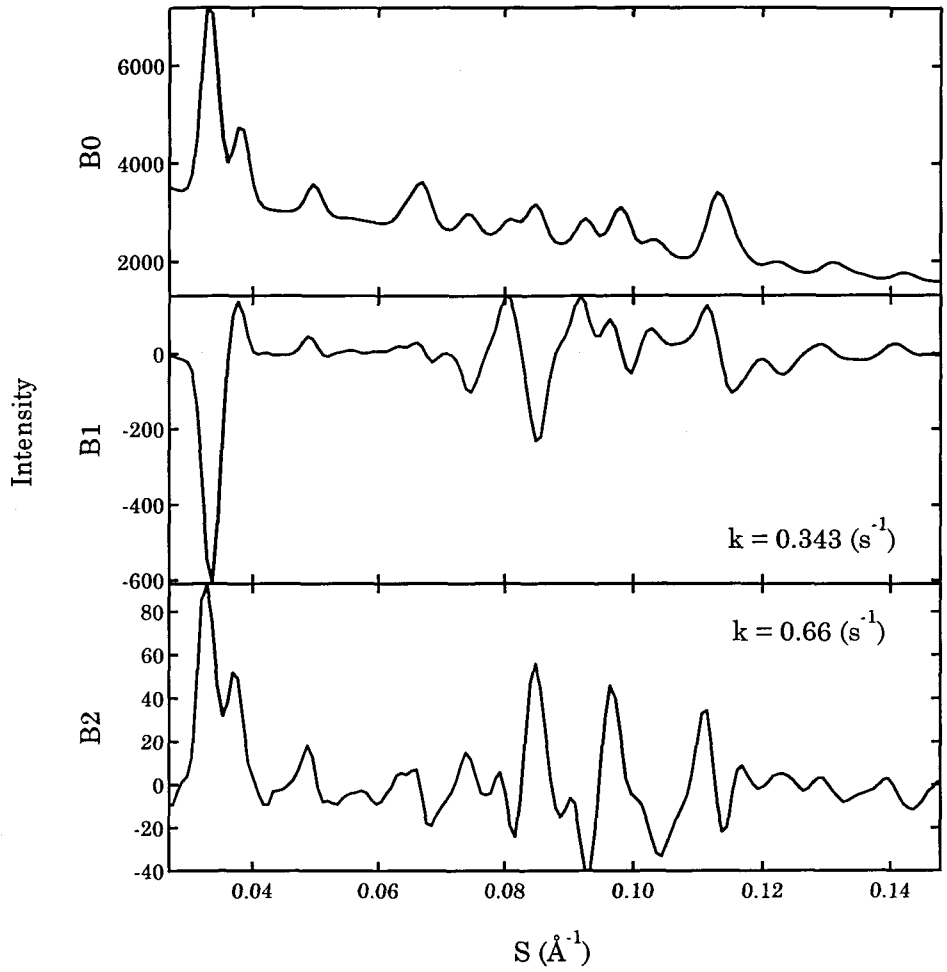

Figure 2.23. Reconstituted B spectra of weighted diffraction data (D96N, pH7, 25°C) (see 2.2.8). B0 is diffraction profile of purple membrane under dark. B1 is a slow decay component, and B1 is a fast one. D96N accumulates almost M intermediate at this condition (Fig. 2.6). Then observed two intermediates might be M and MN intermediate (Sasaki et al., 1992; Kamikubo et al., 1997).

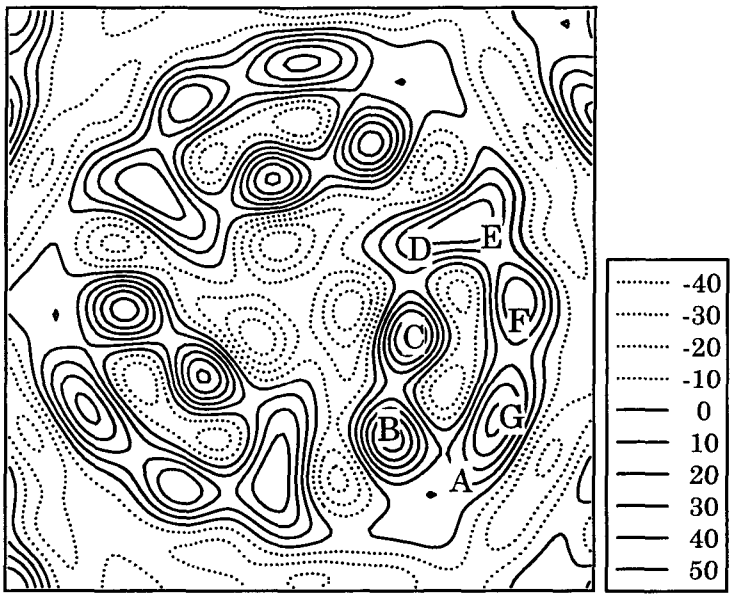

Figure 2.24. Electron density map of wild-type BR (pH9, 10°C) before a flash excitation.

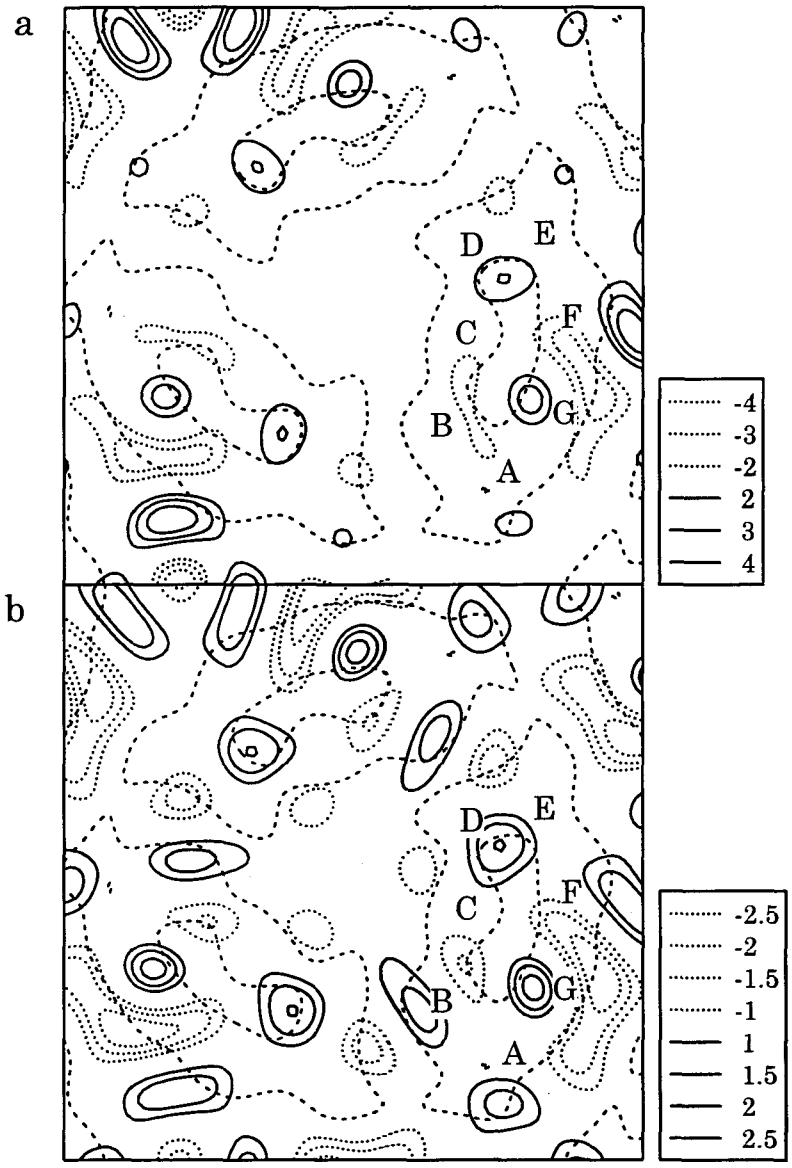

Figure 2.25. Difference Fourier maps of the slow and the fast component of wild-type BR (pH9, 10°C) in Fig 2.20. (a) Map of the slow component. (b) Map of the fast component. Structural changes occur near F and G helix in both maps. But peak of F helix is higher than that of G in (a). On the contrary that of G helix is higher than that of F helix in (b). Since the fast and the slow components correspond to M and N intermediates, the positive peak of F helix increase in M-N transition. This change corresponds to movement of F helix terminals. The peak heights of F and G helix are 5.0 and 3.6 in (a), 1.9 and 2.3 in (b). Estimated errors of this maps are 0.75 and 0.47.

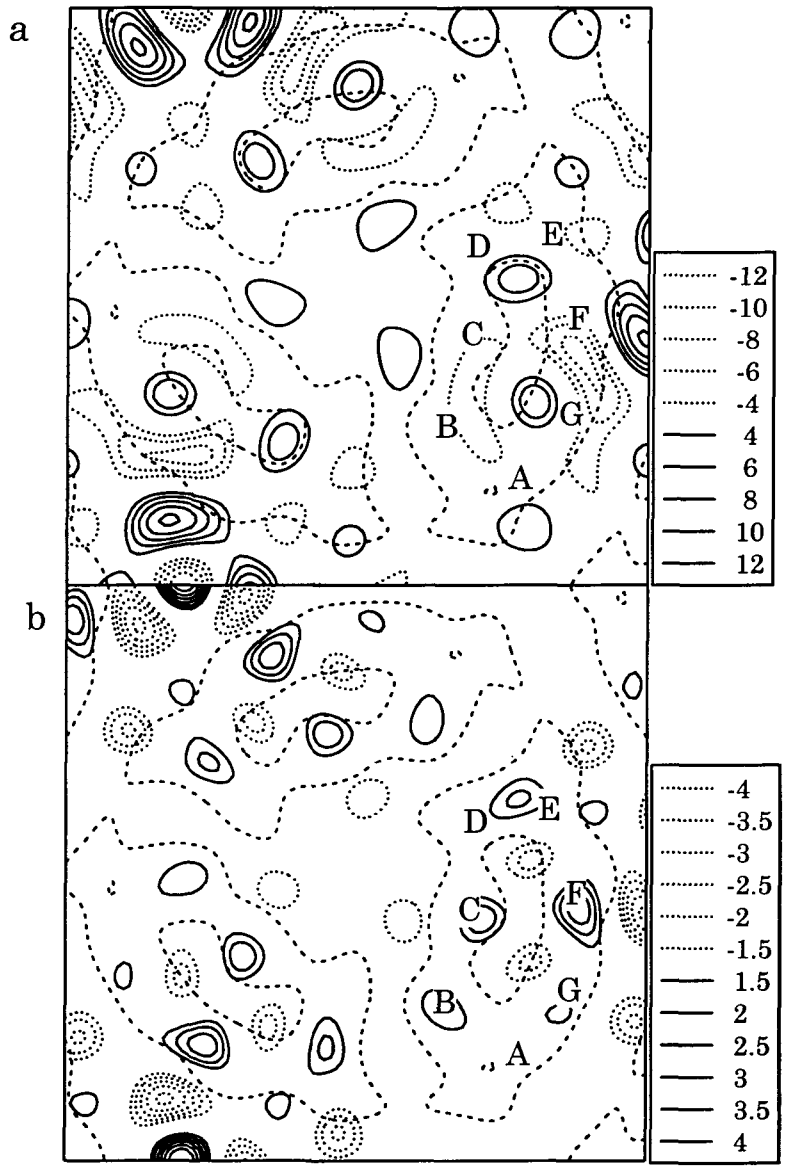

Figure 2.26. Difference Fourier maps of the slow and the fast decay components of D96N (pH7, 25°C) B spectra in Fig. 2.23. (a) Map of the slow component. BR structure near F and G helices changes clearly. This difference map is almost same as that of N intermediate of wild-type. (b) Map of the fast component. A negative peak is seen at outside of F helix. This position is same as the positive peak of F helix in (a). Consequently F helix is low just after a flash excitation (summation map of slow and fast components), then it increase as the fast component decay (map of slow component). The positive peak heights of F and G helix in (a) are 12. 5 and 7.6. The negative peak heights of F helix in (b) is –3.7. Estimated errors of this maps are 1.8 and 0.54.

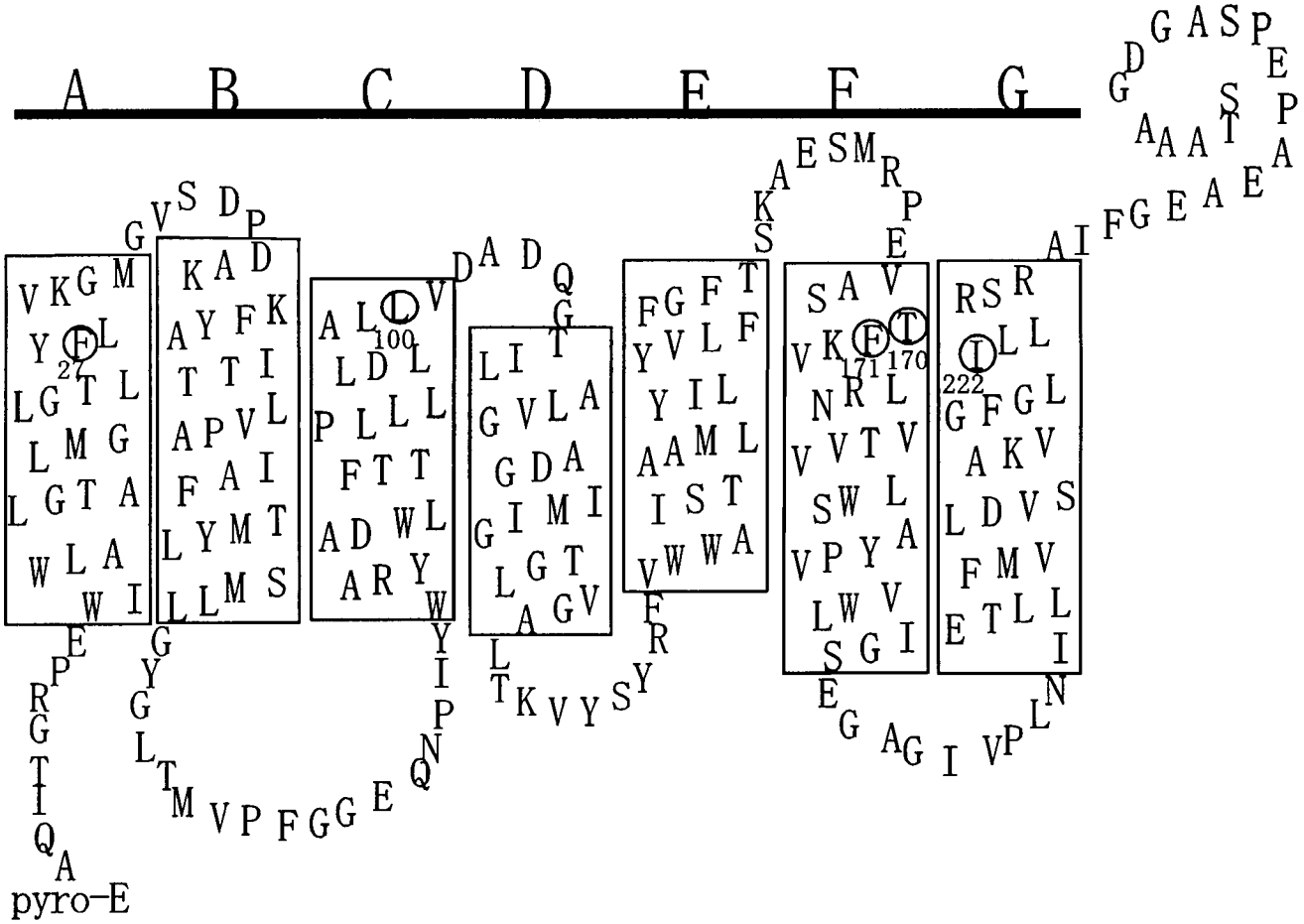

Figure 3.1. Secondary structure of bacteriorhodopsin from Grigorieff et al. (1996). The each circled residue was substituted with cysteine in F27C, L100C, T170C, F171C, I222C.

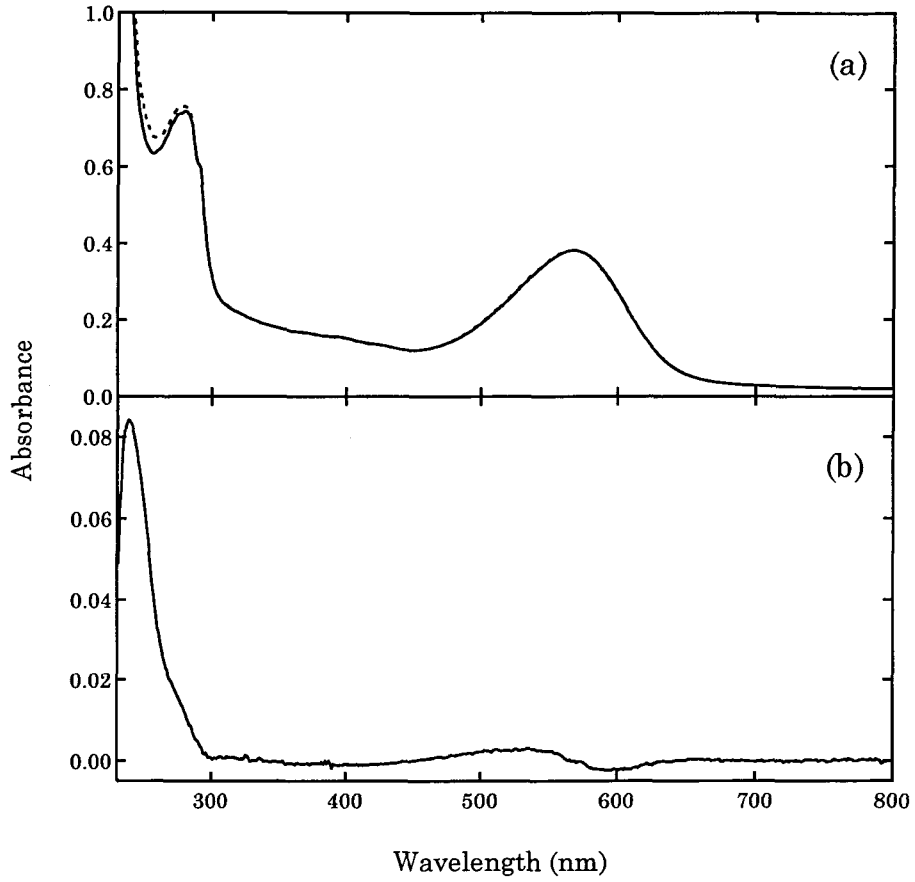

Figure 3.2. (a) Light-adapted spectra of 222C (solid line) and 222CMB (dashed line), in 50mM sodium phosphate, pH 7.0, 20 °C. Data are Normalized at 568 nm. (b) Difference spectrum between 222CMB and 222C.

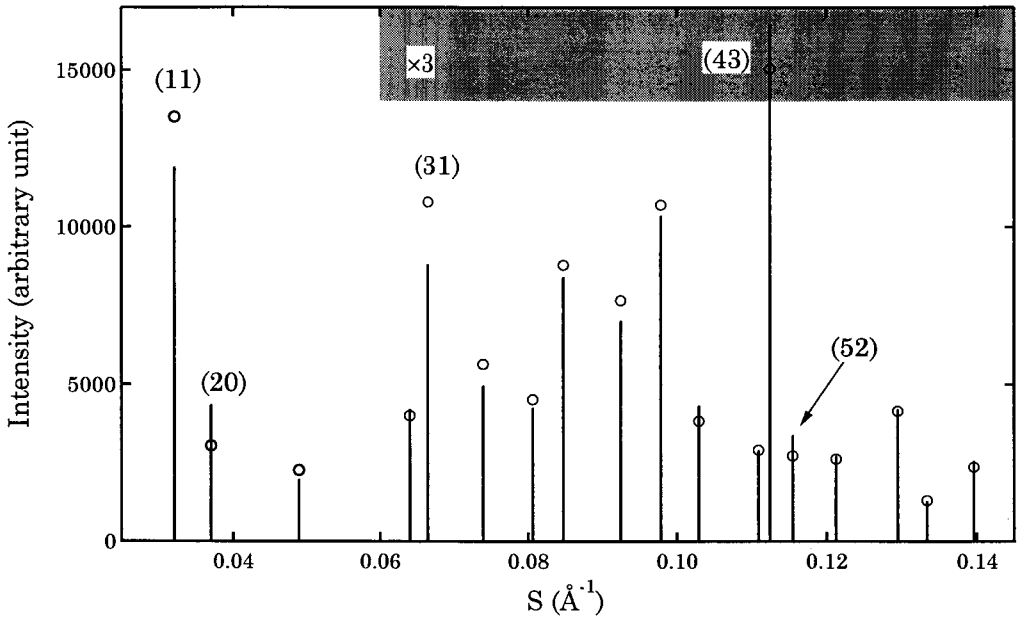

Figure 3.3. X-ray diffraction intensities of labeled and non-labeled I222C bacteriorhodopsin. S > 0.06 region are expanded by a factor of 3. Almost all errors are smaller than the radius of circle , so error bar were not shown.

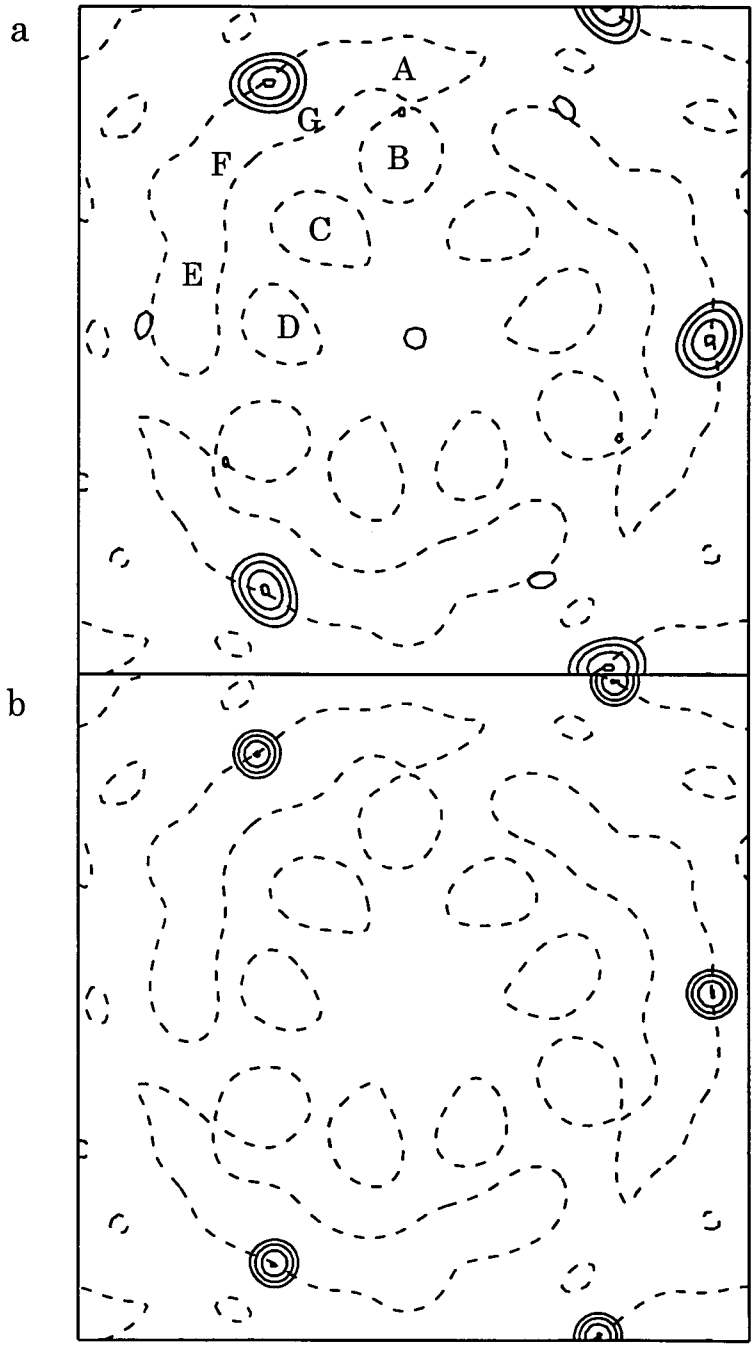

Figure 3.4. Two-dimensional difference electron density maps between heavy atom labeled and non-labeled I222C bacteriorhodopsin. Dashed contour line is an outline of bacteriorhodopsin. Four solid contour lines indicate 70, 80, 90, 99 % when the difference the maximum and minimum density set as 100 % and 0 %. The characters on the map indicates each helix location. The sides of squares are 62.45 Å. (a)Before data refinement in Materrial and Method. (b)After data refinement.

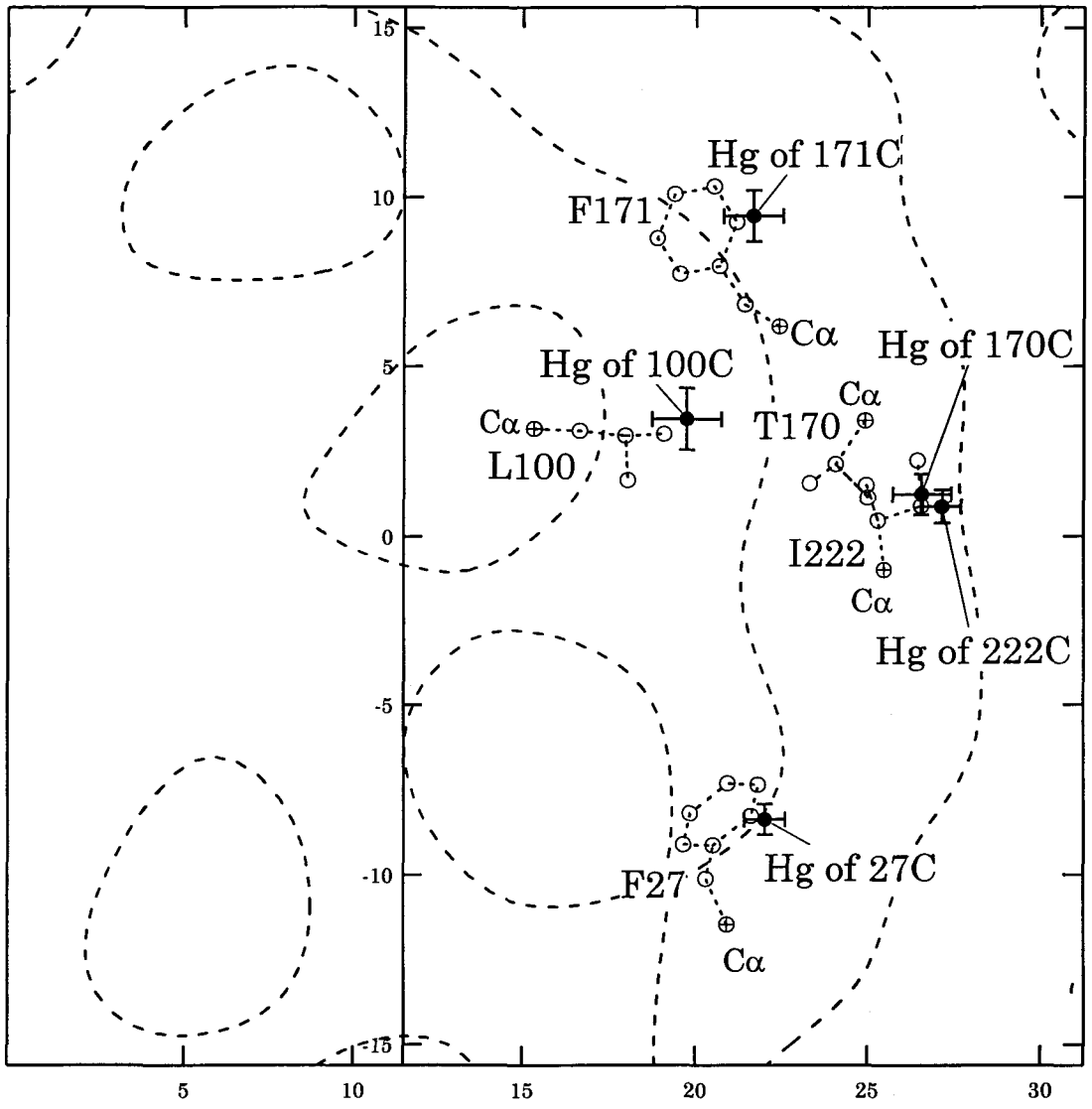

Figure 3.5. Location map of labeled mercury from my data and residues (2) which substituted in my experiment. Filled circle shows mercury position observed form this experiments. Empty circle Cα atom position from Grigorieff et al. (1996). Dashed contour line is an outline of bacteriorhodopsin. The each distance between mercury and Cα atom is shorter than 4.5 Å.

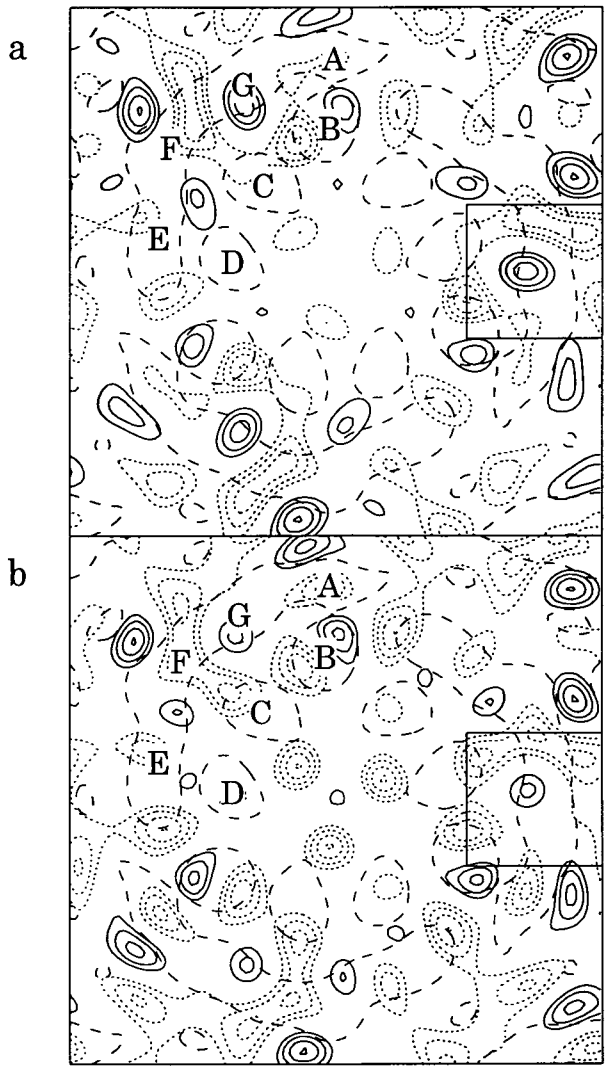

Figure 4.1. Difference density map between the M_N intermediate and the BR state: (a) non-labeled I222C BR, (b) PCMB labeled I222C BR. The four solid contour lines indicate 70, 80, 90, 99% density change and the four dashed lines 1, 10, 20, 30%, where maximum and minimum of the difference density set as 100% and 0%. The outlines of the helices of BR and the trimer are also shown. Boxed region indicates the region enlarged in Fig. 4.4.

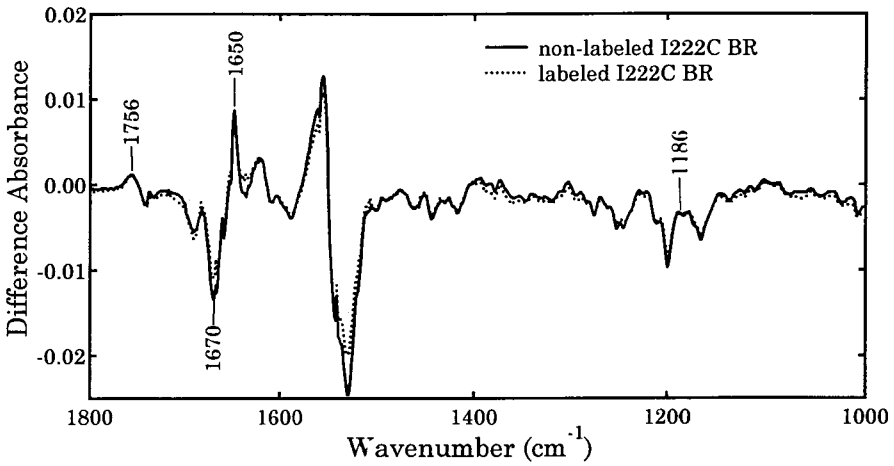

Figure 4.2. FTIR difference spectra between M_N intermediate state and BR state. The solid line indicates non-labeled I222C BR and the dashed line labeled I222C.

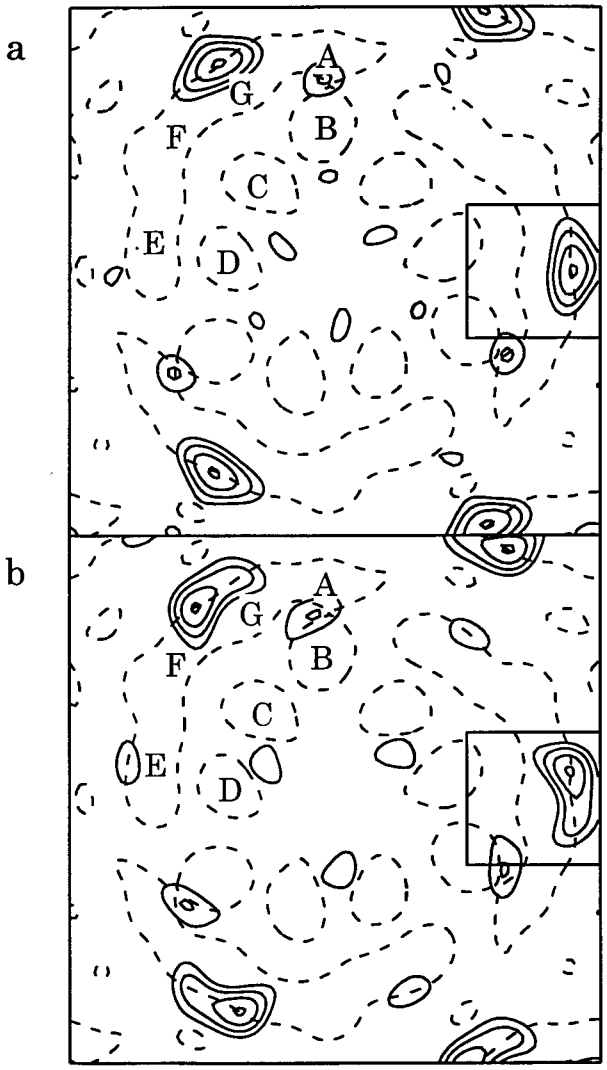

Figure 4.3. Difference density map between labeled and non-labeled I222C BR. (a) BR state. (b) M_N state. The four solid contour lines indicate 70, 80, 90, 99% density change. where the maximum and minimum of the difference density are set to 100% and 0%. All noise peaks observed are shown in this Figure. Boxed region indicates the region enlarged in Fig. 4.4.

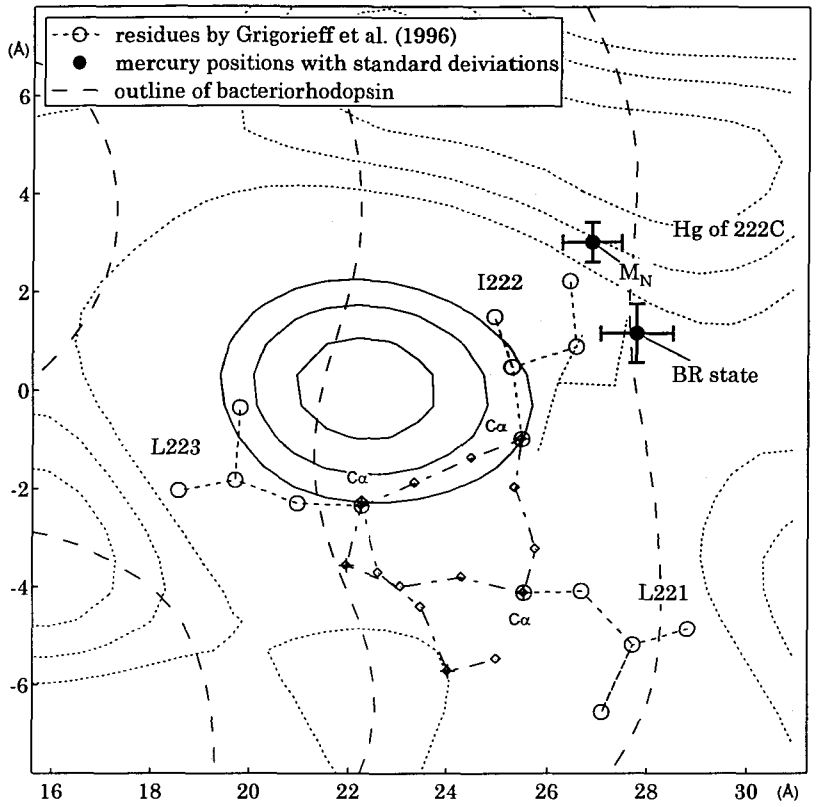

Figure 4.4. Mercury atom positions are shown in the M_N intermediate and the BR state. Error bars of position are also indicated. Wild-type BR residues (Grigorieff et al., 1996) from the 221st to the 223rd are shown. The non-labeled I222C density change map (Fig.4.1a) is superimposed.